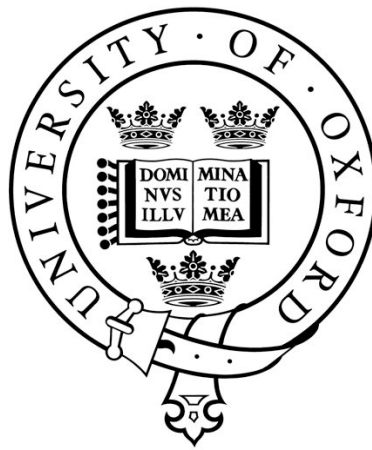


Trapping of Rubidium Atoms using Optical Tweezers

Lukas Brandt
Merton College, Oxford



Submitted for the degree of Doctor of Philosophy
Trinity Term 2011

Supervised by
Dr. Axel Kuhn

Clarendon Laboratory
University of Oxford
United Kingdom

Abstract

Trapping of Rubidium Atoms using Optical Tweezers

Lukas Brandt, Merton College, Oxford

Submitted for the degree of Doctor of Philosophy Trinity Term 2011

Supervised by Dr. Axel Kuhn

This thesis describes the realisation of a novel dipole force trapping method for cold neutral atoms, the optical tweezers. They are formed by imaging a spatial light modulator onto a mirror surface, by an aspherical lens. The spatial light modulator, a digital mirror device, consist of an array 1024 by 768 of micro-mirrors, which can individually be switched between the on and off position with a full frame refresh rate of 4 kHz and hence can create arbitrary light patterns in real time. Atoms are trapped through the dipole force in them. The optical tweezers have a potential depth on the order of 1 mK.

A magneto-optical surface-trap cools and traps Rubidium atoms close to the mirror surface. Unlike a normal magneto-optical trap, which traps atoms in free space, this trap incorporates a mirror, above which the atoms are trapped and then loaded into the optical tweezers.

I will show that we managed to load atoms into the dipole traps with a variety of different potential landscapes and observe them with a highly sensitive CCD-camera through fluorescence imaging.

Furthermore I study a scheme to use a high powered, but spatial multimode diode laser for atom trapping. An optical diffuser smoothes out the otherwise poor quality profile, to make the high power diode laser applicable for optical tweezers.

Contents

1	Introduction	1
2	Theory	5
2.1	The Interaction of Light with a Single Atom	6
2.1.1	Theoretical Framework	6
2.1.2	The Internal States of Atoms	9
2.1.3	The Adiabatic Evolution	10
2.1.4	Rabi Oscillations	12
2.1.5	Spontaneous Decay	13
2.2	The light forces on atoms	14
2.2.1	Light Pressure	14
2.2.2	Gradient force	14
2.2.3	Heating	15
3	Rubidium	17
3.1	Properties of Rubidium	18

3.1.1	Doppler Broadening	21
3.2	Saturated Absorption Spectroscopy	22
4	The Magneto-Optical Surface Trap (MOST)	28
4.1	Doppler-Cooling	29
4.2	The Repump Laser	31
4.3	The Magneto-Optical Trap	32
4.3.1	The MOT in 1D	33
4.3.2	The MOT in 3D	35
4.3.3	Magneto Optical Surface Trap	36
4.3.4	U-shaped wire	37
4.3.5	The Design of the U-Shaped Wire	42
4.3.6	The Magnetic Fields of the U-Shaped-Wire	45
5	Lab Setup of the MOST	49
5.1	Optical Setup	49
5.1.1	The Cooling and Repump Laser	50
5.1.2	The Laser Source for Dipole-Force Trapping	52
5.1.3	Laser Locking	52
5.1.4	Fabry-Perot Interferometer and Wavemeter	54
5.1.5	The Acousto Optical Modulators	54
5.2	The Vacuum Chamber	57
5.2.1	The MOST Finger	57

5.2.2	The Beam Steering into the Vacuum Chamber	58
5.3	The Computer Control	59
6	Characterisation of the MOST	61
6.1	Observation of the MOST	61
6.2	Loading of the Dipole Trap	65
7	Optical Tweezers	69
7.1	Outline	70
7.2	Feasibility	73
7.2.1	Dipole trapping of Alkali Atoms	73
7.2.2	The Role of the SLM	76
7.2.3	Radial and Axial Confinement	79
7.3	Ways to Single Atoms	83
7.4	Single Atom Detection and Transport	85
7.5	Conclusion	87
8	Isoplanatism	88
8.1	Introduction	88
8.2	Mathematical Formalism of Imaging	90
8.3	Isoplanatic Imaging Through a Thin Lens	96
8.4	Experimental Investigation	98
8.5	Conclusion	101

9	Optical Tweezers Setup	102
9.1	The Trap Setup	102
9.1.1	The Digital-Mirror-Device	103
9.1.2	The Optical Setup	105
9.2	The Imaging Setup	107
9.2.1	The EM-CCD Camera	109
9.2.2	Optical Filters and Shielding	111
10	Optical Tweezers Results	114
10.1	Absorption Imaging	114
10.2	Fluorescence Imaging	116
10.3	Summary	119
11	A High-Power Laser Diode for Dipole Trapping	121
11.1	The High-Power Laser Diode Module	122
11.2	Trap Depth of a focused Beam	126
11.2.1	Characterisation of the focussed Beam	127
11.3	The optical Diffuser	129
11.4	The Application of the Diffuser	131
11.4.1	Initial Conditions	131
11.4.2	The Optimisation Problem	133
11.4.3	Solving the Optimisation Problem	135
11.5	The experimental Check of the Setup	137

11.5.1 The stationary Diffuser	137
11.5.2 The rotating Diffuser	139
11.6 Feasibility Study	143
11.7 Outlook	144
12 Conclusion	147
12.1 Summary	147
12.2 Outlook	148
13 List of Publications	151
A Supplement to Theory	153
A.1 Rotating Wave Approximation	153
A.2 The Adiabatic States	155
A.3 Connection between Transition Rates and Rabi Oscillations	156
A.4 The Density Matirix Formalism including Decay	158
B Rubidium Reference Data	160
B.1 Universal Physical Constants	160
B.2 Values of Rubidium	161
B.3 Other Physical Values	161
B.4 Rubidium 87 D ₁ Transition	161
B.5 Rubidium 87 D ₂ Transition	162
C Pound-Drever-Hall Laser Stabilisation	163

D The Computer Control	167
E The Gaussian Beam Optics	170
E.1 The Electric Field	170
E.2 Beam Expansion	171
E.3 The Intensity and Power	172
E.4 The retro-reflected Beam	172
F The Collimator in the Diffuser Setup	174
Bibliography	176

Chapter 1

Introduction

A major challenge in experimental Quantum Physics is to control and manipulate individual quantum objects and combine them to larger systems. By studying these objects one is able to investigate fundamental properties of quantum mechanics, like superposition, entanglement and decoherence, which are topics of current research. Early experiments of quantum physics were limited to spectroscopy. Even though relatively early in 1928, there was the seminal paper by Einstein, Podolski and Rosen^[1], which discussed entanglement, it took some time till it was investigated experimentally^[2]. With the invention of the laser^[3], experimentalists gained a versatile tool for the manipulation of quantum systems. This opened up a new fields of physics way beyond spectroscopy. The first non-trivial manipulation of internal atomic states was coherent population trapping in the seventies^[4]. Soon there were many more examples of coherent manipulation of atomic states^[5,6].

There are two fundamentally different quantum systems: the relativistic objects,

like photons, and massive quantum objects, like atoms and ions, among many other. Though there are many experiments with single photons^[7,8], which are based on parametric down-conversion in nonlinear crystals. The road towards isolated matter-based quantum systems has proven much more challenging. Atoms tend to be elusive particles unless they are bound to solid state system, since they move about with speeds of hundreds of meters per second at room temperature. Their interaction with electric and magnetic fields is very small, so they need to be cooled prior to trapping. Ions, however, interact highly with electric fields and can be easily trapped^[9,10].

Many proposals for large-scale quantum computing^[11] or quantum simulation^[12] rely on the ability to deterministically manipulate, address and couple individual components of a quantum network. A quantum network combines matter based stationary quantum objects as nodes with quantum connections, like photons. These challenges can be addressed by the use of isolated quantum systems, such as trapped ions in quantum computing and entanglement experiments^[13,14], or dipole-trapped single neutral atoms^[15–18]. In an effective one-dimensional arrangement it has already been shown that the addressing and preparation of individual dipole-trapped atoms is possible and that those atoms can also be used as a phase preserving quantum register^[19]. To control a larger number of atoms in a two or three-dimensional quantum network, more elaborate techniques are required. Therefore several methods for handling individual atoms have been developed. The most promising techniques are the trapping of ion strings^[13,14,20], magnetically trapped neutral atoms

above atom chips^[21–24], individual atoms in steep optical dipole-force traps^[16,25–28], optical lattices^[17,29–31], and dipole-trap arrays created either by a matrix of micro lenses^[32], by holograms^[33], spatial light modulators^[34] or by a combination of these techniques^[31].

I propose to use a spatial light modulator (SLM)^[35,36] as an amplitude modulator to form the desired two-dimensional trapping potential, by directly imaging the SLM. This concept has much in common with the optical tweezers technique used in biology^[37], where light is used to manipulate small objects, like viruses, bacteria, or organic samples attached to micro-spheres. Here we apply this technique directly to cold atoms. This combination of the SLM with optical tweezers offers atom-chip like flexibility of individual-atom manipulation as well as magnetic-field free dipole trapping. Furthermore, with SLM refresh rates far above the loss rate of trapped atoms, such an arrangement might allow for the real-time manipulation of atoms.

The precise control of the atomic position could be applied to couple atoms with optical cavities to enhance the interaction between photons and atoms, which is very weak in free space. This can be done with single atoms in the optical regime^[38–42] as well as the microwave regime^[43,44], ions^[45], or even Bose-Einstein-Condensates(BEC)^[46,47]. Cavity quantum electro dynamics can also be used for the pairwise entanglement of atoms^[48]. This is one key to generate large cluster states, which are the essential resource for one-way quantum computing^[49].

The thesis is structured into four major parts. First, chapters 1-3 are the introduction, the theory, and the fundamental aspects of Rubidium. Second, chapters 4-6

discuss the cooling and trapping of a Magneto Optical Surface Trap. Third, chapters 7-10 discuss the properties of optical tweezers, as well as the implementation, and the experimental characterisation of them. Fourth, chapter 11 discusses the use of a high power laser diode for the use as a dipole trapping radiation source.

Chapter 2

Theory

This work mainly focusses on the use of light to trap and manipulate neutral atoms. Though the light forces on neutral atoms are usually very small, they prove to be extremely versatile tools when properly applied. The action of light onto a particle can have effects such as light pressure, gradient force, heating and manipulation of the internal states.

In particular, the light pressure and the gradient force can be used for cooling and trapping atoms, whereas heating limits the lowest achievable temperature. These forces act on the external degrees of freedom of the atom, i.e. the atomic motion.

In the following chapter, I derive the interaction of coherent light with atomic systems. This treatment is semi-classical, i.e. light is treated as a classical field. Only when atoms interact with one or few photons, e.g. with atoms coupled to single photons in a cavity, the quantum effects of the electromagnetic field have to be accounted for as well.

2.1 The Interaction of Light with a Single Atom

2.1.1 Theoretical Framework

The state of an atom is described by the state vector $|\psi\rangle_{atom}$, which includes the internal degree of freedom and the motional state of the atom. The state of the electromagnetic field is described by the state vector $|\psi\rangle_{elm}$. The dynamics of $|\psi\rangle = |\psi\rangle_{atom} \otimes |\psi\rangle_{elm}$ is determined by the Schrödinger equation

$$i\hbar \frac{\partial}{\partial t} |\psi\rangle = \hat{H} |\psi\rangle, \quad (2.1)$$

where \hbar is the reduced Planck constant and \hat{H} the Hamiltonian of the system. In general, the Hamilton operator can be split in the interaction part \hat{H}_{int} and the non-interacting part for the atom \hat{H}_{atom} and the electromagnetic field \hat{H}_{elm} : $\hat{H} = \hat{H}_{atom} \otimes \hat{I}_{elm} + \hat{H}_{int} + \hat{I}_{atom} \otimes \hat{H}_{elm}$. Lets consider the non-interacting part \hat{H}_{atom} first. This Hamiltonian can be divided into the centre of mass part \hat{H}_{cm} and the electronic part \hat{H}_{el} . (Not to be confused with the electromagnetic field Hamiltonian \hat{H}_{elm} .) If there are no external potentials acting on the atom the centre of mass Hamiltonian becomes:

$$\hat{H}_{cm} = \frac{1}{2m} \hat{\mathbf{P}}^2, \quad (2.2)$$

where $\hat{\mathbf{P}}$ is the momentum operator. The corresponding eigenstate is $|\mathbf{p}\rangle$, with an eigenvalue of \mathbf{p} . The internal states $|n\rangle$ are the eigenstates of \hat{H}_{el} with the eigenvalues

E_n , so that the electronic Hamiltonian can be written as:

$$\hat{H}_{el} = \sum_n E_n |n\rangle \langle n|. \quad (2.3)$$

The Hamilton operator \hat{H}_{elm} describes the evolution of the electromagnetic field, the full quantum mechanical treatment of the electromagnetic field is not required. Instead to describe absorption and induced emission it is sufficient to treat the problem semi-classically, that is to treat the atom quantum-mechanically and the electromagnetic field classically as:

$$\mathcal{E}(\hat{\mathbf{R}}, t) = \frac{1}{2} \left(\mathcal{E}_0(t) \exp \left(-i(\omega t - \mathbf{k} \cdot \hat{\mathbf{R}}) \right) + \mathcal{E}_0^*(t) \exp \left(i(\omega t - \mathbf{k} \cdot \hat{\mathbf{R}}) \right) \right), \quad (2.4)$$

where $\hat{\mathbf{R}}$ is the position operator acting on the external part of the atomic wave function and $\mathcal{E}_0(t)$ is the slowly varying amplitude of the electric field.

The interaction of neutral atoms with electromagnetic fields can be treated through a multipole expansion, of which the strongest is the dipole interaction:

$$\hat{\mathbf{D}} = \sum_i -e\hat{\mathbf{x}}_i \mathcal{E}(\hat{\mathbf{R}}, t), \quad (2.5)$$

where e is the charge of the electron and \mathbf{x}_i is the position operator of the i^{th} electron in the atomic reference frame. The action of (2.5) can be divided into the action on the motional state of the atom and the action on its internal state. I will investigate the action on the motional state first. The exponential $\exp(\pm i\mathbf{k} \cdot \hat{\mathbf{R}})$ acts as a

translation operator on the momentum eigenstates:

$$\langle p | e^{\pm i\mathbf{k}\cdot\hat{\mathbf{R}}} | p' \rangle = \delta(\mathbf{p} - (\mathbf{p}' \mp \hbar\mathbf{k})) \quad (2.6)$$

The significance of this equation is that the atomic momentum changes by $\hbar\mathbf{k}$ when absorbing or emitting one photon. The delta function ensures the conservation of momentum. The dipole operator (2.5) acts on the electronic states through the position operators \mathbf{x}_i , which couple states of opposite parity. The transition dipole moments are given by the following expression: $\mathbf{d}_{nm} = \sum_i \langle n | e \cdot \hat{\mathbf{x}}_i | m \rangle$. The full interaction Hamiltonian reads:

$$\hat{H}_{int} = \sum_{nm} \hat{\mathbf{d}}_{nm} \cdot \mathcal{E}(\hat{\mathbf{R}}, t). \quad (2.7)$$

Applying the rotating wave approximation (Appendix A.1) to the interaction term results in the simplified Hamiltonian:

$$\hat{H}_{rwa} = -\frac{\hbar}{2} \sum_{nm} \left(|n\rangle\langle m| \otimes \Omega_{n,m}(\hat{\mathbf{R}}) + |m\rangle\langle n| \otimes \Omega_{n,m}^*(\hat{\mathbf{R}}) \right), \quad (2.8)$$

for $(E_m - E_n) \approx \hbar\omega$, where $\Omega_{n,m}(\hat{\mathbf{R}}) = \Omega_{nm} e^{i\mathbf{k}\cdot\hat{\mathbf{R}}}$ is the Rabi frequency, with $\Omega_{nm} = \mathbf{d}_{nm} \cdot \mathcal{E}_0/\hbar$.

The first order transition amplitude can be calculated in the framework of first order perturbation theory^[50]:

$$L_{n,m} = -2\pi i \delta(E_{final} - E_{initial}) V_{n,m}, \quad (2.9)$$

where $V_{n,m} = -\frac{\hbar}{2} \Omega_{n,m}$ is the transition matrix element, $E_{initial} = \hbar\omega + E_n + \frac{\mathbf{p}^2}{2m}$ and $E_{final} = E_m + \frac{(\mathbf{p} + \hbar\mathbf{k})^2}{2m}$ is the total energy of the initial and final state respectively. The transition obeys the energy conservation through the delta function in (2.9). The energy balance reads: $\hbar\omega = \hbar\omega_{nm} + \frac{(\hbar\mathbf{k} + \mathbf{p})^2}{2m} - \frac{\mathbf{p}^2}{2m}$, where $\omega_{nm} = \frac{E_n - E_m}{\hbar}$ is the transition frequency, which simplifies to $\hbar\omega = \hbar\omega_{nm} + \frac{\hbar^2 \mathbf{k}^2}{2m} + \frac{\hbar\mathbf{k} \cdot \mathbf{p}}{m}$. The second term is the recoil energy $E_{recoil} = \frac{\hbar^2 k^2}{2m}$ and third term is the Doppler shift.

This derivation has been made while treating the electromagnetic field classically. As long as the fields which the atoms interact with have a high flux of photons, this is justified. However, the approach can easily be generalised to cases where atoms interact with only few or single photons, such as in Cavity Quantum Electrodynamics, by replacing the field amplitudes by field operators.

2.1.2 The Internal States of Atoms

In the previous subsection I showed that the exchange of photons with atoms result in a change of momentum as well as a change of the internal state of the atom. Here I investigate the change of the internal state further.

In general the energy difference between the electronic ground state and any of the excited states, $(E_0 - E_n) \approx eV$, neglecting fine and hyperfine splitting, is much

bigger than the thermal energy $k_b T \approx 0.026$ eV at room temperature. Thus atoms in thermodynamic equilibrium will be in the electronic ground state. Furthermore, it can be shown that the coupling of the electromagnetic field only leads to a population transfer when the frequency of the electric field, ω , is close to the atomic resonance $\omega_{nm} = \frac{E_n - E_m}{\hbar}$. Hence for most applications, it is sufficient to model the atom as a two-level system.

The interaction Hamiltonian (2.8) combined with the truncated bare energy Hamiltonian (2.3), $\hat{H}_{el} = E_g |g\rangle\langle g| + E_e |e\rangle\langle e|$ (where $|g\rangle$ denotes the ground state and $|e\rangle$ denotes the excited state), can be written in the following form after applying the rotating wave approximation, see Appendix A.1:

$$\hat{H}_{\text{RWA}} = \frac{\hbar}{2} \left(\Delta |g'\rangle\langle g'| + \Omega(t) |g'\rangle\langle e'| + \Omega^*(t) |e'\rangle\langle g'| - \Delta |e'\rangle\langle e'| \right), \quad (2.10)$$

where $\Delta = \omega - E_e/\hbar$ is the detuning of the electromagnetic field with respect to the atomic resonance and $|g'\rangle$ and $|e'\rangle$ are the ground and excited states in the rotating frame. The population dynamic is adiabatic, i.e. the population follows the evolution of the instantaneous eigenstates of this time dependent Hamiltonian, if the Rabi frequency changes slowly and the field is sufficiently detuned $\frac{1}{2} \frac{|\dot{\Omega}(t)\Delta|}{(\Omega(t)^2 + \Delta^2)^{\frac{3}{2}}} \ll 1$ and $\Delta \neq 0$ ^[5,51].

2.1.3 The Adiabatic Evolution

The matrix (2.10) can be diagonalized (see Appendix A.2), leading to the new eigenvalues of the system:

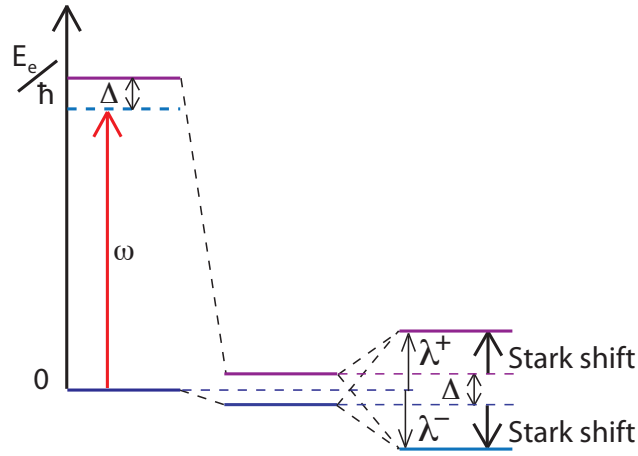


Figure 2.1 This picture shows the sequence in which the Stark shift is derived. First a red detuned laser couples two atomic level. Then the rotating wave approximation is applied, which shifts the energy levels symmetric around the zero energy. The eigenstates of the rotating wave hamiltonian are a mix of the original states. The energy difference to the previous states is the Stark shift.

$$\lambda^\pm = \pm \frac{\hbar}{2} \sqrt{\Delta(t)^2 + |\Omega(t)|^2}, \quad (2.11)$$

here and for the rest of the chapter I have omitted the time dependence of Δ and Ω , assuming that their values change much slower than the atomic population.

The new eigenvalues given by Eq. (2.11) are related to the Stark shift, which is caused by the perturbation of the atomic system by radiation. The adiabatic states are shifted with respect to the bare atomic states, see Fig. 2.1. For a red detuned laser beam, the energy of the ground state is shifted down by $\Delta\omega_{Stark} = \frac{\hbar}{2}(\sqrt{\Delta^2 + |\Omega|^2} + \Delta)$ and the excited state is shifted up by the same value. If the detuning is large compared to the Rabi frequency the expression can be expanded

into the following form.

$$\Delta\omega_{Stark} = \frac{\hbar \Omega^2}{2 \Delta} \quad (2.12)$$

This formula is the result for an idealised 2 level atom. For a real atom all allowed transitions have to be taken into account, since they can significantly contribute to the overall Stark shift.

2.1.4 Rabi Oscillations

The Hamiltonian (2.10) acting on the bare states leads to population oscillations between those states, the Rabi oscillations. The complex amplitudes $c_g(t)$ & $c_e(t)$ are obtained by solving the time dependent Schrödinger equation. The populations of the ground and excited states are given by:

$$|c_g(t)|^2 = \frac{\Delta^2}{\Omega_{eff}^2} + \frac{\Omega^2}{2\Omega_{eff}^2}(1 + \cos(\Omega_{eff}t)) \quad (2.13)$$

$$|c_e(t)|^2 = \frac{\Omega^2}{2\Omega_{eff}^2}(1 - \cos(\Omega_{eff}t)) \quad (2.14)$$

Here $\Omega_{eff} = \sqrt{\Omega^2 + \Delta^2}$ is the effective Rabi frequency, which is closely related with the transition matrix element in Eq. (2.9) (see Appendix A.3).

2.1.5 Spontaneous Decay

The treatment so far includes only absorption and stimulated emission. One way to include spontaneous emission within the system is the density matrix formalism, from which the optical Bloch equations^[52] can be derived for a two-level system (Appendix A.4). They describe the population dynamics of a driven two level system with decay. The population in the excited state is, if the population dynamics of the two level atom reach a steady state^[52]:

$$|c_e|^2 = \frac{1}{2} \frac{\Omega^2/2}{\Delta^2 + \Omega^2/2 + \Gamma^2/4}, \quad (2.15)$$

where Γ is the decay constant for the population in the excited state. The spontaneous scattering rate for an atom is $R_{scatt} = \Gamma|c_e|^2$, hence for far detuned light fields and sufficiently high Rabi frequency ($\Delta \gg \Omega \gg \Gamma$), which are used in dipole traps, the scattering rate becomes:

$$R_{scatt} = \frac{1}{4} \frac{\Omega^2}{\Delta^2} \Gamma \quad (2.16)$$

Comparing this result with equation (2.12) shows that for increasing detuning the scattering rates decreases faster than the Stark shift does. This is advantageous for optical dipole-force traps, as deep trap depth, i.e. a high Stark shift, and a low heating rate, i.e. low scattering rate, is generally required.

2.2 The light forces on atoms

2.2.1 Light Pressure

Each time a atom absorbs a photon, it receives a momentum kick of $\hbar\mathbf{k}$, according to equation (2.6). When the atom is only interacting with one laser beam, the momentum change is uni-directional and the atom feels a strong force. The highest scattering rate according to (2.15) is $R_{scat} = \Gamma/2$, so the atom will feel an acceleration of $a = R_{scat} \cdot \hbar\mathbf{k}/m$, which can be as high as 10^6 m/s² for Rubidium.

2.2.2 Gradient force

The gradient of a conservative potential U gives rise to the gradient force $\mathbf{F} = -\nabla U$. The case treated here is the potential created through the Stark shift (2.12). The Stark shift is negative when the light is red detuned with respect to the transition, i.e. the light is detuned to a longer wavelength, and hence the resulting potential is attractive. When the light is blue detuned the potential is repulsive. Hence red detuned light is generally used to create a trap. The potential depth tends to be rather weak, since it relies only on perturbation of the energy levels of the atom, but when the field intensity varies quickly, as for example in tightly focussed laser beams, the resulting force can be large. For example, a Rubidium atom confined in a cone shaped potential with a diameter of $20\ \mu\text{m}$ and a trap depth of $U_o/k_b = 1$ mK experiences an acceleration of 10^4 m/s².

2.2.3 Heating

As discussed in section 2.1.1 every time an atom scatters a photon, it receives a momentum kick of $\hbar\mathbf{k}$ for the absorption and for the emission. If absorption and emission occur in the same direction, for example absorption of a photon from one laser beam, and the subsequent stimulated emission by the same laser beam, then there is no net effect. But if the emission occurs in a random direction, which happens when the atom spontaneously emits the photon the effect leads to heating, as the atom receives a random momentum kick^[52]. For a single atom illuminated with a single laser beam, the process can be modelled as a random walk in momentum space, which has a standard deviation of \sqrt{N} about its mean, where N is the number of scattering events. The mean square of the momentum along the the z-axis is therefore given by:

$$\overline{p_z^2} = \eta(\hbar k)^2 R_{scatt} t, \quad (2.17)$$

here R_{scatt} is the scattering rate and $\eta = 1/3$ is a geometrical factor, since the scattering is randomly distributed in 3 dimensions. The same heating occurs for $\overline{p_x^2}$ and $\overline{p_y^2}$ as well.

In addition to the heating due to the spontaneous emission, there is a heating due to fluctuations in absorption, which is also described by Poissonian statistics. This leads to heating according to $\overline{p_z^2} = (\hbar k)^2 R_{scatt} t$. This configuration also creates light pressure, as only one laser beam is present. However if the atom is simultaneously

illuminated by two counter propagating laser beams, the light pressures cancel out and only the heating remains.

The total heating, caused by absorption and emission, is

$\overline{p_x^2} + \overline{p_y^2} + \overline{p_z^2} = 2(\hbar k)^2 R_{scatt} t$. With the recoil energy $E_{recoil} = \frac{\hbar^2 k^2}{2m}$, this leads to a heating rate of:

$$R_{heat} = 2 \frac{E_{recoil}}{k_b} R_{scatt}, \quad (2.18)$$

where k_b is the Boltzmann constant. This result states that the average heating per scattering event is $2E_{recoil}$, since the atom receives two momentum kicks per scattering event. If only the spontaneous emission had been taken into account, the heating rate would have been underestimated by a factor of 2.

Chapter 3

Rubidium

Alkali atoms have a simple electronic structure, hence they are often chosen for cooling and trapping experiments. For instance, Doppler cooling requires a closed cooling transition, i.e. the atom must decay to a state which does belong to the cooling transition, because it relies on scattering many photons of an atom and a complicated level structure therefore would limit the number of scattering events. Also, for coupling atoms to an optical cavity, which is the eventual goal of this project, a simple atomic structure is favourable. These criteria are met by Alkali metals, of which Rubidium has its cooling transition at a convenient wavelength for widely available high power diode lasers, and a small nuclear spin, which leads to a small number of Zeeman sub-levels. Hence I choose to use Rubidium for this project.

In this Chapter the spectroscopic properties of the Rubidium, which are required for the magneto-optical trap, are treated and doppler free absorption spectroscopy,

which is used to lock the laser systems, is explained.

3.1 Properties of Rubidium

Rubidium is a highly reactive alkali metal, which has two abundant naturally occurring isotopes, ^{85}Rb (72.2%) and ^{87}Rb (27.8%). At room temperature it is solid, but its vapour pressure of $33 \cdot 10^{-7}$ mbar is sufficiently high for spectroscopy.

The Rubidium atom has one $5s$ valence electron. This electron is responsible for the chemical and spectroscopic properties of Rubidium. The other electrons form a closed shell and contribute only through the shielding of the nucleus. This significantly changes the energy levels of the valence electron from the corresponding hydrogen levels. Thus, the energy levels for different electronic orbital angular momenta L are not degenerate. The energy gap between the $5s$ and $5p$ state is 1.589 eV and is addressable by optical radiation in the near infrared at about 780 nm^[53]. This transition is used in the trapping scheme and therefore deserves special attention.

The angular momentum of the ground state $L=0$, combined with the electron spin $S=\frac{1}{2}$, results in a electron angular momentum of $J=\frac{1}{2}$. The excited state has an electronic angular momentum of $L'=1$. Therefore the total electronic angular momentum is $J'=\frac{1}{2}$ or $J'=\frac{3}{2}$. These two levels are separated due to the fine structure splitting by about 15 nm. This large gap in wavelength is sufficient to treat those two levels separately. The corresponding lines are known as the D_1 -line ($J'=\frac{1}{2}$) at 795 nm and the D_2 -line ($J'=\frac{3}{2}$) at 780 nm.

In addition to the fine structure, the hyperfine structure has an significant effect

on the level structure. The two isotopes have a nuclear spin of $I_{(85)} = \frac{1}{2}$ and $I_{(87)} = \frac{3}{2}$. This results in a rich hyperfine-structure, see Fig. 3.4 and Fig. 4.1 for ^{87}Rb . The resulting quantum numbers are summarised in the following table:

Isotope	Nuclear Spin I	Ground State F	Excited State D_1 F'	Excited State D_2 F'
85	5/2	2,3	2,3	1,2,3,4
87	3/2	1,2	1,2	0,1,2,3

Optical transitions between the ground and excited states are possible. The transition rules for optical dipole transitions^[52] are:

$$\Delta L = \pm 1 \quad (3.1)$$

$$\Delta M_L = 0, \pm 1 \quad (3.2)$$

The rest of the electronic spin and nuclear spin quantum numbers do not change: $\Delta S, \Delta M_S, \Delta I, \Delta M_I = 0$, since the optical dipole transition is purely an orbital change of the electron. These restraints translate into the following transition rules expressed in the basis of total angular momentum F, which is the sum of the total electronic angular momentum J and the nuclear spin I^[52]:

$$\Delta F = 0, \pm 1 \quad (3.3)$$

$$\Delta M_F = 0, \pm 1 \quad (3.4)$$

$$\Delta M_F \neq 0 \quad \text{if } \Delta F = 0 \text{ and } M_F = 0$$

The transition strengths vary between the allowed transitions, see reference^[54].

Optical Doppler cooling, which will be discussed in detail later in this thesis, requires a closed cycling transition. This means that the excited state only decays back into the same state it was excited from. This would correspond to a perfect two level atom. For example when a ^{87}Rb atom in the $F=2$ state is driven with σ^+ light, that is right hand circular polarised light in the reference frame of the atom, it can only cycle in the $F=2 \leftrightarrow F'=3$ transition of the D_2 -line and can not decay into the $F=1$ state, hence it resembles a two level atom. This applies similarly for the $F=3 \leftrightarrow F'=4$ transition of the ^{85}Rb D_2 -line, but there is no such transition within the D_1 lines. This is why the D_2 line is used for the Doppler cooling. Additionally ^{87}Rb has fewer hyperfine sub-states than ^{85}Rb , which is advantageous in the context of addressing the individual sub states. Thus ^{87}Rb is used in the work presented in this thesis.

3.1.1 Doppler Broadening

The atoms used for spectroscopy are at room temperature. Hence they have a significant velocity, and their spectrum is thus Doppler broadened. The absolute value of their velocity, i.e. their speed, is given by the Boltzmann distribution:

$$f_D(v) = \sqrt{\frac{2}{\pi}} \left(\frac{M}{k_B T} \right)^3 v^2 \exp\left(-\frac{Mv^2}{2k_B T}\right) \quad (3.5)$$

Here M is the mass of the atom, k_B the Boltzmann constant and T the temperature. This distribution has its most likely velocity at:

$$v_D = \sqrt{\frac{2k_B T}{M}} \quad (3.6)$$

The above equation is of importance if only the magnitude of the velocity is of interest. However, the Doppler shift is determined by the velocity component along the propagation axis of the light. For only one component the distribution is slightly different:

$$f_D(v) = \sqrt{\frac{M}{2\pi k_B T}} \exp\left(-\frac{Mv^2}{2k_B T}\right) \quad (3.7)$$

This is a normal distribution centred around zero velocity. It has a width of $\sigma_v = 2\sqrt{k_B T/M}$. In the reference frame of the moving atom, the Doppler shift is given by:

$$f(v) = f_0 \left(1 - \frac{v}{c}\right), \quad (3.8)$$

where c is the speed of light in vacuum, and f_0 is the Bohr frequency of the atomic transition. Hence the Doppler broadening is also normally distributed with a width of $\sigma_D = \sigma_v \cdot \frac{f_0}{c}$. In the following table there are a couple of velocities listed for some important temperatures. The doppler shifts are calculated for the D_2 line of ^{87}Rb .

Temperature	Value	modal velocity v_D [m/s]	velocity distribution width σ_v [m/s]	Doppler broadening σ_D [MHz]
Dispenser	700	367	518	704
Room Temp	300	240	318	434
Doppler Limit	143μ	0.166	0.234	0.300
Recoil Limit	0.37μ	0.0084	0.0119	0.015

At room temperature the Doppler broadening is much wider than the natural line width of 6 MHz. In fact it has the same magnitude as the spacing of the upper hyperfine levels. To resolve these lines a Doppler free spectroscopic method has to be applied. The next section will introduce the saturated absorption spectroscopy.

3.2 Saturated Absorption Spectroscopy

For most atomic species the linewidth at room temperature is dominated by the Doppler broadening. Rubidium for example has a natural linewidth (FWHM) of

6.1 Mhz and at room temperature the Doppler width (FWHM) is 512 MHz. As the hyperfine structure is only about 400 MHz wide, it is impossible to resolve it. The remedy is to use Doppler free spectroscopy. Here I choose to use 'saturated absorption spectroscopy', which is a pump-probe scheme where a strong pump beam modifies the atomic sample by burning a spectral hole in the absorption profile monitored by the probe laser. Fig. 3.1 shows the principle scheme of the setup.

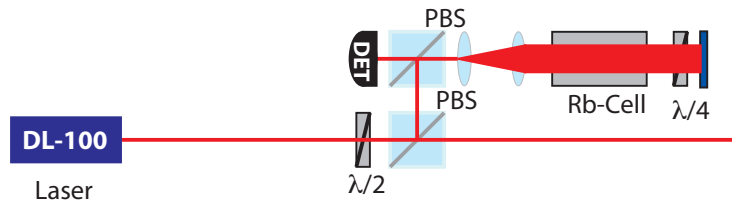


Figure 3.1 Scheme of the pump probe setup. A half-wave plate in combination with a polarising beam splitter (PBS), splits a part of the laser beam into the spectroscopy setup. There the beam is widened by a telescope and propagates through a Rubidium cell. A quarter wave plate, through which the beam propagates twice, acts as a half wave plate to rotate the polarisation axis of the retro reflected probe beam, so that the beam will reach the detector, behind the second PBS.

To understand saturated absorption spectroscopy, the concept of velocity classes of atoms is very useful. The velocity class v contains the atoms with a velocity component v along the propagation axis of the probe beam, see Fig. 3.2 and is distributed according to Eq. (3.7). Each velocity class experiences a Doppler shift, according to Eq. (3.8). Hence the probe beam, which is detuned by Δf with respect to the resonance frequency f_0 , probes the velocity class $v_{probe} = -\frac{\Delta f}{f_0}c$.

The pump beam is counter-propagating with respect to the probe beam, hence

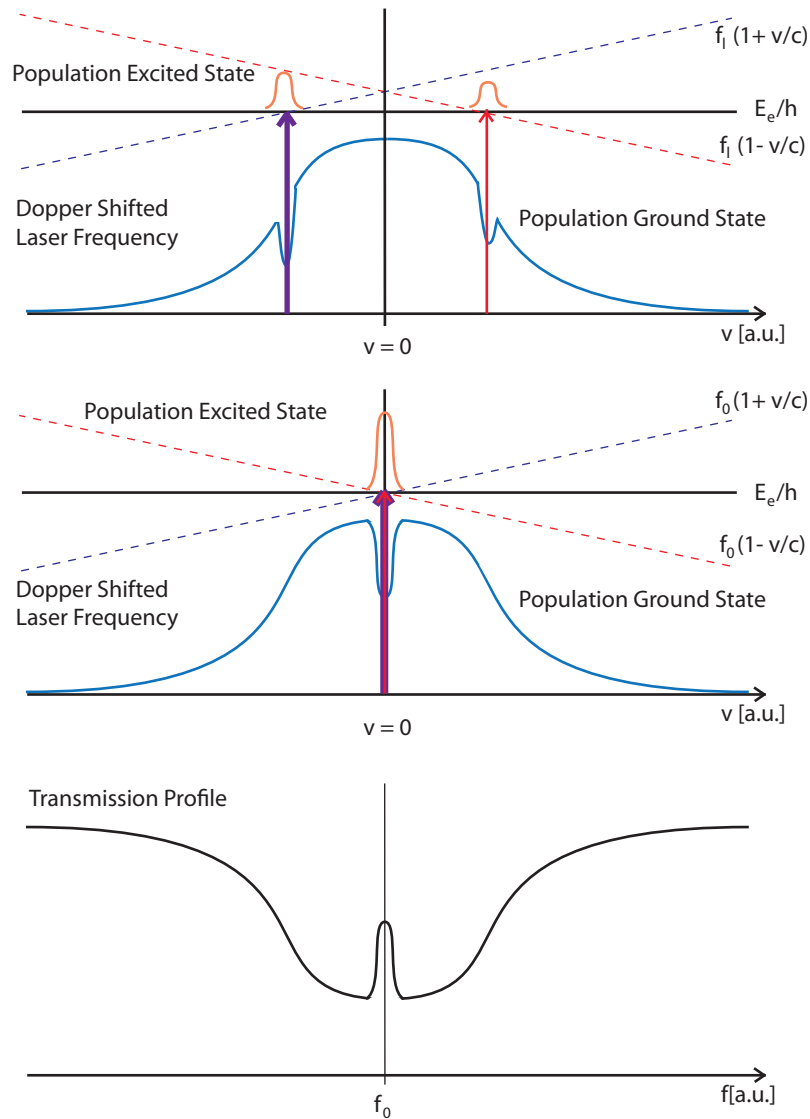


Figure 3.2 The top figure shows the absorption of a counter-propagating pair red detuned laser beams by atoms which are in different velocity classes. Due to the Doppler-shift the beams excite different atoms. Whereas, in the middle figure, the laser beams are on resonance, hence they both excite atoms with zero velocity. That leads to a reduction of absorption on resonance, lower figure.

the pump beam interacts with the opposite velocity class $v_{pump} = \frac{\Delta f}{f_0}c$. In the setup according to Fig. 3.1 the probe beam is simply the reflected pump beam. The pump

beam depletes the population in the ground state of the velocity class v through a combination of saturating the transition as well as optical hyperfine pumping^[55,56], which is called spectral hole burning.

Since the pump and the probe beam are counter propagating, they always interact with different velocity classes except for $\Delta f = 0$ where they interact with the same velocity class. The probe beam then detects the spectral hole burned by the pump laser. Its width is given by saturation broadening and the effect of optical pumping, so it is on the order of a few natural line widths (6MHz) and hence much narrower than the hyperfine structure of Rubidium (≈ 100 MHz), which is resolved with this technique, see Fig. 3.4.

Compared to a single transition, spectra with multiple lines are richer, because there are additional cross-over lines. These occur exactly in the middle of two absorption lines. Consider the case that there are two excited states present with the resonance frequencies f_1 and f_2 . The pump beam burns two spectral holes at $v_{pump,1} = \frac{\Delta f_1}{f_1}c$ and $v_{pump,2} = \frac{\Delta f_2}{f_2}c$, one for each excited state. When the laser frequency is exactly in the middle of the two transitions $f_l = (f_1 + f_2)/2$, the two spectral holes are in the opposite velocity classes $v_{pump,1} = -v_{pump,2}$. The pump and probe beams interact with opposite velocity classes: $v_{probe,1} = -v_{pump,1}$ and $v_{probe,2} = -v_{pump,2}$. Hence the pump and probe beam are interacting with the same velocity classes, since $v_{probe,1} = v_{pump,2}$ and $v_{probe,2} = v_{pump,1}$. This effect leads to another feature in the observed spectrum, the cross-over line, see Fig. 3.3.

The spectrum of Rubidium has three primary lines and three crossover lines for

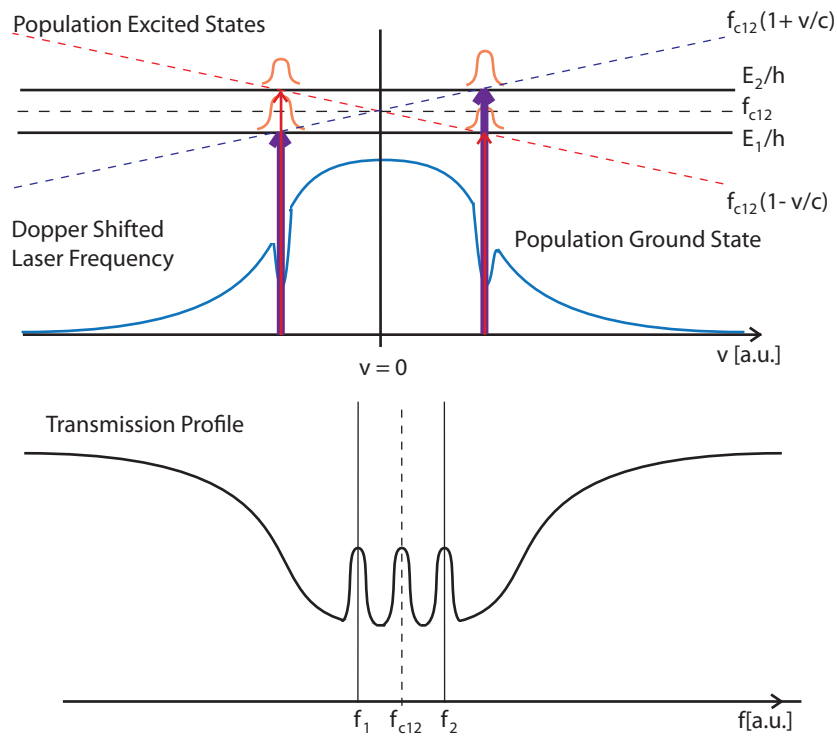


Figure 3.3 In the top figure a pair of counter-propagating laser beams illuminates an ensemble of atoms with two excited states. Due to the doppler shift each laser beam interacts with both excited states. If the detuning is exactly half way between the resonances they interact with the same velocity class. This leads to the appearance of an additional dip in the absorption profile, the cross over dip (lower figure).

each ground state ($F=1$ and $F=2$), see Fig. 3.4. The Doppler free spectroscopy is used for laser stabilisation of the cooling and repump lasers, for which the cross over lines are convenient, since they bridge the gap between the natural lines. For example the cooling laser is looked onto the cross over line 2/3 and an acousto-optic modulator then shifts the frequency close to the $F=2 \leftrightarrow F'=3$ transition for the laser cooling.

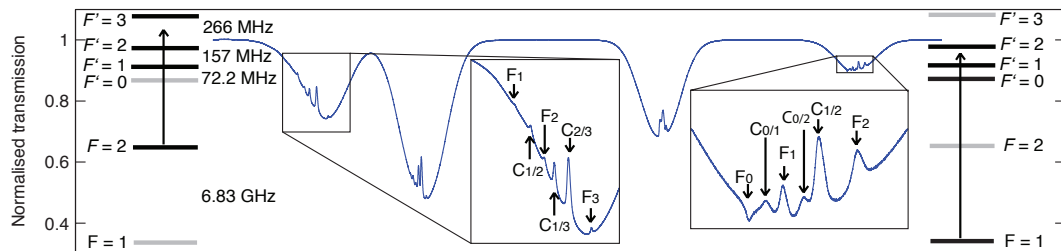


Figure 3.4 This figure (taken from^[57]) shows the full spectrum for the D2 line of Rubidium. The middle two peaks are ^{85}Rb and the outer two ^{87}Rb . These peaks are split by the hyperfine shift in of the ground state. For ^{87}Rb the spectrum is showed in detail, so the dips including the cross over dips become more appeared.

Chapter 4

The Magneto-Optical Surface Trap (MOST)

The goal of this project is to trap and manipulate single atoms in optical tweezers. The initial temperature of the atoms is about 300 K. The trap depth of optical dipole traps is typically less than 1 mK and hence the atoms have to be cooled prior to loading them into the trap. A magneto optical surface trap pre-cools and captures the atoms. This technique relies on resonant photon scattering, which changes the atom momentum by a small amount per scattering event, but if repeated often enough it significantly slows down the atoms. In this chapter I will show how this can be used to cool and trap atoms.

4.1 Doppler-Cooling

When an atom absorbs a photon its momentum is changed by $\hbar\mathbf{k}$ in the direction the photon was travelling (2.6). Repetitive scattering reduces the velocity significantly, provided the laser beam points in the opposite direction the atom travels. To cool an atom in one dimension a pair of red detuned counter propagating beams is required. Since the light is red detuned the Doppler effect shifts the light closer to resonance for photons moving into the opposite direction as the atom, whereas if photons travel into the same direction as the atom the light is shifted further away from resonance. Hence the atom is more likely to scatter photons that move into the opposite direction, which results in a viscous force on the atom and hence cools them. This scheme can easily be expanded to three dimensions, by using 3 mutual orthogonal pairs of counter propagating beams. This method is called Doppler Cooling and was first proposed by Hänsch and Schawlow in 1975^[58]. The first cooling was demonstrated by Chu in 1985^[59].

The force experienced by an atom scattering photons of one laser beam is the photon momentum $\hbar\mathbf{k}$ multiplied by the scattering rate, which is the product of the decay constant Γ and the population of the excited state $|c_e|^2 = \frac{1}{2} \frac{\Omega^2/2}{\Delta^2 + \Omega^2/2 + \Gamma^2/4}$, see Eqn. (2.15). Including the Doppler-shift the following equation describing the the force is obtained for each beam:

$$F(\Delta \pm kv) = \pm \frac{1}{4} \hbar k \Gamma \frac{\Omega^2}{(\Delta \mp kv)^2 + \Gamma^2/4 + \Omega^2/2}, \quad (4.1)$$

where Δ is the detuning from the resonance in the lab-frame, kv is the doppler shift of the resonance of atoms with velocity v and Ω is the Rabi frequency, which relates to the saturation intensity I_{sat} as:

$$\Omega^2 = \frac{\Gamma^2}{2} \frac{I}{I_{Sat}}, \quad (4.2)$$

Using the relation and the assumption that $I/I_{sat} \ll 1$ one can rewrite the force in terms of the saturation intensity:

$$F(\Delta \pm kv) = \pm \frac{1}{2} \hbar k \Gamma \frac{I/I_{Sat}}{\frac{4}{\Gamma^2} (\Delta^2 \mp kv)^2 + 1} \quad (4.3)$$

To obtain a function of the force that a pair of counter propagating beams exerts on an atom the two forces (4.3) with opposite k have to be added, to account for the two counter-propagating beams. The first order Taylor expansion around zero velocity yields the equation:

$$F = 4\hbar k^2 \frac{I}{I_{sat}} \frac{2v\Delta/\Gamma}{(\frac{4}{\Gamma^2}\Delta^2 + 1)^2} \quad (4.4)$$

It is valid for small velocities, where the force is proportional to the velocity, and thus it acts as a frictional force. The cooling force depends on the detuning Δ and reaches its maximum with respect to detuning at $\Delta = \gamma/2$. It appears to be continuous in this treatment, but one has to take into account that the absorption and spontaneous emission of photons result in shot noise, which contributes to heating, see chapter 2.2.3. This heating limits the doppler cooling to the temperature at

which the heating rate equals the cooling rate. At a detuning of $\Delta = \Gamma/2$ the lowest temperature can be reached^[52], the Doppler cooling limit:

$$T_{Doppler} = \frac{\hbar\Gamma}{2k_B}, \quad (4.5)$$

For Rubidium it is $T_D = 145 \mu\text{K}$. Other optical cooling methods, for example polarisation gradient cooling^[54], are capable of reaching temperatures below this limit, e.g. which are as low as the temperature corresponding to the energy of a single photon recoil $T_{Rec} = 0.47 \mu\text{K}$.

4.2 The Repump Laser

In section 4.1 I only considered the cooling for two level atoms, as this is sufficient to explain Doppler cooling. Most atoms however have multiple levels, which can be populated during the cooling. Generally atoms which are pumped out of the cooling cycle will be lost. The lack of a closed cooling transition, will render the cooling inefficient. To close those decay channels, the lost population can be optically pumped back into the cycling transition.

In case of ^{87}Rb D_2 line, see Fig. 4.1, the atomic levels exhibits a hyperfine structure. The ground state splits in two levels and the excited state splits in four levels. For cooling the transition between $F=2$ and $F'=3$ is chosen. It is a closed transition, but there exists the small possibility of off-resonant excitation into the $F'=2$ level, which can decay into the $F=1$ ground state. I use a second laser, the

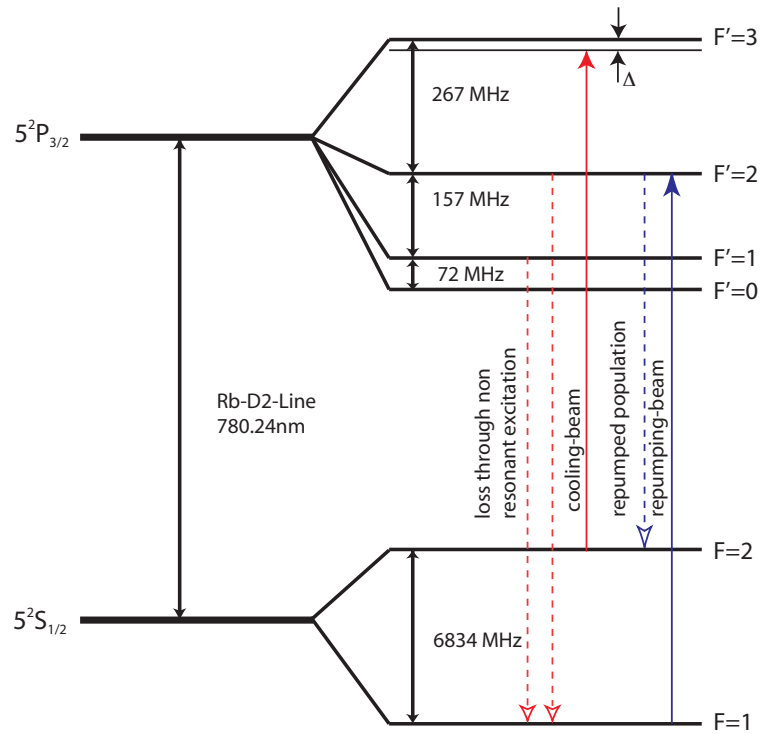


Figure 4.1 This figure shows the cooling transition between the $F=2$ and $F'=3$ level, indicated by the red line, and the re-pumping beam by the blue line. The cooling laser depopulates the $F=2$ through off-resonant excitation of the $F'=2$ and $F'=1$ level. This population is transferred back into the $F=2$ level by the re-pump excitation.

repumper, to pump the lost population back into the $F=2$ ground state, as shown in Fig. 4.1.

4.3 The Magneto-Optical Trap

Doppler cooling as such does not trap the atoms, since there is no spatial dependence of the force. However its extension, the **Magneto-Optical Trap**, includes a magnetic

field, which induces a spatial varying detuning and hence the spatially varying light pressure leads to trapping. The MOT requires the atoms to have a multiplet of excited states, which experience the Zeeman shift:

$$E_{Zeeman} = \mu_B g_F m_F B_z, \quad (4.6)$$

where μ_B is the Bohr magneton, g_F is the hyperfine gyromagnetic ratio, m_F is the projection of the state vector on the axis of the magnetic field B_z . The magnetic field itself can be used for trapping, but this results in very shallow potentials, here however, it will only be used to detune the transitions.

4.3.1 The MOT in 1D

I consider the one dimensional case first for the simple model of a transition between $J=0$ and $J'=1$ with no hyperfine splitting, i.e. $I=0$, to explain the mechanism of the MOT.

As for doppler cooling, there is a pair of red-detuned counter-propagating laser beams orientated along the z -axis. A magnetic field in the form $B_z(z) = B_0 \cdot z$ is added to the light fields. It induces a Zeeman shift, that depends linearly on the distance. The helicity of the beams must be chosen so that only the transitions with the energy lowered through the Zeeman shift are driven. Since the frequency of the cooling beam is red detuned the atom is more likely to absorb photons travelling towards the centre of the trap. The force on the atoms resulting from the light pressure of the counter-propagating beams is:

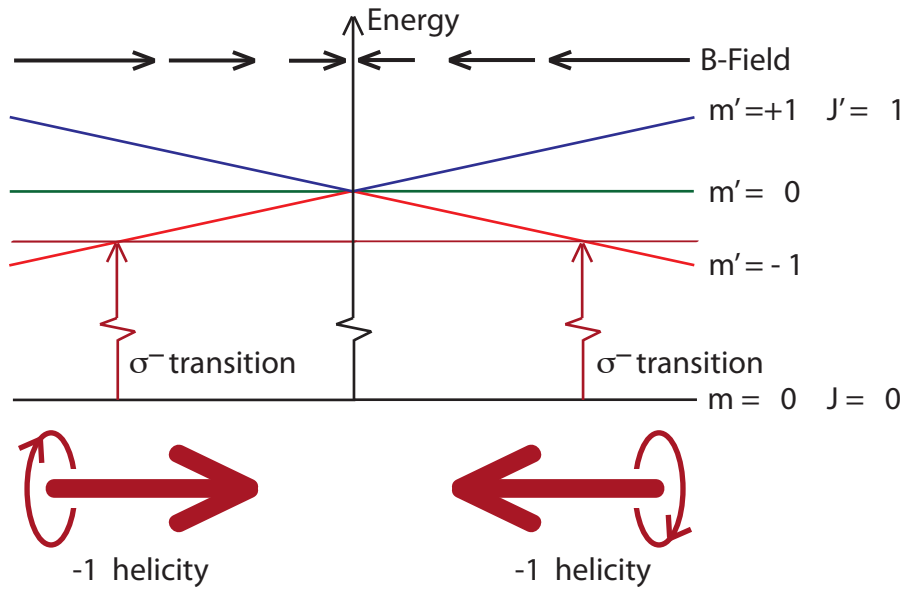


Figure 4.2 The mechanism of the MOT in 1-d is shown. The horizontal axis corresponds to a displacement along the z -axis of the trap. A magnetic field, splits the triplet of the excited state. It defines the quantisation axis, hence the quantisation axis is inverted at $z=0$. The two counter-propagating laser beams are red detuned with respect to the atomic transition frequency. Since they are orientated along the direction of the magnetic field they drive the σ^- -transitions of the atom. The corresponding σ^+ -transitions are disfavoured compared to σ^- -transitions, due to the larger detuning. Hence the atoms feel a effective force pushing them back into the centre.

$$F_{MOT} = F(\Delta - kv) - F(\Delta + kv), \quad (4.7)$$

where $\Delta = \omega - (\omega_0 + \beta z)$ includes the detuning of the magnetic field βz , where $\beta = \frac{1}{\hbar} \mu_B g_F m_F B_0$ is the change of the atomic frequency ω depending on the displacement along the z -axis. Expanding the force in kv and βz and using $\frac{\partial F}{\partial kv} = -\frac{\partial F}{\partial w}$ and $\frac{\partial F}{\partial \beta z} = -\frac{\partial F}{\partial w}$ it can be written as:

$$F_{MOT} = -2 \frac{\partial F}{\partial \omega} (kv + \beta z), \quad (4.8)$$

and $\frac{\partial F}{\partial \omega} = 2\hbar k \frac{I}{I_{sat}} \frac{2v\Delta/\Gamma}{(\frac{4}{\Gamma^2}\Delta^2 + 2I/I_{sat} + 1)}$. This equation reduces to Doppler cooling (Eq. 4.4) when the magnetic field is set to zero. Therefore the MOT simultaneously cools and traps atoms. This method is able to capture a significant part of atoms from a vapour at room temperature, hence the MOT is widely used for the initial trapping and cooling in many experiments.

4.3.2 The MOT in 3D

The extension of this scheme from one to three dimensions is straight forward. In three dimension the scheme requires 3 mutual orthogonal pairs of laser beams overlapping at one point. This point has to overlap with the point of $\mathbf{B} = 0$. But due to the restriction of the 3rd Maxwell's equation, $\nabla \cdot \mathbf{B} = 0$, not all of the 3 components can have the configuration as in Fig. 4.2. Instead a quadrupole field can be used, where one of the components has the opposite orientation $\frac{\partial B_x}{\partial x} = \frac{\partial B_y}{\partial y} = -2 \frac{\partial B_z}{\partial z}$ at $(x, y, z) = 0$. Two parallel coils produce this field to a good approximation when the current flows through them in opposite directions. The axis of these coils defines the z-axis of the field and the to it orthogonal plane is spanned by the x-axis and the y-axis. The MOT requires three pairs of cooling beams, overlapping at $(x, y, z) = 0$. Two pairs are in the x-y plane and have the same helicity. A third pair is orientated along the z-axis and has opposite helicity of the other two beam pairs.

The MOT will still work with atoms that have a more complicated level struc-

ture, such as Rubidium, as long as the addressable transitions experience a similar differential Zeeman shift like the simple $J=0 \leftrightarrow J'=1$ model.

4.3.3 Magneto Optical Surface Trap

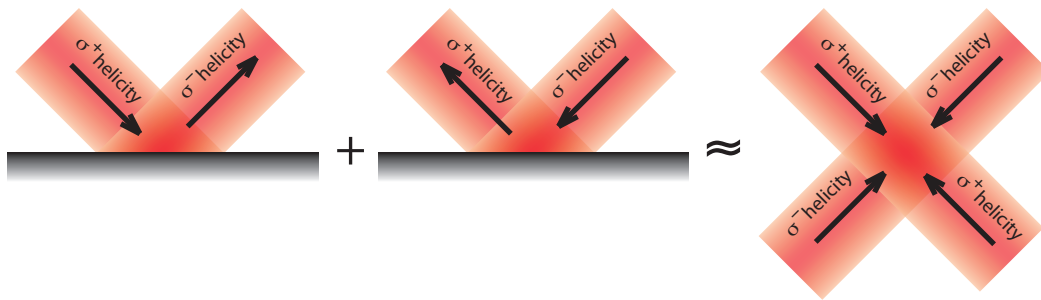


Figure 4.3 Scheme of an incoming beam from the left, which is reflected off a mirror surface with an angle of incidence of 45° . Through the reflection the helicity of the light is changed. There is a triangular area where the incoming and reflected beam overlap. In this region full 3-d cooling is possible, when a horizontal beam is included as well.

In most experiments MOTs are realised with three pairs of counter-propagating beams that overlap in free space. Here however, it is necessary that the MOT operates close to a mirror surface, due to the application of the optical tweezers. The mirror blocks the beam path of two beams, hence the use of three counter-propagating beam pairs is not feasible and a different approach has to be taken.

A laser beam hitting the mirror surface with an angle of 45° will be reflected off the mirror, see Fig. 4.3. The incoming and outgoing beam overlap close to the mirror surface whilst propagating in orthogonal directions. This creates two effective beams. Adding a second beam anti-parallel to the outgoing beam adds another two effective

beams. The reflection of the mirror surface changes the helicity of the beams, hence the two incoming beams must have opposite helicity to form two effective MOT beam pairs, see Fig. 4.3. These beams correspond to the x-beam pair and the z-beam pair in the standard configuration. A third beam pair propagating perpendicular to the other two beams and parallel to the mirror surface completes the MOT-beam configuration of three pairs of counter-propagating beams.

Since the z-axis is inclined with an angle of 45° with respect to the mirror surface, the pair of anti-Helmholtz coils has also be orientated along this angle. Although simple in theory in practice this configurations limits the optical access.

4.3.4 U-shaped wire

An alternative to anti-Helmholtz coils creating the magnetic quadrupole field is to superimpose the magnetic field of an u-shaped wire with a homogeneous bias field^[60–62], see Fig. 4.6. This arrangement is preferable over a pair of inclined anti-Helmholtz coils, as it does not restrict the optical access significantly.

To illustrate the principle of this technique I first treat the 2-dimensional case of an infinitely long thin wire. For the consistency with the following sections I choose a new coordinate system for the fields, in which the horizontal wire is aligned with the y-axis. The z-axis is the vertical axis with respect to the lab and hence perpendicular to y. The magnetic field in the plane perpendicular to the wire is

$B_r = \frac{\mu_0 I}{2\pi r}$, where $r = \sqrt{x^2 + z^2}$, or in vectorial form:

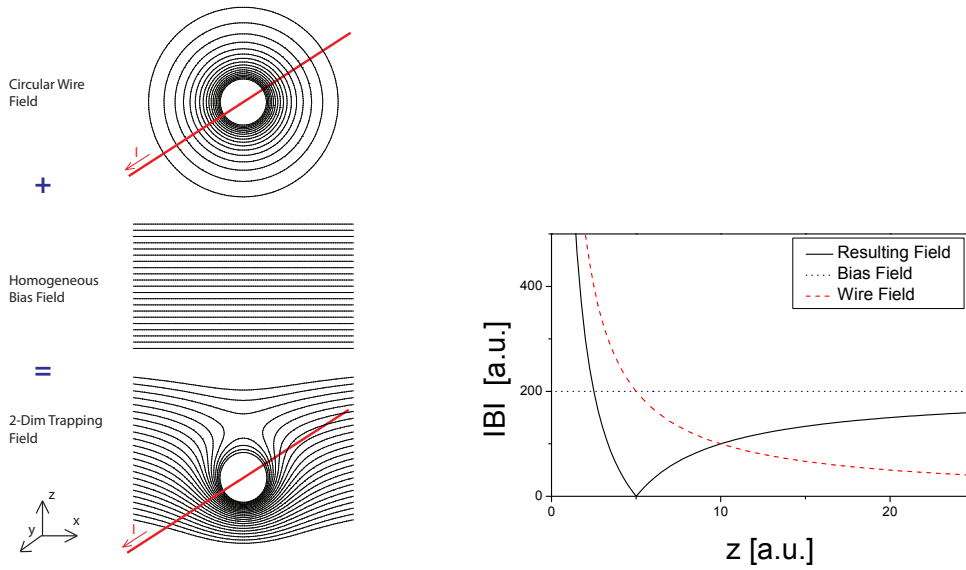


Figure 4.4 On the left hand side the principle of a line trap is shown: The combination of the circular field of a straight wire and a constant magnetic field results in a field which resembles a quadrupole-field near the point where the total field-strength is zero. The point where the total field is zero can be changed by varying the current which runs through the wire, or by changing the constant bias-field. The graph on the right shows the absolute value of the magnetic field along the z -axis. It is 0 where the circular field and the the bias field have the same magnitude but opposite orientation.

$$\mathbf{B}_{\text{circ}} = \tilde{B}_c \begin{pmatrix} \frac{z}{r^2} \\ -\frac{x}{r^2} \end{pmatrix}, \quad (4.9)$$

where $\tilde{B}_c = \frac{\mu_0}{2\pi}I$ for simplicity. It should be noted that \tilde{B}_c is not a magnetic field but has the dimension of a magnetic field times distance. The circular field is now

superposed with a homogenous B-Field \mathbf{B}_{bias} , pointing along x

$$\mathbf{B}_{\text{bias}} = B_b \begin{pmatrix} -1 \\ 0 \end{pmatrix}, \quad (4.10)$$

which results in the total field

$$\mathbf{B}_{\text{tot}} = B_c \begin{pmatrix} \frac{z}{r^2} - \frac{B_b}{B_c} \\ -\frac{x}{r^2} \end{pmatrix}. \quad (4.11)$$

As can be seen from (4.11) there is a point where the total field is zero, because the homogeneous field exactly cancels the circular field. This happens at $x = 0$ and $z = \tilde{B}_c/B_b$. Hence the centre of the trap can be adjusted by changing the relative magnitudes of the two superimposed magnetic fields. Furthermore the components of the gradient around the centre of the trap is

$$\partial_u \mathbf{B}_{\mathbf{u}} = -\frac{B_b^2}{\tilde{B}_c} \quad (4.12)$$

and

$$\partial_v \mathbf{B}_{\mathbf{v}} = \frac{B_b^2}{\tilde{B}_c}. \quad (4.13)$$

Here the coordinates u and v are the symmetry axis of the field, which are rotated by 45° against the cartesian coordinates x, z , such that $\hat{u} = \frac{1}{\sqrt{2}}(\hat{x} + \hat{z})$ and $\hat{v} = \frac{1}{\sqrt{2}}(-\hat{x} + \hat{z})$, see Fig. 4.5. Hence the gradient of the field can be controlled by

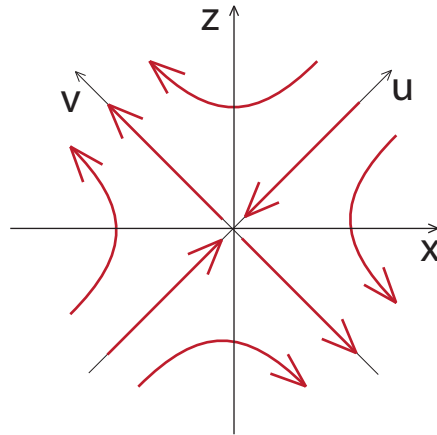


Figure 4.5 Scheme of the magnetic field lines in the centre of the quadrupole field above the wire. The symmetry axis u and v are rotated against the cartesian frame x, z .

changing the strength of the two fields together. This configuration traps in two dimensions, but not in the direction parallel to the wire, see Fig. 4.4.

To produce a potential in three dimensions the wire is bent into a U-shape, see Fig. 4.6. The only sources for the y -component of the field are the two legs in the x -direction. In the y -symmetry plane of the trap, which is defined by $y=0$, the y -components of the two legs cancel exactly. Hence the trap lies in this plane. The fields which have non-vanishing x -components are the bias field and the field from the centre wire, which is the short wire along the y -axis similar to the 2d-case, see Fig. 4.4. Fields in the z -direction are produced by both the legs and the centre wire. The z -field component of the centre wire has to be compensated by the z -component of the legs.

The relation between the fields of the centre wire and the legs couples the degree of freedom in the x -direction and the z -axis. Hence it is not possible to independently

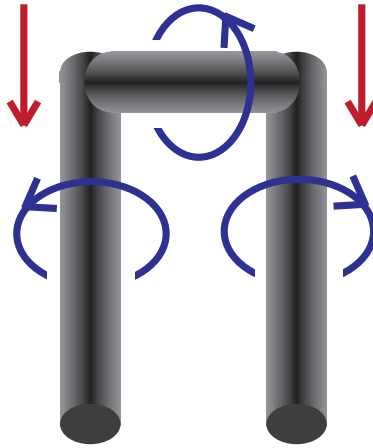


Figure 4.6 Scheme of the U-wire and the magnetic fields. The u-wire consists of the two legs on the left and the wire connected by the central wire on the top. The blue arrows indicate the magnetic field of the individual elements, when the current flows from the right leg to the left leg. The red arrows indicate the homogeneous bias field

change the height above the mirror surface without changing the the horizontal position as well. This effect can be mitigated by including a pair of compensation coils along the vertical axis. However the use of extra compensation coils deforms the quadrupole field and can degrade the MOT.

The configuration of the u-shaped wire in combination with a bias field only produces a good quadrupole field close to the zero-field point. Further away from this point the field lines have a significant angle with respect to the quadrupole axis. This degrades the efficiency of the MOST, since it requires the laser beam to be aligned with the magnetic field lines. The deviation of the field is because the field induced by a round wire is circular. To generate a more convenient field which is shaped closer to that of a quadrupole field, the central-wire is flattened (the thickness in the z -direction is reduced) and stretched (the width in the x -direction

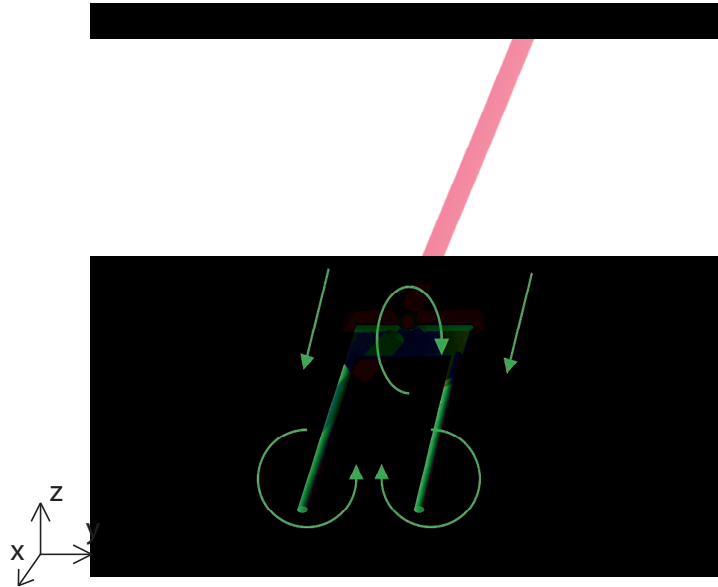


Figure 4.7 Scheme of the surface-MOT with the u-shaped wire underneath the mirror.

is increased)^[62], see Fig. 4.9.

To optimise the shape of the field, I carried out numerical calculations using Mathematica. I approximate the U-shape wire as a bundle of single wires. In order to minimise the errors from this approximation in the trapping volume I choose the distance between the individual wires to be much smaller than the distance between the U-shaped wire and the trap centre.

4.3.5 The Design of the U-Shaped Wire

For the design of the u-shaped wire there are two important points: The field should be close to an ideal quadrupole field over a large distance to have a high capture

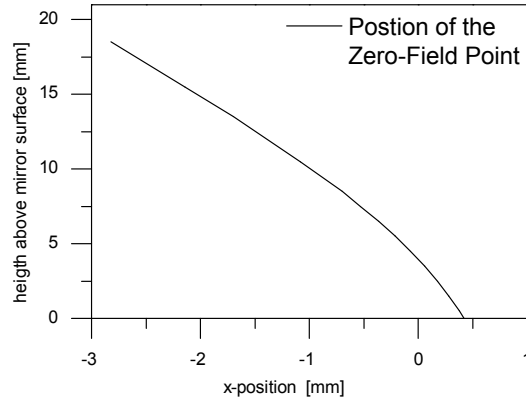


Figure 4.8 Position of the zero-field point, which defines the trap centre, above the mirror as a function of displacement along the x-axis.

range for atoms. Furthermore the u-shaped wire will be in the vacuum chamber hence the wire can not be cooled by convection. Therefore resistance of the wire should be small to avoid heating of the wire.

The Joule heating of any material is:

$$dP = dx \frac{\rho I^2}{A(x)}, \quad (4.14)$$

where ρ is the specific resistance, I is the current and $A(x)$ is the cross-section. A temperature difference across material induces heat-flow:

$$dT = dx' \frac{P}{k_{th} A(x')}, \quad (4.15)$$

where k_{th} is the specific thermal conductivity. This leads to the temperature differ-

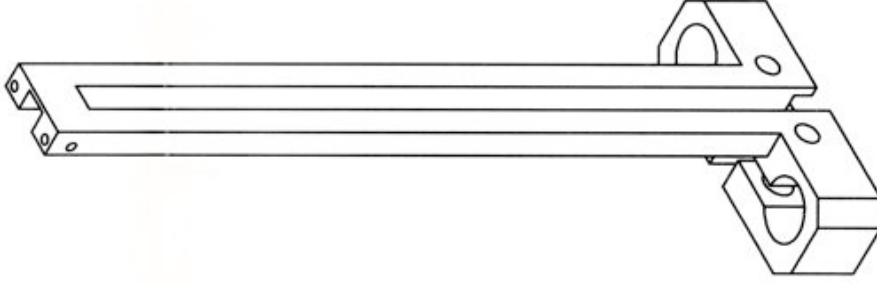


Figure 4.9 A 3d drawing of the u-shaped wire. It consists of a thin plate connecting two rods, which will be fixed on a cooper feed trough of the vacuum chamber.

ence across the entire material:

$$\Delta T = I^2 \int_0^l dx' \frac{1}{A(x') k_{th}} \int_0^{x'} dx \frac{\rho}{A(x)}, \quad (4.16)$$

where l is the total length. The rods of the electric feed through act as heat sinks, since they are connected to the vacuum chamber. Eqn. (4.16) can be simplified because the cross-section of the legs as well as the centre wire are constant. I introduce the following quantities: the electric resistances $R_{cent}^{el} = \rho \frac{l_{cent}}{A_{cent}}$, $R_{leg}^{el} = \rho \frac{l_{leg}}{A_{leg}}$, the Joule heatings $P_{cent} = R_{cent}^{el} I^2$, $P_{leg} = R_{leg}^{el} I^2$ and the thermal resistances $R_{cent}^{th} = \frac{1}{k_{th}} \frac{l_{cent}}{A_{cent}}$ and $R_{leg}^{th} = \frac{1}{k_{th}} \frac{l_{leg}}{A_{leg}}$, to end up with the following expression for the difference in temperature between the centre of the centre wire and the outer ends of the legs:

$$\Delta T = \frac{1}{4} P_{cent} R_{cent}^{th} + \frac{1}{2} (P_{cent} + P_{leg}) R_{leg}^{th} \quad (4.17)$$

To avoid excess heating, I choose the cross section of the legs to be $3 \text{ mm} \times 3 \text{ mm}$

and their length to be 88.5 mm. They are connected by the central plate which has a length of 5 mm, a width of 3 mm, and a thickness of 0.5 mm. On the other end the legs have incorporated clamps to be mounted on the copper feedthrough, whose leads have a diameter of 6.5mm, see Fig 4.9. The thermal conductivity of copper is $k_{th} = 401 \text{ W}^{-1}\text{m}^{-1}$ and the specific resistance is $\rho = 16.78 \cdot 10^{-9} \text{ }\Omega\text{m}$, see appendix B.3. This results in the electric resistances $R_{cent}^{el} = 20.1 \text{ }\mu\Omega$, $R_{leg}^{el} = 165.0 \text{ }\mu\Omega$ and a total electrical resistances $R_{tot}^{el} = 363.6 \text{ }\mu\Omega$. The thermal resistances are $R_{cent}^{th} = 2.8 \frac{\text{K}}{\text{W}}$ and $R_{leg}^{th} = 24.5 \frac{\text{K}}{\text{W}}$.

With a current of 35 A, which is typical for the operation of the MOST, the Joule heating equate to $P_{cent} = 0.025 \text{ W}$, $P_{leg} = 0.202 \text{ W}$. The total power dissipated is $P_{cent} = 0.429 \text{ W}$ which leads to a temperature difference of $\Delta T = 3 \text{ K}$ between the centre of the centre plate and the outer end of the legs. When operating the u-shaped wire continuously with 35 A the temperature stabilises at the end of the feedthrough, outside of the vacuum chamber, at $41 \text{ }^\circ\text{C}$, hence the temperature of tip of the u-shaped wire is $44 \text{ }^\circ\text{C}$. The chamber, which acts as a heat-sink has a temperature of $24 \text{ }^\circ\text{C}$ and the table $16 \text{ }^\circ\text{C}$. Note that other sources, e.g. the pressure gauge and the bias coils, also contribute to the heating of the chamber.

4.3.6 The Magnetic Fields of the U-Shaped-Wire

The simulation shows that the design of the u-shaped wire in combination with a homogeneous bias field is well suited to create the magnetic field required for the MOST. Fig. 4.10 displays the field through the centre of the trap for the xz-plane

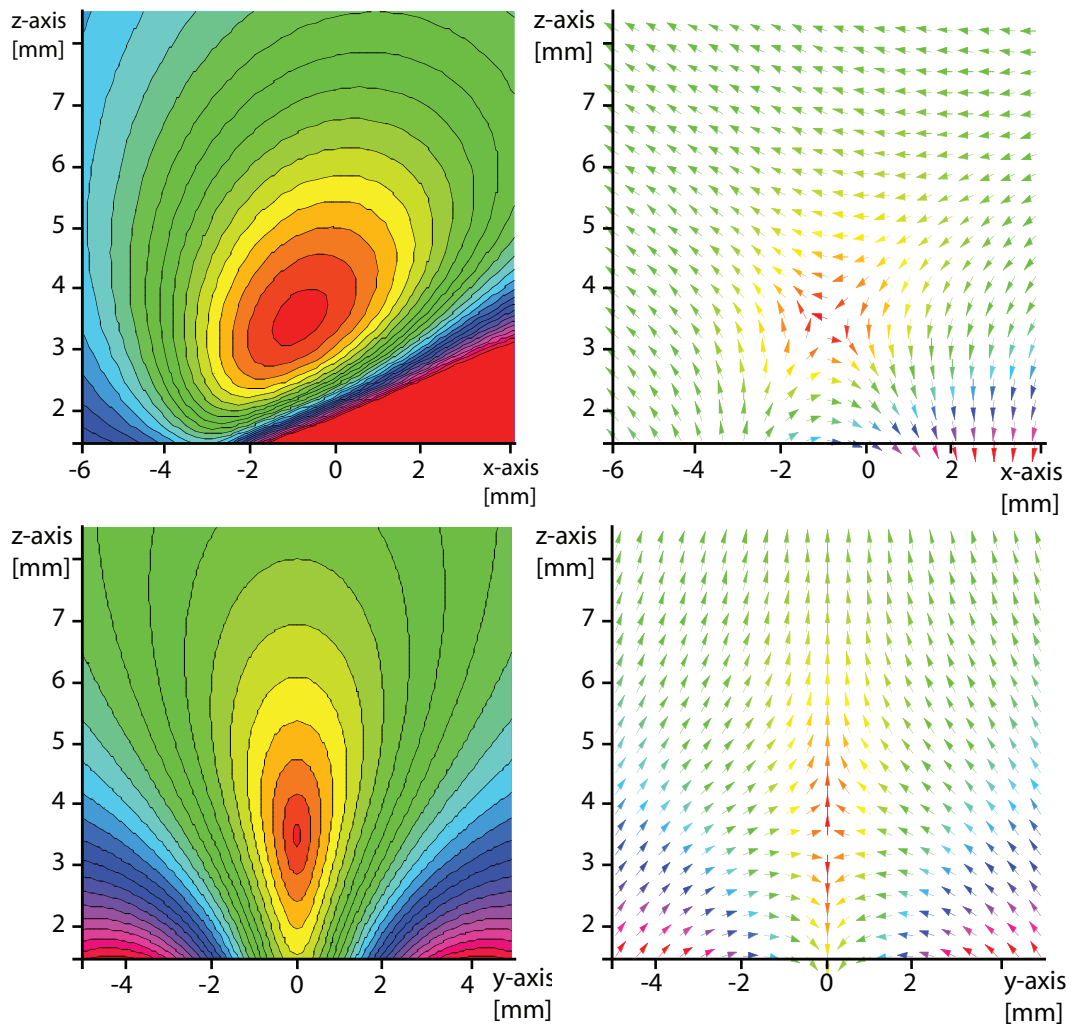


Figure 4.10 These figures show the calculated magnetic field of the u-shaped wire. The top two graphs show the xz -plane and the lower two the yz -plane. The left two graphs display the field strength. The arrows in the right figures indicate the direction of the field. The field is chosen so that the centre of the trap is 3.5 mm above the mirror surface with a current of 20 A and a bias field of 5.64 Gauss at an angle of 20.76° , ($B_x = 5.76\text{ Gauss}$, $B_z = 2\text{ Gauss}$).

and the yz-plane. Two diagonal field axis lay in the xz-plane. The diagonal laser beams, which are reflected of the mirror surfaces, are aligned with those field axis. The field increases in the lower right corner of the graph, due to the proximity to the u-shaped wire. A symmetry axis lies at $y=0$ in the yz-plane, because the plane is situated in the middle of the two legs of the u. The legs are the only source for the magnetic field in this plane. Fig. 4.11 shows the field strength along the axis. Compared with other experiments the dimensions of the u-shaped wire are rather small^[62], but the field is still large enough for atoms to be trapped and cooled. Two EA 3016-20 P Elektro-Automatik power supplies drive the u-shaped wire current of up to 40 A. Two coils separated by 200 mm, each with a diameter of 160 mm and 40 turns, produce the bias field of up to $B_{bias} = 30$ Gauss at a current of 20A, which is delivered by an EA 3016-20 P power supply.

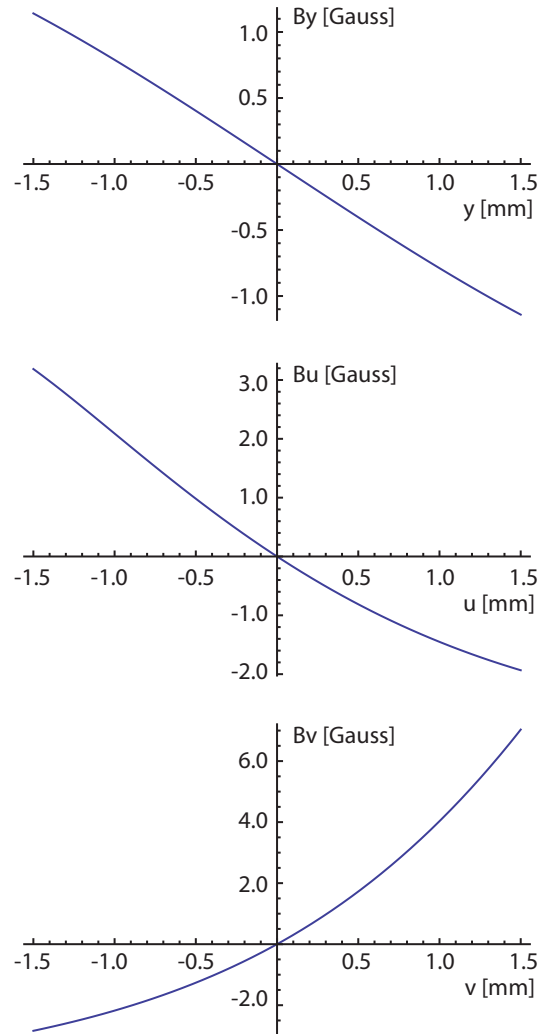


Figure 4.11 These figures show the calculated fields along the axis of the magnetic field of the u-shaped wire. The field is chosen so that the centre of the trap is 3.5 mm above the mirror surface with a current of 20 A and a bias field of 5.64 Gauss at an angle of 20.76° , ($B_x = 5.76$ Gauss, $B_z = 2$ Gauss). The gradients are $Dy = -8.12$ Gauss/cm, $Du = -12.72$ Gauss/cm and $Dv = 20.85$ Gauss/cm, where u and v are defined as $\hat{u} = \frac{1}{\sqrt{2}}(\hat{x} + \hat{z})$ and $\hat{v} = \frac{1}{\sqrt{2}}(-\hat{x} + \hat{z})$, see Fig. 4.5. With Ratios 1:1.5:2.5 this is close to a quadrupole field, which has ratios of 1:1:2.

Chapter 5

Lab Setup of the MOST

The realisation of the MOST requires many individual components and systems. It encompasses the generation and control of the laser beams, the magnetic fields as well as the vacuum technology. The dynamic control is done by a computer.

5.1 Optical Setup

The MOST requires two laser light systems: One to drive the cooling transition and one for the repump transition. Their intensity and frequency need to be controlled quickly and with high precision. For the dipole trap a third high-power laser source is required, which requires less control of power and frequency. The lasers are monitored with Fabry-Perot interferometers and a wavemeter. The light intensity and frequency are controlled with acousto-optic modulators, prior to directing the beams into the vacuum chamber, see Fig 5.1.

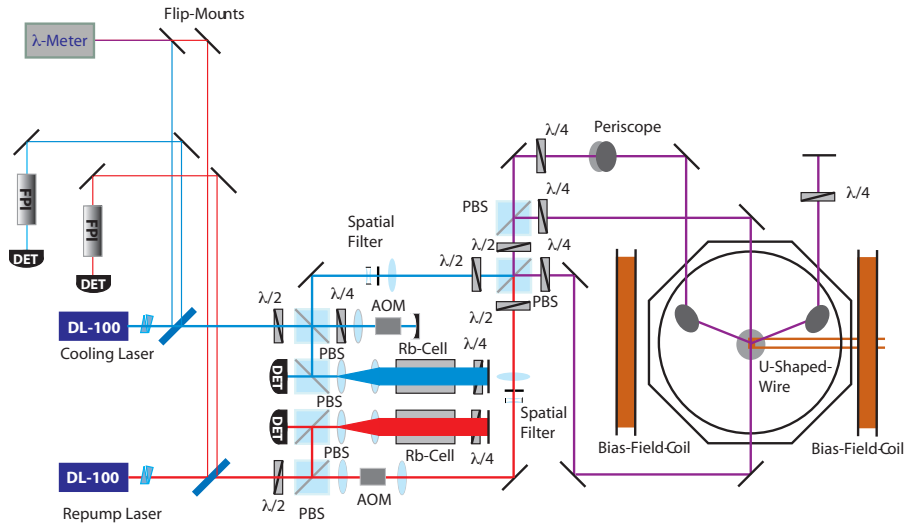


Figure 5.1 Scheme of the laser-setup used for the MOST. On the left-hand side there are the two DL-100 diode-lasers, the Fabry-Perot-interferometers and the wavemeter. In the middle the Doppler-free saturation spectroscopy for the stabilisation is indicated as well as the frequency shift by the AOMs. On the right-hand side the light of the cooling-beam and repumping-beam is combined and split into 3 different beams for the MOST. One pair of beams is travelling in parallel to the mirror whereas the other two beams come from above and have an angle of 45 degrees with respect to its surface. The position of the U-shaped wire and the bias-field coils is also shown.

5.1.1 The Cooling and Repump Laser

Two Toptica DL 100 Laser generate light for cooling and repumping. The laser head contains a laser diode and an optical grating in the Littrow configuration, see Fig. 5.2. The line width in this configuration can be less than 1 MHz according to the manufacturer. Laser diodes emit a beam with a power of up to 150 mW. The spectral mode structure of the laser is determined by several factors: The overall gain profile of the laser diode limits the accessible spectral range of the laser. The centre of the gain profile can be fine tuned by a change of the operating temperature

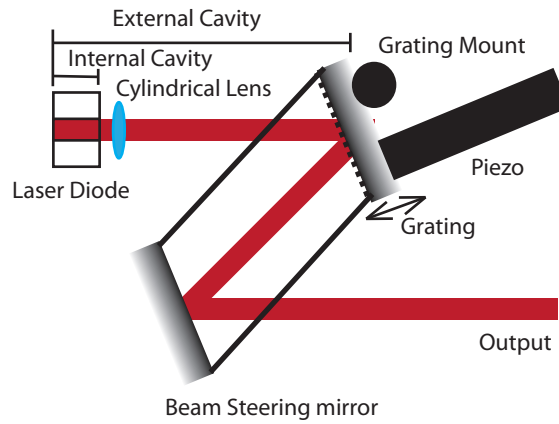


Figure 5.2 Scheme of the laser-head. A laser diode emits radiation onto a optical grating in Littrow configuration, i.e. the minus first order is reflected back into the laser. The zero order is used to couple out light from the cavity via a beam steering mirror. This mirror compensates for changes in beam pointing which arises when tilting the grating.

and laser current. In addition, the grating, see Fig. 5.2, imposes an external mode structure onto the laser. To avoid an influence from the diode cavity the output facet is anti-reflection coated.

The driving current changes the refractive index of the laser diode and hence shifts the mode structure of the resonator. The current can be modulated very fast, to modulate the laser frequency quickly. One way is to connect a fast field-effect-transistor parallel to the laser diode. This configuration can modulate the current with a frequency of up to 20 MHz and is used for the laser stabilisation, see section 5.1.3. Additionally a Bias-T is included into the driving electronics. With the bias-T the current can be modulated up to 200 MHz, to create sidebands for the Pound Drever Hall detection, see appendix C. The control electronics are made by Toptica

and consists of a monitor unit DC 110, a current controller DCC 110, a temperature controller DTC 110, a grating controller SC 110 as well as a Pound Drever Hall detector PDD 110 and a proportional-integral-differential controller PID 110 for the laser locking.

5.1.2 The Laser Source for Dipole-Force Trapping

A tapered amplifier laser system, a Toptica DLX-110, provides the dipole trapping laser beam. Its laser head consists of a tapered amplifier combined with a feedback grating. This configuration leads to a line width of about 1 MHz with a power of up to 800 mW. The spatial profile of the tapered amplifier is rather poor, due to the strip like output facet of the tapered amplifier chip. A set of cylindrical lenses shapes the profile to be closer to a gaussian laser mode. The laser beam then passes through an optical isolator to prevent unwanted feedback of back-reflections. A temperature controller (Toptica DTC 110) and a current controller (Toptica DCC 110) in combination with a monitor unit (Toptica DC 110) operate the laser head.

5.1.3 Laser Locking

Laser cooling requires a stabilisation of the laser frequency to a linewidth of less than one MHz. To achieve this stability the lasers are locked onto atomic transition lines. Rb exhibits a hyperfine structure with a level splitting of hundreds of MHz. These gaps can be bridged by acousto-optic modulators, which shift the frequency of the laser radiation up to several 100 MHz. Hence the laser can be stabilised on

one absorption line and then subsequently be shifted to another line. For the level structure see Fig. 3.4.

The lasers are stabilised using the Pound-Drever-Hall (PDH) method, as described in appendix C. It has a wide looking range and the PDH signal is feed into the Proportional-Integral-Differential controller (PID), which applies a feedback to the laser.

The PID-controller gives an output signal to minimise the error signal, which is the difference between the set level and the input signal, in this case the PDH signal. The output is used as a feedback for the laser system. To minimise the error signal, the controller contains a differential, a proportional and a integral part. The differential part gives a contribution proportional to the derivative of the error signal, hence it is very fast. The proportional part gives a contribution proportional to the error. It is slower than the differential part, but maintains a contribution when the difference stays constant. Last the integral part contributes to the signal by integrating over the error. This part has the slowest response but is the only part that will asymptotically reduce the error to zero.

Feedback to the laser is applied by changing the laser diode current and by changing the length of the external cavity through the grating inclination. The current feedback provides fast feedback but has a limited range. The grating, however, has a slow feedback over a larger range to compensate for long term drifts.

5.1.4 Fabry-Perot Interferometer and Wavemeter

To successfully lock a laser, its wavelength has to be tuned close to the locking transition. This is done with the help of a wave-meter (Metro Lux WL200 with an absolute accuracy of 500 MHz). Furthermore the lasers have to run in single mode for operating the MOST, this is observed with a self-made Fabry-Perot interferometer.

The Fabry-Perot interferometer consists of two mirrors of focal length 10 cm in confocal geometry. One of the mirrors is mounted on a piezo-tube, in order to vary the cavity length. The tube and the other mirror are mounted on a steel tube. With the piezo-driver (Pickelmann SVR 200/3), which provides an output voltage from -50 V to 200 V, the interferometer can be tuned through two free spectral ranges $\nu_{FSR} \approx 1.5$ GHz. The bandwidth of the interferometers is $\nu_{FWHM} = 3.5$ MHz, which corresponds to a finesse of $F \approx 400$.

5.1.5 The Acousto Optical Modulators

Acousto Optical Modulators (AOM) are used to shift the frequency of laser beams and to provide fast switching of intensities. The optically active part of an AOM is a crystal in which acoustic waves run in the radio frequency domain. The acoustic waves diffract the optical radiation, similar to Bragg diffraction. Due to the momentum exchange with phonons in the running wave, the frequency of the laser radiation is shifted by the acoustic frequency or multiples thereof. This technique is most efficient when the $\pm 1^{st}$ diffraction order is used.

The AOMs are driven by a home-built 1.6 W radio frequency source, which are

made of Minicircuits components. Fig. 5.3 shows their scheme. The first component is a **V**oltage **C**ontrolled **O**scillator (POS-150 or POS-100), which can be tuned over a range of 75 MHz to 150 MHz, or 50 MHz to 100 MHz, respectively. To monitor the output frequency a directional coupler PDC-10-1 is connected to the VCO. Amplitude modulation is achieved by using a frequency mixer SRA-1MH in reverse. This configuration works well for moderate and high output power. Though it shows nonlinear behaviour at low control voltages and it does not attenuate the transmitted rf-power completely. Therefore a PSW-1211 rf-switch is included after the AMP-77 pre-amplifier, which is connected to the SRA. The pre-amplifier is required since the power-amplifier has a fixed amplification and requires an input level of 15 dBm to achieve the desired output level.

These components are all surface mounted and placed onto one board into a shielded die cast aluminium box. The output is then put through a low pass filter to remove the higher harmonics from the signal. These come from non linear behaviour in the driver, the frequency mixer and from the distortion of the pre-amplifier. The signal is then fed into a rf-power amplifier, which is home-built and uses a Motorola CA2832 RF amplifier. They deliver an output power of up to 1.6 W. It turns out that the power amplifier can be operated beyond the 1-dB compression point to increase the output power. The amplifiers response becomes nonlinear and hence another low pass filter is required to filter out the higher harmonic frequencies added.

The AOMs operate either in single or double pass configuration. The single pass configuration has the advantage that the efficiency is very high with up to 85 %,

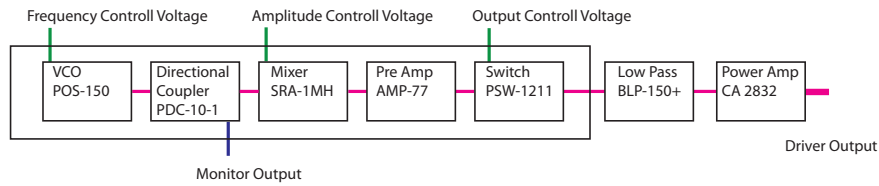


Figure 5.3 This is the scheme of the AOM driver

though it's drawback is that a change in frequency also changes the beam pointing. If the AOM is used in a double pass configuration, the efficiency drops to typically 70% or less, but since the beam is retro-reflected, the overall pointing of the beam does not change since the beam-pointing is altered in opposite directions with each pass through the AOM.

The frequency shifted beam travels back along the same optical path as the incoming beam. One way of separating them is to use a polarising beam splitter. To do so, a quarter wave plate included in the setup changes the axis of polarisation. Since the light crosses it twice, it acts like a half wave plate. It is important to place it next to the retro-reflecting mirror, as otherwise the birefringent AOM will also act on the polarisation.

After the AOMs the laser beams are spatially filtered to improve the beam profile. The beam is focussed by a microscope objective (focal length 28.91 mm) onto a pinhole (diameter 33 μm). The expanded beam is collimated by a plano-convex lens (Focal length 75 mm). The spatial filtering amounts to a loss of 20% in power in the laser beams.

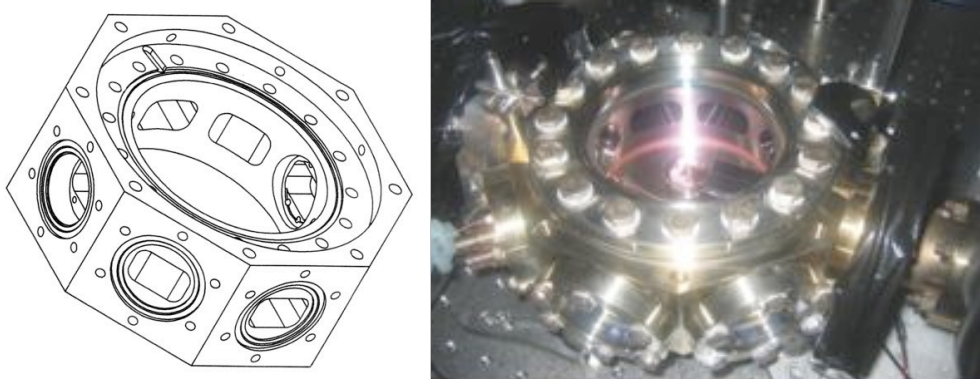


Figure 5.4 (left) A 3-d drawing of the science chamber. (right) The chamber with the u-shaped wire and the finger in place. The top viewport is DN-100 size and the side ones are DN-40.

5.2 The Vacuum Chamber

The chamber is octagonal with two large opposing viewports and eight small ones to provide excellent optical access, see Fig. 5.4. Attached to the science chamber is the auxiliary arm, which contains the ion getter pump, the titan sublimator and the Bayard-Alpert pressure gauge. The science chamber has electric feed throughs for the rubidium dispenser and the u-shaped wire for the magneto optical trap.

5.2.1 The MOST Finger

The MOST is located in the centre of the science chamber. It requires a mirror surface as well as u-shaped wire underneath. To support this configuration a steel finger reaches into the centre of the science chamber, see Fig. 5.5. A ceramic mount is glued, with vacuum compatible glue, Epotek 353ND/2, on the tip of the finger. It supports the u-shaped wire, and a 0.5 mm thick mirror. The surface of the mirror

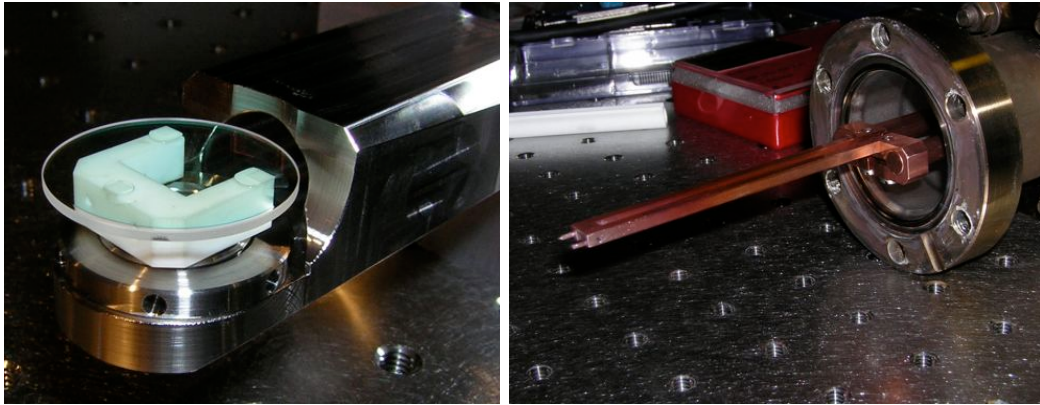


Figure 5.5 The finger for the MOST. The u-shaped wire will be pushed into the finger from the right and rest inside the ceramic holder underneath the mirror.

is 1 mm away from the surface of the u-shaped wire.

5.2.2 The Beam Steering into the Vacuum Chamber

To combine the repumping and cooling beam and to split the light into the needed MOT beams, a combination of $\lambda/2$ plates and polarising beamsplitters is used. Finally $\lambda/4$ plates produce the necessary circular polarisation of the light. For both the horizontal and diagonal beam-pair, two independent beams are used. The diagonal beams enter the vacuum chamber from above, see Fig. 5.6. The beam diameter is $w = 3$ mm and the power of the cooling beam is $P_{cool} = 8$ mW and the power of the repumper is $P_{repump} = 0.3$ mW. So the intensity of the cooling beam is $I_{cool} \approx 35.5 I_{sat}$.

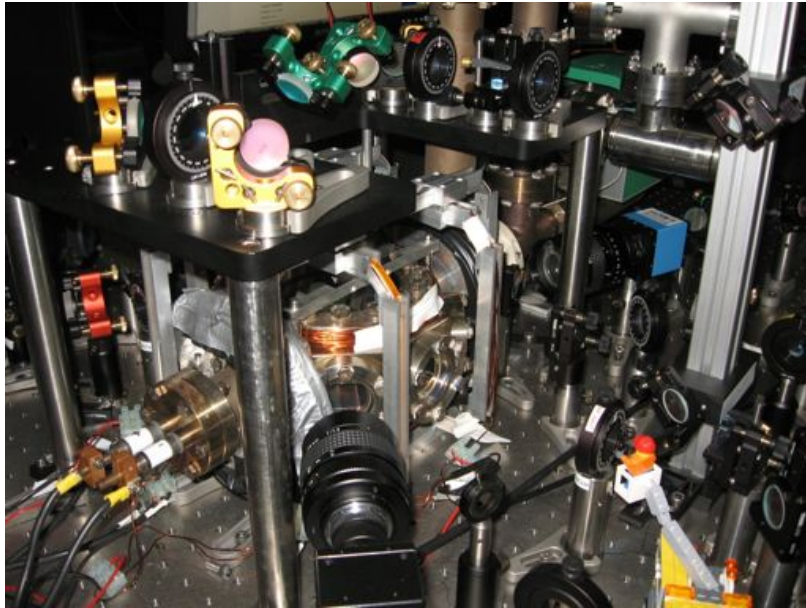


Figure 5.6 The vacuum chamber, with the mirrors (green and gold) for the diagonal MOST beams mounted on the table above the vacuum chamber.

5.3 The Computer Control

The MOST depends on many parameters that need to be controlled dynamically for experiments like time of flight measurement and the loading of the dipole-force trap. The time scale required for the control is determined by the speed of the atoms, which at the doppler cooling limit is about $170 \mu\text{m}/\text{ms}$. Since the dimension of the trap is on the order of $100 \mu\text{m}$, a sub-millisecond time scale is required.

All the measurements on the trapped atoms carried out in this theses rely on imaging either the atomic fluorescence or absorption, which are observed with CCD-cameras. A real-time analysis of these images is required for the efficient optimisation of the trapping procedures. A self written programme running on a standard Win-

dows computer containing two Adlink DAQ-2502 IO-boards manages these tasks, see appendix D.

Chapter 6

Characterisation of the MOST

This chapter includes the observation and characterisation of the MOST as well as the loading of a dipole trap from this trap. The trapped atoms were observed using both fluorescence and absorption imaging.

6.1 Observation of the MOST

A monochromatic CCD-camera, The Imaging Source DMK 21BF04, observes the MOST. It has a resolution of 640×480 and an objective with a focal length of 75 mm. The field of view is about 10 mm. The camera observes the fluorescence light, which is induced by the MOST cooling beams illuminating the atoms. The fluorescence images are shown in Fig. 6.1 for various magnetic field settings.

The first MOST is observed at a distance of 1 mm above the surface of the mirror, see Fig.6.1. By varying the magnetic fields, the position of the MOST above the surface can be changed from 1 mm to about 0.2 mm, see figure 6.2. When the

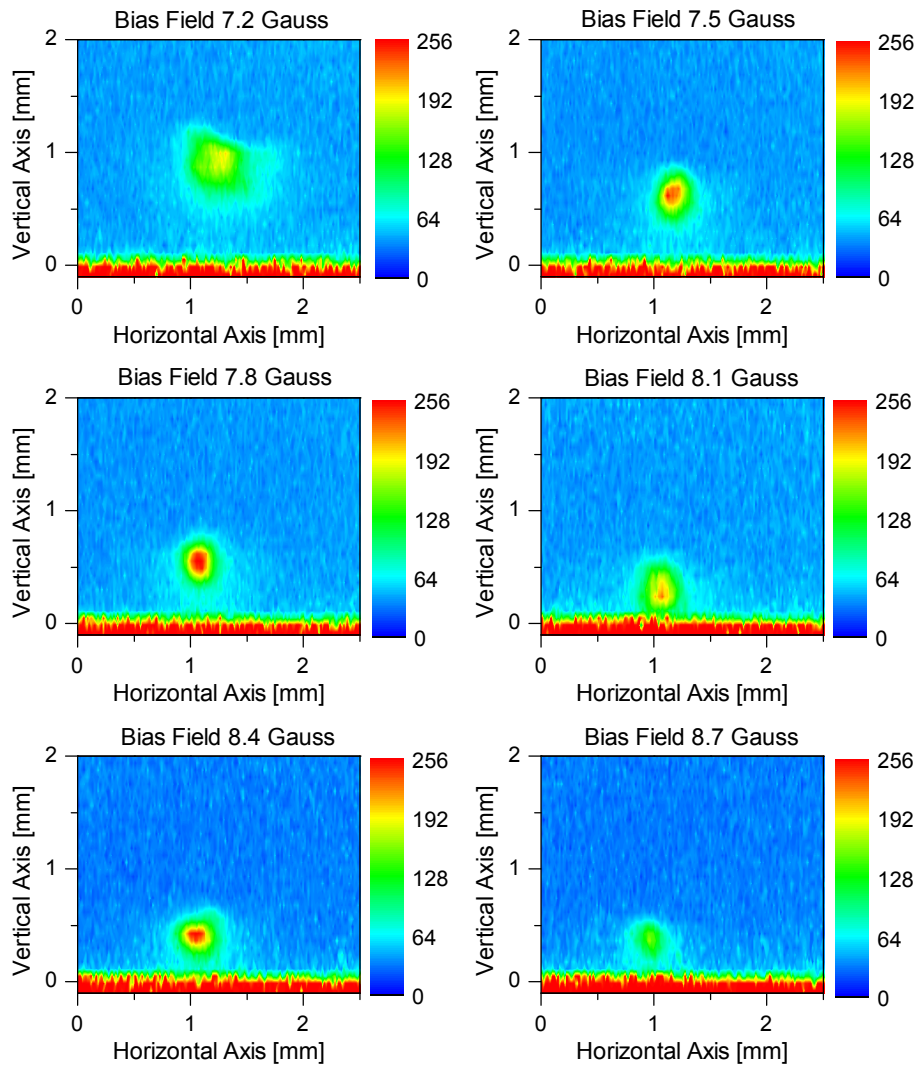


Figure 6.1 These pictures are fluorescence images of the MOST taken for various magnetic-bias-Fields (7.2; 7.5; 7.8; 8.1; 8.4 and 8.7 Gauss). The bright feature in the bottom of the picture is the mirror, which scatters off the cooling laser beams, which are illuminating the atoms. The pictures show the MOST moving closer to the mirror as the bias-field increases. At the same time the MOST becomes weaker.

centre of the MOT is moved too far from the surface, the size of the atom cloud increases, but at the same time the density decreases. On the other hand, when

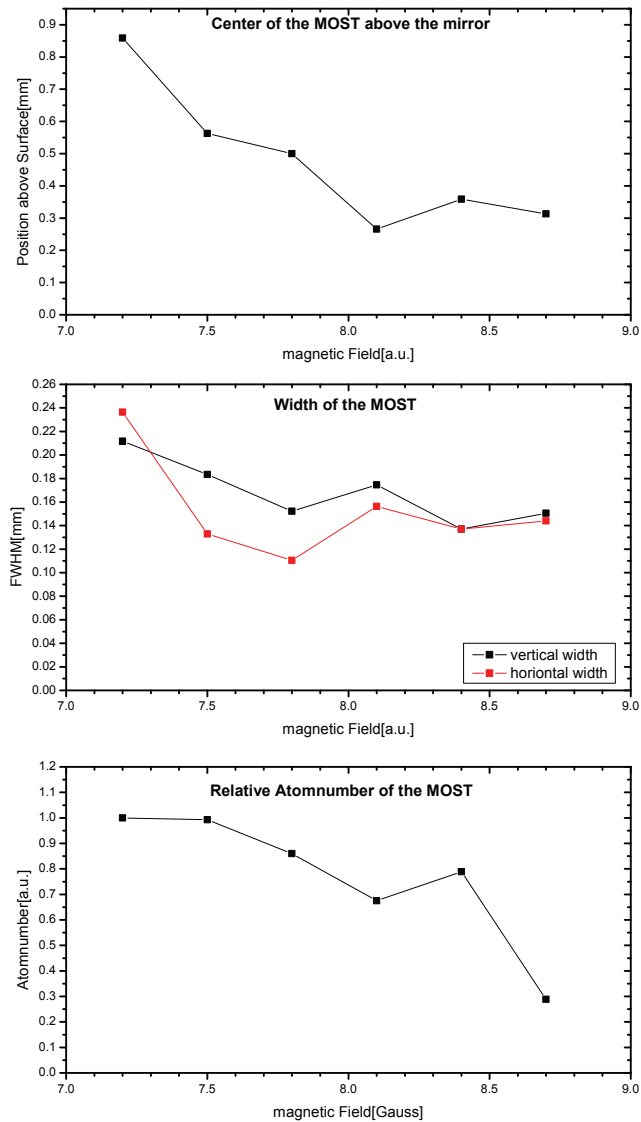


Figure 6.2 The top graph shows the distance of the MOST to the mirror surface, the middle one shows the vertical and horizontal width of the MOST and the lower one the relative atom number of the MOST for different bias-fields. It can be seen that the distance of the MOST and the mirror decreases when the bias-field is increasing. At the same time the MOST is compressed and the number of atoms decreases. The MOST furthest away from the surface contains about 20.000 atoms.

the centre is moved closer to the mirror surface, the field gradient is higher and the cloud is compressed. When it comes close to the mirror surface the number of captured atoms decreases dramatically. This can be understood since the border of the atomic cloud touches the mirror and therefore the loosely bound atoms are lost and hence the loss-rate is greatly increased. It turns out the limit for creating a MOST is about 0.2 mm from the surface.

The atom number of the trapped atoms was determined by fluorescence detection. Due to the experimental setup the scattered from within the vacuum chamber was much higher than the fluorescence of the atoms, hence the standard method of measuring the fluorescence with a photodetector does not work. Instead I used the camera to collect the fluorescence. I calibrated the camera by shining in a laser beam with a power comparable to the fluorescence signal. By taking into account the geometrical collection efficiency I determined the number of trapped atoms to be $n \approx 20.000$.

The density limit for a MOT is $\sim 10^{11}/\text{cm}^3$ ^[54]. Taking the diameter of the cold clouds to be $d = 0.02$ cm, this leads to a volume $V = 4.2 \cdot 10^{-6} \text{ cm}^3$, hence the atom number expected for the density limit is $n_{limit} \approx 420.000$, which is about one order of magnitude higher than the measured number. Though the fluorescence measurement intrinsically underestimates the atom number, since the multiple scattering events within a dense cloud, reduce the amount of fluorescence light. Also the Rubidium background pressure was relatively low $\sim 10^{-9}$, a higher pressure would certainly increased the number of trapped atoms.

6.2 Loading of the Dipole Trap

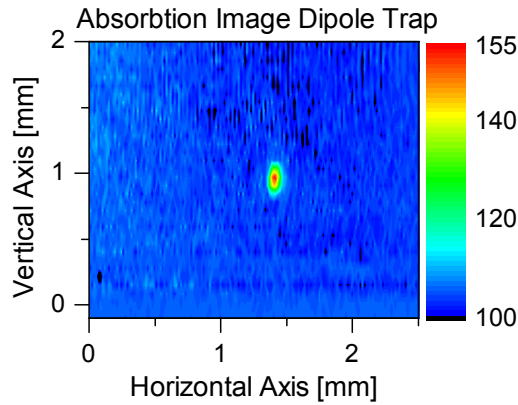


Figure 6.3 This picture shows the absorption image of atoms in a dipole trap 15 ms after they have been loaded from the MOST.

As a first step towards the optical tweezers I investigated the loading of atoms into an optical dipole trap. To generate the trap a 300 mm lens focusses a laser-beam $\lambda = 784 \text{ nm}$ of a DLX 110 down to $w = 50 \mu\text{m}$. This is done without the spatial light modulator, so it is only a static focussed beam. With the power of 250 mW in the beam this results in a trap depth of $170.1 \mu\text{K}$ for a running-wave trap. The Rayleigh length for this beam waist $w = 50 \mu\text{m}$ is $z_R = 10 \text{ mm}$, hence the incoming and reflected beam overlap almost perfectly and the resulting trap resembles a standing wave trap with a depth of $680.4 \mu\text{K}$ in the antinodes.

After the atoms are loaded into the dipole trap they are observed by absorption imaging, see Fig. 6.3. The absorption imaging measures the amount of absorption of a light beam when it passes through a cloud of atoms, see Fig. 6.4 The intensity

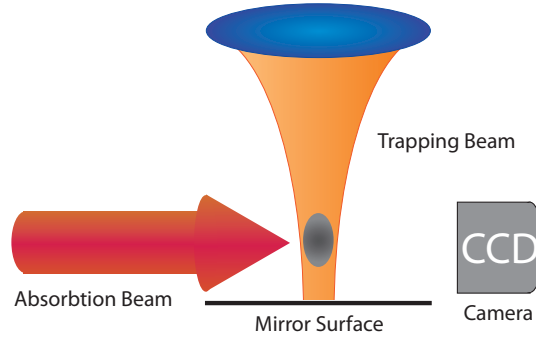


Figure 6.4 This picture shows the absorption image of atoms in a dipole trap 15 ms after they have been loaded from the MOST.

$I(\mathbf{r})$ of the laser beam as^[63]:

$$dI(\mathbf{r}) = -I(\mathbf{r})\sigma_{abs}(\delta, I)n(\mathbf{r})dx \quad \text{with} \quad \sigma_{abs}(\delta, I) = \frac{\sigma_0}{1 + I/I_{sat} + 4\Delta^2/\Gamma^2}, \quad (6.1)$$

where $\sigma_0 = \lambda^2/(2\pi)$ is the resonant absorption cross section. For weak intensities $I/I_{sat} \ll 1$, there Intensity dependents in $\sigma_{abs}(\delta, I)$ can be neglected and equation (6.1) can be formal integrated to: $I_{abs} = I_0 \exp(-D)$, where $D = \int_{-\infty}^{+\infty} \sigma_{abs}(\Delta)n(\mathbf{r})dx$ is the optical density. For optically thin samples $D \ll 1$, the ratio of $I_{abs}/I_0 = 1 - D$ or equivalently $I_0 - I_{abs} = I_0 D$, hence the absorption is proportional to the atom number.

For the imaging a total of three intensity profiles have been taken. The first one was the laser beam with the absorption of atoms. Directly after that an intensity profile without atoms was taken and than finally a picture without the illuminating beam, to determine the background. The illumination beam was tuned on atomic resonance $F=2 \leftrightarrow F'=3$, it had a width of $w = 5$ mm, a power of $100 \mu\text{W}$ an a

duration of $10 \mu\text{s}$. The resulting peak intensity was $I_0 = 0.25 \text{ mW/cm}^2$, which is a factor of six below the saturation intensity.

To determine the lifetime and the loading efficiency, absorption imaging has been taken at various delays after the the start of the loading process, see Fig. 6.5. During the loading there is a significant loss of atoms, the loading efficiency is 12.4%. After the loading process is finished there was an exponential decay in the atom number. The lifetime was fitted to be 327.7 ms. This is promising for the application of the optical tweezers, since the update time of the digital mirror device is $270 \mu\text{s}$ and hence the trapping pattern could be changed several times within the lifetime of the trapped atoms.

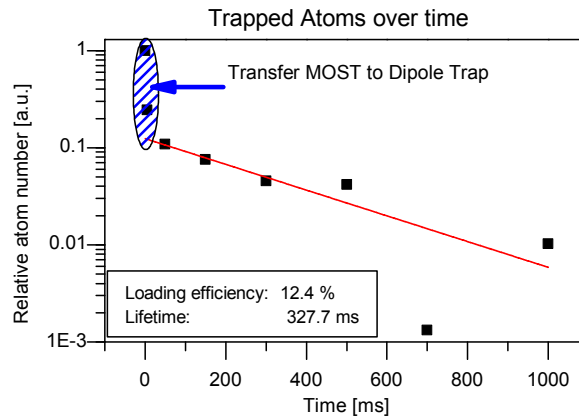


Figure 6.5 The graph shows the atom number in the dipole trap, after it has been loaded from the MOST.

The temperature of the atoms can be determined with the time of flight method. After the trap is switched of the atom cloud expands with a velocity distribution (3.7), where T is the temperature of the atomic cloud after they are released from the trap. Hence the atom cloud width spreads like $w(t) = tw_v$, where $w_v = 2\sqrt{\frac{k_b T}{m}}$. The

velocity spread has to be convoluted with the initial distribution to obtain the total width. If the atomic cloud can be approximated with a gaussian distribution, with a width w_0 , $w(t) = \sqrt{(w_0)^2 + (w_v t)^2}$ gives the total width. The temperature results are obtained for the atoms released from the MOST are $T_{MOST} = 384 \mu K$ and for the atoms of the dipole trap $T_{Dip} = 137 \mu K$. The lower temperature of the dipole trap compared with the MOST, suggests that the trap depth of the dipole trap is lower than the calculated value, hence only cold atoms are loaded into the dipole trap. This is consistent with the low loading efficiency of 12.4%. The measured temperature is about a factor of 5 smaller than the theoretically predicted trap depth. Likely contributions of this discrepancy are: 1. The MOST is not overlapped with the centre of the dipole trap and hence the trap depth experienced by the atoms is not the deepest part of the trap. 2. The trap depth has been calculated using the formula for a Gaussian beam, since the beam significantly deviates from this shape the beam waist will be larger and hence the trap less deep. 3. The temperature of the atoms is always smaller than the trap depth since the temperature is an ensemble average of different energies, this has been verified in an experiment^[64] similar to the one presented here to be a ratio of 0.4. These factors can explain the low temperature compared with the expected trap depth.

Chapter 7

Optical Tweezers

I propose a versatile arrangement for the trapping and manipulation of single atoms in optical tweezers by using spatial light modulators (SLM). It incorporates a high numerical aperture microscope to map the intensity distribution of a SLM onto a cloud of cold atoms. The regions of high intensity act as optical dipole force traps. With a SLM fast enough to modify the trapping potential in real time, this technique is well suited for the controlled addressing and manipulation of arbitrarily selected atoms.

The discussion of the optical tweezers is split up in a number of chapters. This chapter will investigate the fundamental concept of the tweezers and will explain how these tweezers can be realised. The next chapter, chapter 8, investigates in detail the intrigues of imaging extended objects with coherent light. This is crucial since the lack of isoplanatism will lead to highly distorted optical tweezers. In chapter 9, the experimental set-up to realise the optical tweezers is described in detail. Finally

the experimental results are given in chapter 10.

This chapter contains the proposal published in Applied Physics B in 2010^[65]: "Spatial Light Modulators for the Manipulation of Individual Atoms", by L. Brandt, C. Muldoon, T. Thiele, J. Dong, E. Brainis & A. Kuhn, Volume 102, Page 443.

7.1 Outline

At the heart of this novel setup is the use of an SLM to generate arbitrary patterns of light in the object plane of a microscope and to trap atoms therein. Fig. 7.1 illustrates this approach and shows how one can use the same microscope to observe the atoms. Several types of SLM are available which all have the potential to achieve this goal. One widely used technology is the liquid crystal device (LCD)^[33,66]. It has the advantage of creating a range of grey scales, but has the drawback of having a low refresh rate, usually not exceeding 100 Hz. This is in general too slow for the dynamic control of trapped neutral atoms. Other commercially available SLMs are digital mirror devices (DMD)^[67]. They consist of an array of individual flat mirrors which can be independently switched between two tilt angles to generate arbitrary intensity distributions. With a full-frame refresh rate of up to 50 kHz and a resolution of typically 1024 by 768 individual mirrors, these devices seem ideal for the real-time manipulation of trapped atoms.

The desired intensity distribution can be formed in two ways. One possibility is to place the SLM in the back focal plane of a lens system, such that its Fourier transform is in the front focal plane. Thus the SLM acts as an effective hologram

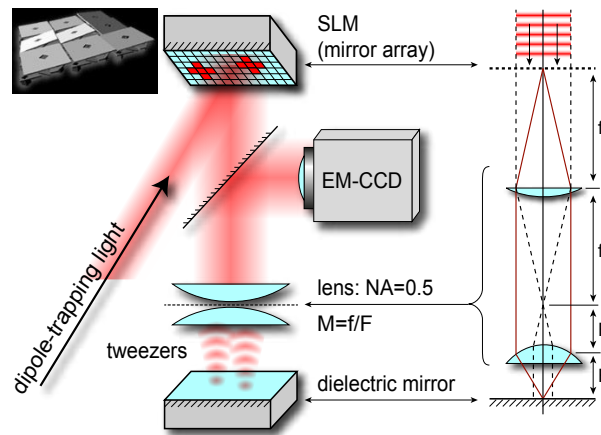


Figure 7.1 Scheme of the proposed setup. A red detuned laser beam illuminates the mirror array of the SLM. A microscope reproduces the intensity pattern of the SLM near the surface of a mirror placed in the tweezer plane (object plane of the microscope). The reflected light interferes with the incoming beam and forms a standing wave. Its antinodes act as dipole traps, which can hold individual atoms. Since the SLM is reconfigurable, the setup allows arbitrary repositioning of atoms. A very sensitive camera, detecting atomic fluorescence via a dichroic mirror, can be used to observe the trapped atoms and monitor the tweezers in operation. The insert (Courtesy of Texas Instruments) shows a block of 3 by 3 mirrors of the SLM. The mirrors can be switched between two tilt angles, so that the light is directed either into the microscope or deflected to a beam stop. On the right hand side, a possible arrangement of microscope lenses is shown, with SLM and tweezers in conjugate planes for point-to-point imaging from SLM to tweezers (solid rays) and isoplanatic reproduction of the collimated wave illuminating the SLM in the microscope's object plane^[68] (dashed rays).

for the resulting intensity distribution^[33]. This method has the drawback that any change in the trapping pattern requires one to recalculate the entire hologram and thus restrains the experimenter to work with predefined sequences. Alternatively, the tweezers can be generated by imaging the surface of an *amplitude-modulating* SLM through a microscope directly onto the atoms. The tweezers are then formed in the object plane of the microscope, see Fig. 7.2. In the following I concentrate

on this latter method, as the direct mapping of intensities provides an intrinsically higher speed and flexibility in the manipulation of trapped atoms. This system can be used to expose the atoms to almost any arbitrarily shaped and time-varying potential landscape, which offers a plethora of applications. Out of these I focus on the implementation of an array of very tiny atom traps, eventually capable of storing single atoms.

The plane of the SLM and the plane where the tweezers are formed are conjugated. Therefore the illumination of the SLM needs to be taken into account. In order to get a uniform trap depth for a given pattern, like in Fig. 7.2, the SLM has to be illuminated uniformly, otherwise the trap depth will vary. Ideally a flat top profile should be used for the illumination. A Gaussian beam could be used as well, provided the beam waist is large enough so that the variation across the SLM stays within bearable limits. If coherent light is used for trapping, a suitable geometry of the illumination has to be chosen to ensure isoplanatism^[68] and therefore no distortion of the waveform.

Any tight spatial confinement of atoms in dipole-force traps relies on small foci of the trapping light. Therefore, an optical system of high numerical aperture is necessary. This can be done with either a sophisticated microscope objective^[69] or a single aspheric lens^[70]. Typically, these are diffraction limited and have a numerical aperture of 0.5, leading to an optical resolution approximately equal to one wavelength, λ . This also determines the lateral confinement of the atoms. Along the optical axis, the atoms are trapped by the longitudinal beam profile. For a single

beam focussed to λ , atoms are axially confined to a Rayleigh length of $\pi \cdot \lambda$. To obtain a better confinement along the optical axis, a standing wave could be used. This can be achieved by placing a mirror at or close to the plane where the tweezers are formed. The atoms trapped in the anti-nodes of the standing wave are then axially confined to $\lambda/2$.

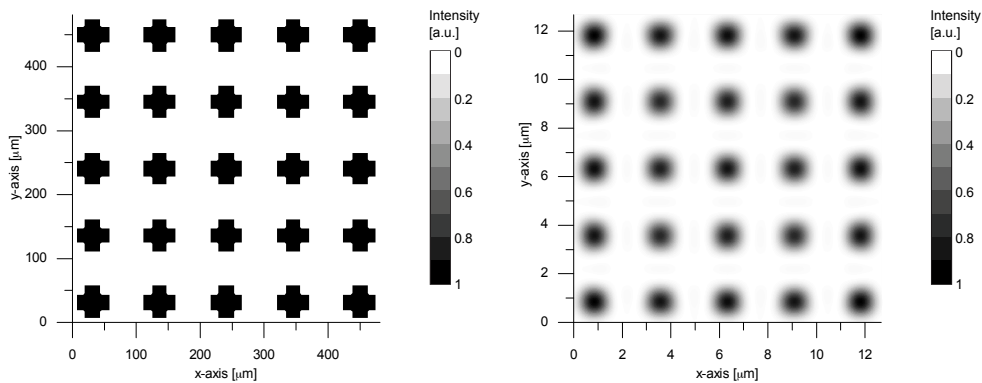


Figure 7.2 The top picture shows a pattern on the SLM. The pattern is a repetition of a 4 by 4 mirror block where the corner pixels are missing. Each mirror has a dimension of $14 \mu\text{m}$ by $14 \mu\text{m}$. The bottom picture shows the resulting image, when a diffraction limited lens system with a numerical aperture of $NA = 0.5$ is used to demagnify the pattern by a factor of $1/38$. This picture is obtained by convoluting the demagnified pattern from above with an airy pattern of $1 \mu\text{m}$ waist.

7.2 Feasibility

7.2.1 Dipole trapping of Alkali Atoms

The optical tweezers consist of tiny optical dipole-force traps, in which the dynamic Stark shift gives rise to a trapping potential in the *far* detuned limit^[52]:

$$U_{dip}(\mathbf{r}) \approx \frac{\hbar\Gamma^2 I(\mathbf{r})}{8\delta I_{sat}} \quad (7.1)$$

where δ is the detuning of the trapping laser light with respect to the atomic transition, $I(\mathbf{r})$ is the intensity of the trapping light, I_{sat} is the saturation intensity for the chosen transition, and Γ is the corresponding decay rate. For red detuned light, $\delta < 0$, U_{dip} is negative and hence attractive. The most critical parameter is the trap depth U_0 , which corresponds to the highest intensity of the trapping laser light I_0 . Hence U_0 is the energy required for an atom at rest to escape the trap, neglecting gravity. Obviously, the trap depth has to be at least as large as the energy of the pre-cooled atoms. Therefore, the minimum usable trap depth is determined by the temperature that can be reached by the magneto-optical trap. For rubidium, the Doppler cooling limit would be $T_D = 143 \mu\text{K}$. However, it is desirable to operate deeper traps since the spatial confinement of the atoms increases with depth. For atoms whose kinetic energy is smaller than the potential depth by a sufficient amount, the trap can be treated as harmonic, and the spatial confinement of the atoms can be determined by the harmonic oscillation frequencies ω_r and ω_z for radial and longitudinal motion, respectively. The achievable values of U_0 , ω_r , and ω_z depend on the wavelength λ of the trapping laser, its intensity, and the trap geometry.

In the proposed scheme (Fig. 7.1), the trap geometry is essentially determined by the distance L between the focal plane of the optical system which generates the tweezers and the dielectric mirror. The intensity modulation induced by the

interference of forward and backward travelling waves over this distance can be seen in Fig. 7.3. In the following, I first discuss the limiting case $L \rightarrow \infty$ (left picture of Fig. 7.3), which corresponds to having no mirror at all, and then analyze the longitudinal intensity modulation for finite L .

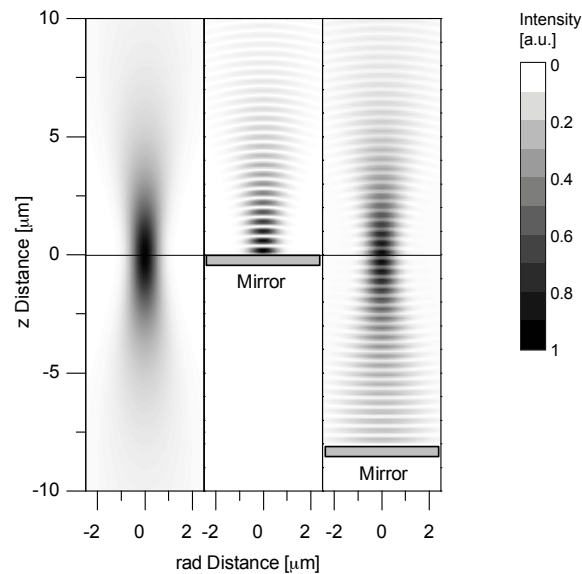


Figure 7.3 Intensity distribution of a focused laser beam (with beam waist $w_0 = 0.78 \mu\text{m}$) in the neighborhood of the focal plane for different distances L between the dielectric mirror and the focal plane. (Black corresponds to the highest intensities.) The left picture is for $L \rightarrow \infty$, i.e. no mirror being present. The tweezer is a pure forward traveling wave with no longitudinal intensity modulation. The middle picture shows a beam which is reflected in its focal plane ($L = 0$). The tweezer has a perfect standing wave pattern, but atoms cannot be trapped in the beam waist. The right picture shows the intensity of a retro-reflected beam whose focus lies $L = 8 \mu\text{m}$ above the mirror surface. Here the intensity modulation is notably less than in the previous case.

When the dielectric mirror is not present ($L \rightarrow \infty$), the trapping potential has a single minimum at the beam waist, in the focal plane of the lens system. The

maximum achievable intensity at that point is

$$I_0 = I_d \cdot M^2, \quad (7.2)$$

where M is the magnification of the microscope (resulting in a demagnification of the DMD by $1/M$) and $I_d = 10 \text{ W/cm}^2$ is the damage threshold of the DMD. To maximise the spatial control of the atoms, the individual traps should be as small as possible. The smallest achievable trap size is set by the resolution of the optical system D_{min} . According to the Raylight criteria it is:

$$D_{min} = 1.22 \cdot \lambda N, \quad (7.3)$$

where λ is the wavelength of the light used, and N is the f-number related to the numerical aperture NA of the optical system by $N \approx \frac{1}{2NA}$. If an aspherical singlet lens is used, the NA can be as high as 0.5. For this value, a resolution limit of $D_{min} \approx 1 \mu\text{m}$ is realisable for $\lambda = 785 \text{ nm}$, which well suited for trapping Rb.

7.2.2 The Role of the SLM

It is important to bear in mind that any experiments involving dynamics require the reconfiguration of the trapping potential. One way atomic transport could be realized is by displacing a pattern of traps. The switching of mirrors would lead to abrupt changes in the trapping potential if the contribution of light for a point in the image plane of the DMD is dominated by one mirror only. If, however, the optical

system does not resolve individual mirrors, the reconfiguration of the traps can be smoother, since the light intensity for every point will have contributions from a number of mirrors. Effectively, this leads to grey scales in the trapping pattern. To take advantage of this, I choose the magnification M such that the diagonal of a 2×2 mirror block is not resolved. As the micro-mirrors of a commercially available DMD have a size of $14 \mu\text{m} \times 14 \mu\text{m}$, a demagnification of $1/38$ is required, i.e. the microscopic magnification should be $M = 38$ (see Fig. 7.2). According to Eq. (7.2), if the DMD is illuminated with light of an intensity at its damage threshold, an intensity I_0 of 14.4 kW/cm^2 can be obtained at the center of a tweezer. To insure a high loading efficiency from the MOT into the tweezers linear polarised trapping light has to be used^[64], for which the saturation intensity for the D_2 line of Rubidium is $I_{sat} = 2.5 \text{ mW/cm}^2$. Therefore the maximum intensity is $5.8 \cdot 10^6$ times the saturation intensity. Taking the above discussion into account and requiring a trap depth of 1 mK leads to a detuning $\delta \leq 2.1 \cdot 10^5 \Gamma$, according to Eq. (7.1). This corresponds to a wavelength detuning of about 2.6 nm to the red with respect to the D_2 line. However, since Rubidium has a fine structure splitting of 15 nm, this estimation of the required detuning is certainly too crude. The hyperfine transitions within the D_1 and D_2 lines of Rb need to be taken into account. Two possible wavelength regimes present themselves. The first is slightly red detuned from the D_2 line at 780 nm, and the second is red detuned from the D_1 line at 795 nm (see the left graph of Fig. 7.4). More specifically, for a trapping laser with an intensity of $I_0 = 14.4 \text{ kW/cm}^2$, for instance, a trap depth of 1 mK can be achieved for the

wavelengths of $\lambda_2 = 782.85$ nm, and $\lambda_1 = 796.90$ nm.

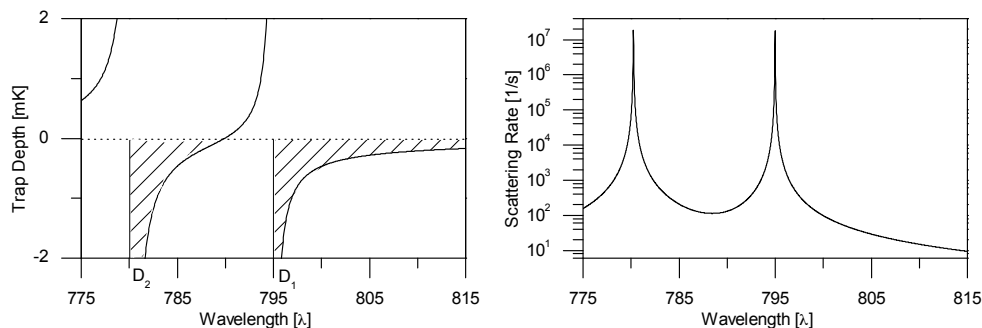


Figure 7.4 The left graph shows the potential depth of the trap with respect to the wavelength of the trapping light, for linearly polarized light with an intensity of $I_0 = 14.4 \text{ kW/cm}^2$. The trapping regions are hatched. The right graph shows the corresponding scattering rate.

Working with light so close to the D₁ and D₂ resonances gives rise to atomic heating due to photon scattering from the trapping beam. The heating is proportional to the scattering rate R_{scat} , which, in the far detuned limit^[52], is given by:

$$R_{scat} \approx \frac{\Gamma^3}{8\delta^2} \frac{I}{I_{sat}}. \quad (7.4)$$

Here I have to take the scattering from both the D₁ and the D₂ line into account, as shown in the bottom graph of Fig. 7.4. For both λ_1 and λ_2 , Rb scatters about 600 photons per second. The scattering rate in both detunings is about the same, since in both cases, the detuning to the closest transition is small when compared to detuning from the other transition. If the trapping laser were further detuned, the region to the red from the D₁ line would be preferable, as the potentials of both lines add constructively there, whereas in the region in-between the D₁ and D₂ lines,

the potentials add destructively.

Given that each scattering event involves an exchange of two photons, the kinetic energy of an atom increases on average by twice the recoil energy per scattering event. The lifetime τ of a Rubidium atom (initially at rest) in the dipole trap would therefore be limited to $\tau = 1/R_{scat} \cdot U/2E_{rec}$. This yields $\tau = 2.3$ s if photon scattering is the only source of heating. It will be shown below that this time is long enough to allow for many transport and detection cycles.

7.2.3 Radial and Axial Confinement

We now estimate the radial and longitudinal confinement for a travelling-wave dipole trap ($L \rightarrow \infty$). Since a 2 by 2 mirror block is spatially not resolved in the object plane of the microscope, I may safely assume that the corresponding intensity distribution is basically limited by diffraction and therefore cylindrically symmetric. The intensity of the light field in the radial direction then reads

$$I(q) = I_0 \left(\frac{2 J_1(q)}{q} \right)^2, \quad (7.5)$$

where $q = \frac{\pi r}{\lambda N}$, r is the distance from the axis of the trap, and $N \approx 1/(2 NA)$ is the f-number which is about 1 in this case. $J_1(q)$ is a Bessel function of the first kind.

For small q , it expands as

$$J_1(q) = \frac{1}{2}q - \frac{1}{16}q^3 + O(q^5). \quad (7.6)$$

Inserting this into (7.5) and keeping only terms up to second order I obtain the harmonic approximation to the trapping potential in the radial direction:

$$U(r) \approx U_0 - \frac{U_0}{4} \left(\frac{\pi}{\lambda N} \right)^2 r^2. \quad (7.7)$$

Here U_0 is the trap depth, which is plotted in Fig. 7.4 as a function of the wavelength λ . A particle with mass m oscillates with frequency

$$\omega_r = \sqrt{\frac{-U_0 \pi^2}{2m \lambda^2 N^2}} \quad (7.8)$$

in this potential. For $-U_0 = 1 \text{ mK} \cdot k_B$, this leads to a radial trapping frequency of $\omega_r = 2\pi \cdot 162 \text{ kHz}$. If I approximate this as a Gaussian distribution, the beam waist would be $w_0 = 2\sqrt{2}\lambda N/\pi = 0.71 \text{ } \mu\text{m}$, see appendix E, which is in agreement with the expected resolution limit. The oscillation frequency along the axial direction ω_z can be calculated using the Rayleigh length $z_0 = \pi w_0^2/\lambda \approx 2.0 \text{ } \mu\text{m}$:

$$\omega_z = \sqrt{\frac{-2U_0}{m z_0^2}}. \quad (7.9)$$

For $-U_0 = 1 \text{ mK} \cdot k_B$, this yields $\omega_z = 2\pi \cdot 35 \text{ kHz}$. The axial trapping frequency ω_z is significantly lower than the radial trapping frequency ω_r , which is generally the case for running wave optical dipole-force traps.

We now consider the dielectric mirror to be in the object plane of the microscope $L = 0$. The backward travelling wave interferes with the forward travelling wave

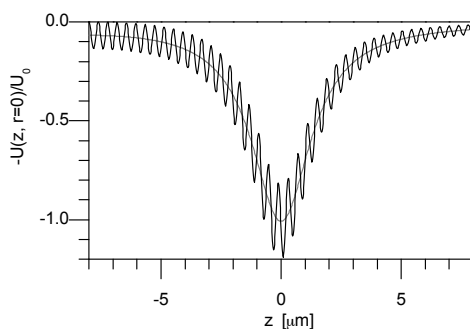


Figure 7.5 Potential depth $U(z)$ along the axis, with the focal point $8\ \mu\text{m}$ away from the mirror surface. The slowly varying average of the potential (gray) is a feature of focusing the light, whereas the oscillation (black) is caused by the partial standing wave. The modulation has the highest visibility close to the mirror-surface, becomes less pronounced in the focal spot, and then increases again further away from the focal point.

and gives rise to a longitudinal interference pattern, creating an ideal standing wave (see the central picture of Fig. 7.3). The potential has many local minima in which atoms can be trapped. The intensity modulation along the z -axis gives rise to the following longitudinal potential:

$$U(z) = A(z) \sin^2\left(\frac{2\pi}{\lambda} z\right). \quad (7.10)$$

The envelope of the modulation, $A(z) = 4U_0/(1+z^2/z_0^2)$, reaches its maximum at the mirror surface. Here U_0 is the potential depth only due to a single focused beam. Because the contrast of the modulation is one, $A(z)$ is also the trap depth of a local minimum at height z above the mirror. The largest achievable trap depth is $4U_0$, four times higher than without the mirror. Strictly speaking the first anti-node is $\lambda/4$ over the mirror, but this small deviation can be neglected. Therefore the maximum

radial trapping frequency in the standing wave configuration is $\omega_r^{st} = 2\omega_r = 2\pi \cdot 324$ kHz and is achieved close to the mirror. The longitudinal oscillation frequency inside a local trap at height z is given by

$$\omega_z^{st}(z) = \sqrt{\frac{-8A(z)\pi^2}{m\lambda^2}}. \quad (7.11)$$

Close to the mirror, the highest value $\omega_z^{st} = 2\pi \cdot 1100$ kHz is achieved.

When the mirror is not exactly in the image plane of the DMD (finite distance L), the forward and backward propagating waves do not have the same amplitude. Therefore the longitudinal intensity modulation has a peak-to-peak amplitude of:

$$A(z) = \frac{4U_0}{\sqrt{1 + z^2/z_0^2}\sqrt{1 + (2L + z)^2/z_0^2}}, \quad (7.12)$$

where the origin for z is defined to be the beam-waist and the mirror surface is situated at $z = -L$, see appendix E. The amplitude $A(z)$ rapidly fades away as the distance between the mirror and the focal plane increases. Fig. 5 shows the longitudinal potential $U(z)$ for $L = 8 \mu\text{m}$. The deepest local minima are found at the focus of the beam. In general the deepest local minima are found at $d = \sqrt{L^2 - z_0^2} - L$, for $|L| > |z_0|$, otherwise at $d = -L$, i.e. at the mirror surface. An atom trapped in one of these local minima sees a trap depth of about $1.37 U_0$ in the radial direction but only $0.3 U_0$ in the longitudinal direction. Whatever the distance between the focal plane and the mirror, the trap depth in the radial direction will always be larger than in the travelling wave case ($L \rightarrow \infty$) but smaller

than in the standing wave case ($L = 0$): $162 \text{ kHz} < \omega_r/(2\pi) < 324 \text{ kHz}$. Along the z -axis, the trapped atoms are confined either to the slowly varying envelope or to the local minimum, depending on their initial kinetic energy. Only the coldest atoms can be trapped in the local minima. If they are, their confinement shall be strongly improved. In that case the longitudinal frequency can be estimated from Eq. 7.11, with $A(z)$ given by Eq. 7.12. For the example of Fig. 5, one finds that the oscillation frequency at the focus of the beam is $\omega_z = 2\pi \cdot 300 \text{ kHz}$. Depending on L , the values of ω_z are intermediate between the travelling wave case ($L \rightarrow \infty$) and standing wave ($L = 0$) case: $35 \text{ kHz} < \omega_z/(2\pi) < 1100 \text{ kHz}$.

7.3 Ways to Single Atoms

In addition to controlling the size and depth of the traps, it is also important to control and measure the number of atoms. More specifically for the goal of conducting single atom experiments an efficient scheme to prepare single trapped atoms is essential. When loading atoms into moderately sized traps, the number of atoms therein is generally Poisson distributed. In this case, I would need to measure the atom number and then post-select traps with just one atom. Fortunately, for tightly focused dipole traps, the collisional blockade mechanism^[71] should give rise to a significant departure from the Poissonian statistics and favour the loading of only one atom per trap.

The effect occurs when atoms are loaded at a rate R from a magneto optical trap into tightly confined dipole traps. It relies on light-assisted collisions^[64] between

atoms in the presence of the MOT cooling beam. Provided the latter is strong enough to saturate the transition, two-body losses occur at a rate $\beta'N(N-1)$. N is the atom number and β' is the rate constant, which is inversely proportional to the trapping volume. There is also a single body loss process γN , which is mostly due to background collisions, so the full rate-equation^[72] for the entire loading process reads:

$$\frac{dN}{dt} = R - \gamma N - \beta'N(N-1). \quad (7.13)$$

Collisional blockade will occur when the two-body loss rate dominates over the loading rate of the dipole trap. Hence, it will work very efficiently when β' is large, this occurs when if the atoms are confined to a tiny volume. The volume occupied by the atoms depends on the temperature and the trapping frequency. A comparison of the frequencies achievable with the proposed set up, and the trapping frequency $\omega_t = 2\pi \cdot 200$ kHz of a previous experiment demonstrating the collisional blockade^[71] leads us to the conclusion that this mechanism could be highly efficient here as well. Due to the nature of the collisional blockade, the traps would be filled with a random pattern of atoms, with a filling factor of at most 50%. Nonetheless, in connection with an in-situ atom detection and subsequent rearrangement of occupied traps, scaling to very large arrays of single trapped atoms seems feasible.

7.4 Single Atom Detection and Transport

To investigate the loading processes, the atom numbers in the individual traps have to be determined. For well-isolated traps, laser induced resonance fluorescence could be used for atom counting^[73]. To collect the fluorescence, the lens system which creates the optical tweezers can be used in the backward direction as a microscope. This fluorescence is detected by a highly sensitive camera. This technique is nowadays routinely used to observe single atoms while trapped in microscopic dipole traps^[16,74,75].

To discuss the feasibility of single atom detection, the flux of photons impinging on the camera has to be determined. The geometrical collection efficiency η depends on the numerical aperture of the lens system. To evaluate η , I assume a uniform photon emission of the atoms and calculate the ratio of photons passing through the system. The ratio of the surface area of a spherical cap with that of a sphere, yields $\eta = 2\pi (1 - \cos(\frac{\alpha}{2})) / (4\pi)$, where α is the opening angle. For a numerical aperture of 0.5, $\alpha = 60^\circ$, I expect a collection efficiency of $\eta = 0.067$.

If the radiative transition of the atom is completely saturated, the scattering rate on resonance tends to $R_{scat} = \frac{1}{2}\Gamma$, hence $R_{scat} = 19.6 \mu\text{s}^{-1}$ for Rubidium. Assuming a further loss of 50% through the lens system, a camera should collect photons from a single atom with a rate of $R_{cam} = 653 \text{ms}^{-1}$. In other words, a camera operating with an exposure time of $100 \mu\text{s}$ could count as many as 65 photons. For modern electron multiplying charged coupled device (EM-CCD) cameras, this is well above the signal to noise threshold, so it is possible to use such devices to observe

single atoms. We emphasise that this estimate assumes no direct scattering of probe photons off the dielectric mirror into the camera. The latter effect can be eliminated altogether using a probe beam traveling parallel to the mirror surface.

The high frame rate of the DMD should allow for the reconfiguration of the potential landscape, and hence for the transport of confined atoms. A naive method would be to transport atoms adiabatically by changing the potential slowly enough so that the atoms are following without being heated. Since the DMD has only a finite resolution, this must be done using discrete steps. With the aforementioned trap consisting of a four by four block, as shown in Fig. 7.2, the pattern would have to be shifted by at most one pixel per step. The longest distance the traps could be moved is 1000 pixels, that is from one edge of the DMD to the other. With a refresh rate of 50 kHz, this transport would take 20 ms. This is much shorter than the anticipated lifetime of the trap, which should be of at least several 100 ms. However a drawback of this method is that discrete switching of mirror elements leads to parametric heating of the atoms. To circumvent this, the atom-transport could also be realised ballistically. The initially trapped atoms would be accelerated through a sudden change in trapping potential, guided through a channel and eventually decelerated and recaptured. This scheme has the advantage that it needs only a few changes in the potential, making it less susceptible to heating, and yet faster at the same time.

7.5 Conclusion

This chapter shows that the handling and manipulation of individual dipole-trapped atoms should be possible with an optical-tweezers type setup. The optical setup and most importantly the imaging of extended objects has to be investigated in detail. This will be done in the next chapter. In the following chapters the setup will be described and results about trapping and transport will be presented.

Chapter 8

Isoplanatism

This chapter investigates a very important detail of the optical tweezers, the optical imaging of extended objects with coherent light. This is important since the the optical tweezers are designed to have a diffraction limited resolution. As this chapter shows there are coherent effects that can degrade coherent imaging even though the imaging is perfect in the incoherent case.

This chapter summarises the article published in Optics Communications in 2009^[68]: "Coherent imaging of extended objects", by E. Brainis, C. Muldoon, L. Brandt & A. Kuhn, Volume 282, Page 465.

8.1 Introduction

Even aberration-free lens systems suffer from distortions, the most well known is the diffraction due to the limited aperture of the lens. For a lens system imaging coherent light there is an additional distortion due to non-isoplanatism^[76,77]. This

type of distortion can be easily understood in the framework of Fourier-Optics and linear systems. I will introduce the formalism briefly to investigate the phenomenon in more depth.

An optical system can be treated in the framework of linear systems^[77], since the Maxwell equations themselves are linear. For this investigation it is sufficient to restrict the treatment of the field propagation from an object plane \mathcal{O} to an image plane \mathcal{I} , which is parallel to the \mathcal{O} . The coordinates of the object plane and image plane are (x_o, y_o) and (x_i, y_i) respectively. A linear transfer-function $h(x_i, y_i | x_o, y_o)$ describes the propagation of the complex field from the object plane $U_o(x_o, y_o)$ to the image plane $U_i(x_i, y_i)$:

$$U_i(x_i, y_i) = \iint h(x_i, y_i | x_o, y_o) U_o(x_o, y_o) dx_o dy_o. \quad (8.1)$$

The specific appearance of the function $h(x_i, y_i | x_o, y_o)$, which is also known as the impulse response function, depends on the specific imaging system, but Eq. (8.1) is valid in general. For the rest of this thesis I will define the points of $(x_o, y_o) = 0$ and $(x_i, y_i) = 0$ as the points where the axis of the imaging system intersects the object and image plane.

The impulse response function is isoplanatic only if it is translationally independent in the object plane. Hence it can be written as:

$$h(x_i, y_i | x_o, y_o) = h(x_i - x_o \cdot M, y_i - y_o \cdot M), \quad (8.2)$$

where M is the magnification of the optical system. For aberration free systems the response function is generally only isoplanatic for the field amplitude, but not for the phase. This is the reason that for coherent imaging the non-isoplanatism can have a strong effect, but is not observed when the imaging is incoherent.

Isoplanatism was first recognised by Dumontet^[78], and later by Tichenor and Goodman^[79], who showed that a thin lens can only be considered as an isoplanatic system if both the object and the image lie on spherical surfaces \mathcal{S}_o and \mathcal{S}_i , tangent to the geometrical-optics object and image planes \mathcal{O} and \mathcal{I} respectively, and having their centre of curvature in the plane of the lens (see Sec. 8.2).

In practice, an aberration-free optical instrument can be treated as an ideal coherent-light imaging system whenever the spherical surfaces \mathcal{S}_o and \mathcal{S}_i can be approximated by their tangent planes \mathcal{O} and \mathcal{I} . I emphasize that this is only viable when the object to be imaged is very small and lies close to the optical axis.

8.2 Mathematical Formalism of Imaging

The thin lens here will be treated as linear system according to Eq. (8.1). The impulse response function of a thin lens^[77,79] is an important concept that has proven to be very useful for the design of optical systems and optical data processing. The value of z_i is related to z_o through the lens law $1/z_o + 1/z_i = 1/f$. The impulse response of a thin lens (in the paraxial and far-field approximation) is given by the

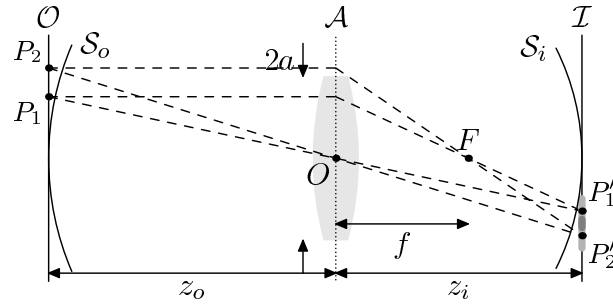


Figure 8.1 Scheme of coherent image formation by an aberration-free thin lens. The points P'_1 and P'_2 in the image plane \mathcal{I} are the geometrical images of the point objects P_1 and P_2 in the object plane \mathcal{O} . The light-gray zones around P'_1 and P'_2 in the \mathcal{I} -plane represent the individual diffraction patterns resulting from illumination of the lens by P_1 and P_2 respectively. The dark-gray zone represents the area where the individual diffraction patterns overlap and interfere.

Fraunhofer integral

$$\begin{aligned}
 h(x_i, y_i | x_o, y_o) &= \frac{1}{\lambda^2} \frac{e^{i2\pi(r+s)/\lambda}}{rs} \iint_{\mathcal{A}} e^{-i2\pi(f_x \xi + f_y \eta)} d\xi d\eta, \\
 &= \frac{1}{\lambda^2} \frac{e^{i2\pi(r+s)/\lambda}}{rs} \delta_a(f_x, f_y),
 \end{aligned} \tag{8.3}$$

where (x_o, y_o) are the coordinates of the point source in the object plane, (x_i, y_i) are the coordinates of the “observation point” in the image plane. The integration domain \mathcal{A} is the lens opening disc, while

$$\begin{aligned}
 r &= \sqrt{x_o^2 + y_o^2 + z_o^2}, \\
 s &= \sqrt{x_i^2 + y_i^2 + z_i^2}
 \end{aligned}$$

are the distances from the point source and the observation point to the lens centre, and

$$\begin{aligned} f_x &= \frac{1}{\lambda} \left(\frac{x_i}{s} + \frac{x_o}{r} \right), \\ f_y &= \frac{1}{\lambda} \left(\frac{y_i}{s} + \frac{y_o}{r} \right) \end{aligned}$$

are the spatial frequencies of the plane waves diffracted by the lens. On the second line of Eq. (8.3), the function

$$\delta_N(x, y) = |N| \frac{J_1(2\pi N \sqrt{x^2 + y^2})}{\sqrt{x^2 + y^2}} \quad (N \in \mathbb{R}_0) \quad (8.4)$$

has been introduced ($J_1(x)$ is a Bessel function of first kind). Its square $\delta_N^2(x, y)$ is the usual intensity point spread function or Airy pattern of diffraction-limited optical systems and it is normalized so that $\lim_{|N| \rightarrow \infty} \delta_N(x, y) = \delta(x, y)$ (the Dirac distribution). The “scaling” property,

$$\delta_N(Cx, Cy) = \delta_{CN}(x, y)/C^2 \quad \text{for any } C \text{ in } \mathbb{R}/\{0\}, \quad (8.5)$$

can be used to simplify (8.3):

$$\begin{aligned} h(x_i, y_i | x_o, y_o) &= |M| e^{i\frac{2\pi}{\lambda}(r+s)} \times \\ &\delta_{\frac{a}{\lambda s}}(x_i - Mx_o, y_i - My_o), \end{aligned} \quad (8.6)$$

where $M = -s/r$ is the geometric *magnification ratio* of the lens. Note that the approximation $M \approx -z_i/z_o$ is justified, because r and s vary only very slightly over the object and image planes. For the same reason, $\delta_{a/(\lambda s)}(x, y) \approx \delta_{a/(\lambda z_i)}(x, y)$.

The phase factor in Eq. (8.6) plays an important role. If the phase factor were not there, the impulse response function would only be $\delta_{\frac{a}{\lambda s}}(x_i - Mx_o, y_i - My_o)$ and according to Eq. (8.2) it would be isoplanatic. Hence the image of a coherent object with field amplitude $U_o(x_o, y_o)$ could be computed by simply convoluting $U_o(x_o, y_o)$ with the impulse response function. The example of Fig. 8.2 clearly shows that this is not the case, because the impulse response function includes a phase factor, which depends on the coordinates in the object plane. This creates interference patterns that modify the image more significantly than a simple blur. The image of a field profile $U_o(x_o, y_o)$ is given by

$$U_i(x_i, y_i) = \frac{1}{|M|} e^{i\frac{2\pi}{\lambda}s} \iint U_o(x_o, y_o) e^{i\frac{2\pi}{\lambda}r} \delta_{\frac{a}{\lambda z_o}}\left(\frac{x_i}{M} - x_o, \frac{y_i}{M} - y_o\right) dx_o dy_o. \quad (8.7)$$

To establish Eq. (8.7), I make use of the scaling property (8.5). The function $\delta_{\frac{a}{\lambda z_o}}\left(\frac{x_i}{M} - x_o, \frac{y_i}{M} - y_o\right)$ can be considered either as a function of (x_i, y_i) , the usual Airy pattern centered on the geometrical image point (Mx_o, My_o) , or as a function of (x_o, y_o) centered on the object point $(x_i/M, y_i/M)$. Note that in the first interpretation, the first-zero full-width of the Airy pattern $e_i = 1.22\lambda z_i/a$ represents the region of the image plane most influenced by the field originating from the point source at

(x_o, y_o) in the object plane. In the second interpretation, the first-zero full-width of the Airy pattern $e_o = 1.22\lambda z_o/a$ represents the area of the object plane that most contributes to the field at the observation point (x_i, y_i) in the image plane. In the *non-isoplanatic* situation described by Eq. (8.7), important interferences occur when the phase factor $\exp[i\frac{2\pi}{\lambda}r]$ cannot be considered as constant over the circular region of area $\pi(e_o/2)^2$ centered on $(x_i/M, y_i/M)$ in the object plane.

It is interesting to note that isoplanatism is recovered when one considers the imaging problem from \mathcal{S}_o to \mathcal{S}_i (see Fig. 8.1), where \mathcal{S}_o (\mathcal{S}_i) is a spherical surface of radius z_o (z_i) centered on the lens, and having its vertex on \mathcal{O} (\mathcal{I}). The spherical field distributions on \mathcal{S}_o and \mathcal{S}_i are described by the amplitudes $U_{\mathcal{S}_o}(x_o, y_o)$ and $U_{\mathcal{S}_i}(x_i, y_i)$, respectively (z -coordinates are dependent variables). These are related to the field amplitudes on \mathcal{O} and \mathcal{I} by a phase relations:

$$\begin{aligned} U_{\mathcal{S}_o}(x_o, y_o) &= U_o(x_o, y_o) \exp[i2\pi(r - z_o)/\lambda] \\ U_{\mathcal{S}_i}(x_i, y_i) &= U_i(x_i, y_i) \exp[-i2\pi(s - z_i)/\lambda]. \end{aligned}$$

Inserting these relations into Eq. (8.7) and removing the constant phase factor $\exp[i2\pi(z_o + z_i)/\lambda]$ one gets:

$$\begin{aligned} U_{\mathcal{S}_i}(x_i, y_i) &= \frac{1}{|M|} \iint U_{\mathcal{S}_o}(x_o, y_o) \\ &\quad \times \delta_{\frac{a}{\lambda z_o}}\left(\frac{x_i}{M} - x_o, \frac{y_i}{M} - y_o\right) dx_o dy_o \end{aligned} \quad (8.8)$$

which is a convolution relation, as expected for an isoplanatic imaging system. The

physical reason why isoplanatism is recovered when the object lies on the spherical surface \mathcal{S}_o is simple to understand: since all the point sources are at same distance z_o from the lens, their point spread functions always interfere constructively.

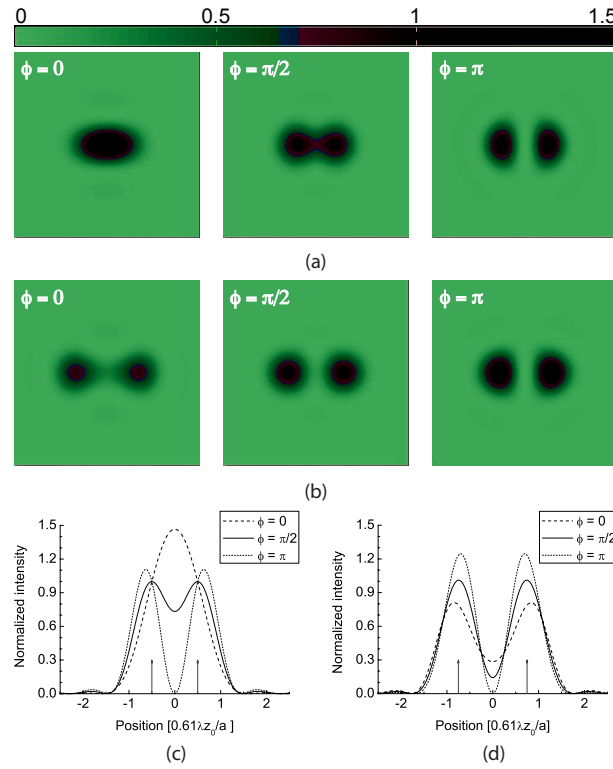


Figure 8.2 Intensity profile in the image plane of a diffraction-limited lens due to the interference of the Airy patterns of two coherent point sources. The distance $|x_{o,1} - x_{o,2}|$ between the sources is equal to (a) $0.61\lambda z_o/a$ (the Rayleigh resolution limit), and (b) $0.915\lambda z_o/a$ (1.5 times the Rayleigh resolution limit). The Airy patterns have been normalised so that their peak intensity is 1. Panel (c) and (d) show the intensity profiles along the x -axis corresponding to the images in panel (a) and (b), respectively. Vertical arrows in panels (c) and (d) point the positions of the centres of the interfering Airy patterns.

8.3 Isoplanatic Imaging Through a Thin Lens

In Sec. 8.2, I claimed that isoplanatic imaging is possible with a thin lens when the object lies on the spherical surface \mathcal{S}_o and the image is observed on the spherical surface \mathcal{S}_i . Let's examine this statement more closely.

Referring to Fig. 8.1, simple Gaussian Optics arguments suggest that if the point P_2 is translated horizontally from the object plane \mathcal{O} to the surface \mathcal{S}_o , its image P'_2 , instead of moving towards \mathcal{S}_i , should move away from the lens. This argument is correct, but it relies on the Gaussian approximation that the point P'_2 is initially in the "image plane" \mathcal{I} . In reality, because of the field curvature aberration due to the lens, the stigmatic image of P_2 is closer to the lens than the surface \mathcal{S}_i itself (P'_2 lies on the so-called Petzval surface). Bringing P_2 on \mathcal{S}_o will place its image P'_2 exactly on \mathcal{S}_i ^[80]. Consequently, Eq. (8.8) is exact, while Eq. (8.7) is only valid in the context of Gaussian approximation. If the lens is still diffraction-limited in this regime (no point-aberrations), the isoplanatic imaging geometry provides a nearly perfect transfer of the coherent field from the object to the image space. Only the resolution is reduced because of the finite size of the lens.

The problem that remains is how to transfer a given field from a plane surface to a curved one before imaging, and vice versa after imaging. Generally, the object field is obtained by modulating a coherent illumination field $A(x_o, y_o)$ by a complex amplitude function $u_o(x_o, y_o)$:

$$U_o(x_o, y_o) = A(x_o, y_o) \times u_o(x_o, y_o). \quad (8.9)$$

The modulation $u_o(x_o, y_o)$ can be produced by any plane modulation device like a plane transparency, a grating or some kind of adaptive optics. Usually $u_o(x_o, y_o)$ itself is considered as the “object” of interest. In that case, the illumination beam must be a plane wave propagating along the optical axis in order to map the profile $u_o(x_o, y_o)$ to the beam: $U_o(x_o, y_o) \propto u_o(x_o, y_o)$. If, instead, I illuminate the modulation device with a spherical wave $A(x_o, y_o) = A \exp(-i2\pi r/\lambda)$ focusing on O (see Fig. 8.1), I get $U_{S_o}(x_o, y_o) = U_o(x_o, y_o) \exp(i2\pi r/\lambda) \propto u_o(x_o, y_o)$. This kind of illumination projects the object onto S_o as required for isoplanatic imaging^[77]. Starting with an illuminating plane wave travelling along the optical axis, this can be achieved by placing an additional thin lens of focal length z_o just before (or just after) the object plane \mathcal{O} . This lens must act as a pure phase-correction transparency. Similarly, on the image side, a thin lens of focal length z_i placed just after (or before) the image plane can be used to project the image from S_i onto \mathcal{I} . From a broader point of view, any spherical field distribution in the object space of a centered paraxial optical system can be imaged onto a spherical surface of any curvature using only lenses; some of them will be imaging lenses, while others will play the role of phase-correction transparencies.

It should be noted that this approach only works for sufficiently slowly varying fields, because the diffraction from \mathcal{O} to S_o (and S_i to \mathcal{I}) has to be negligible for the amplitude of the fields on \mathcal{O} and S_o (S_i and \mathcal{I}) being the same. In addition, due to optical design constraints, the use of optical lenses as phase-correction transparencies is not always possible. Moreover, lenses are never perfectly thin and diffraction

through them may have worse effects on imaging than the phase curvature due to non-isoplanatism. Whether or not non-isoplanatism should be corrected depends on the particular system under consideration. A clever design can minimise, if not cancel, its effects on the detected intensity.

8.4 Experimental Investigation

The theoretical discussion relies on two strong approximations: the paraxial approximation and the thin lens approximation. One may wonder whether this analysis is robust enough to be applied to systems containing powerful lenses, which are usually thick and have a high numerical aperture. The following experiment shows that the previous discussion is also valid for these systems.

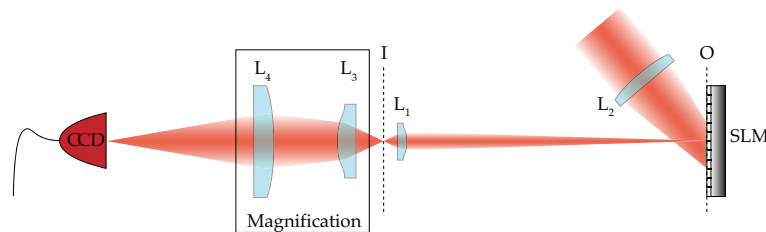


Figure 8.3 Experimental setup: L_1 , aspheric lens ($f = 8$ mm); L_2 , achromatic doublet ($f = 750$ mm); L_3 , aspheric lens ($f = 20$ mm); and L_4 , achromatic doublet ($f = 500$ mm); SLM, spatial light modulator; CCD, coupled-charge camera; O, object plane; I, image plane.

The setup is shown in Fig. 8.3. The test lens L_1 is an aspheric lens having a focal length $f = 8$ mm and a diameter $2a = 8$ mm (LightPath 352240). This lens is used to image the surface of a spatial light modulator (SLM), a 1024×768 micromirror array, that modulates the amplitude of the reflected beam and can

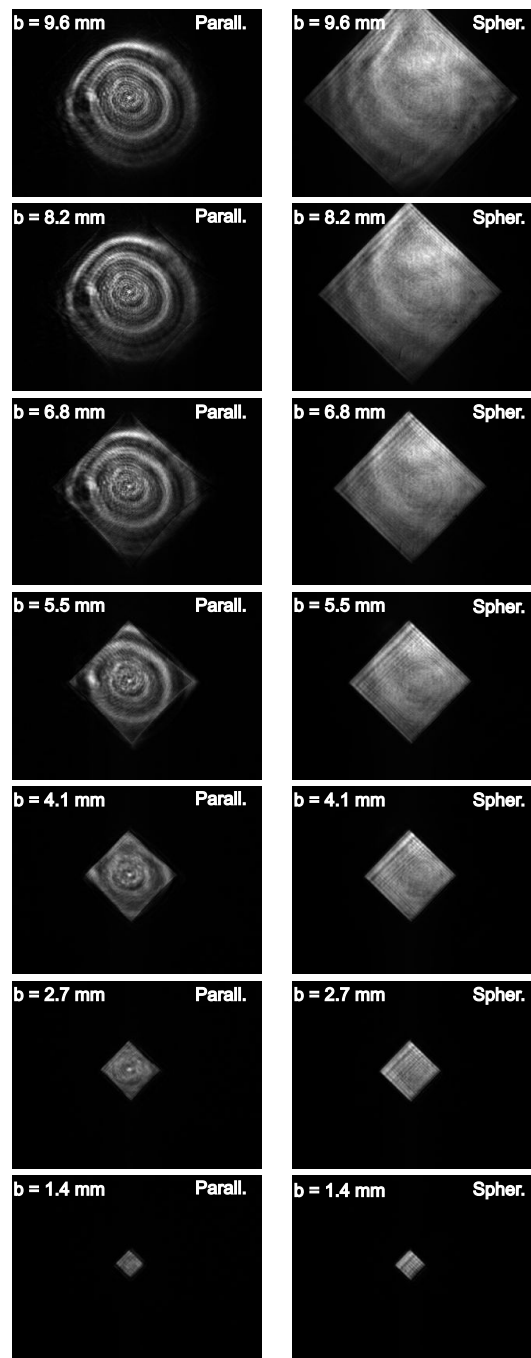


Figure 8.4 Images of different-sized squares (the side b ranges from 1.4 mm to 9.6 mm) recorded using the setup in Fig. 8.3. The object plane is either illuminated with a parallel beam (non-isoplanatic case, left column) or with a spherical one converging on L_1 (isoplanatic case, right column).

generate arbitrary patterns. The resolution is set by the size of the micromirrors ($13 \times 13 \mu\text{m}^2$). The object plane is 60 cm away from the lens. A double-lens system (L_3, L_4) is used to magnify the image produced and project it on the CCD camera. L_3 is a diffraction-limited aspheric lens and L_4 a long-focal achromatic doublet. The numerical aperture of this double-lens system is large enough to prevent any possible clipping or diffraction during the magnification process. The SLM is either illuminated with a plane wave or a spherical wave converging on L_1 ($\lambda = 780 \text{ nm}$). In the first case, the imaging system is non-isoplanatic. As explained in Sec. 8.3, it becomes isoplanatic when a spherical-wave illumination is used. The spherical wave is obtained from the impinging plane wave by inserting the additional lens L_2 (75-cm focal length, achromatic doublet) in front of the SLM. We use this setup to image objects of different sizes and shapes through the test lens.

Fig. 8.4 shows the pictures recorded by the CCD camera when squares of different sizes are imaged through the 8-mm diameter aspheric lens L_1 . First consider the case when the SLM is illuminated by a parallel beam (non-isoplanatic imaging, left column of Fig. 8.4). For a square side larger than 8 mm, the clipping effect is clearly observed and circular fringes are also seen in the image plane. For a square side smaller than 8 mm, the region of non-zero intensity is limited by the size of the square. However, intensity modulation due to non-isoplanatism is still noticeable for a square side as small as 2.7 mm. In the case of the $1.4 \times 1.4 \text{ mm}^2$ square, non-isoplanatism has a negligible effect. Here, the lens is always the same, but the square size is varied instead. For this reason, the ring pattern is the same for every

picture in the left column of Fig. 8.4. When the SLM is illuminated with a spherical wave converging on L_1 no clipping effect occurs and there is, in principle, no limit to the size of the objects that the system can image (the slight variations in intensity are due to amplitude inhomogeneities in the illumination beam).

8.5 Conclusion

In general, even diffraction-limited imaging systems distort the phase of the processed fields. This is of no relevance when used with incoherent light, but has a tremendous effect on coherent imaging. In combination with Fraunhofer diffraction from the finite instrumental aperture, the phase distortion leads to a severe degradation of the field amplitude in the image plane. The main aspects of the theoretical analysis have been confirmed experimentally using a powerful thick aspheric lens to demonstrate that the phenomenology that is described also holds beyond the paraxial and thin lens approximations used for the theoretical analysis. These results are very important for the design of the optical tweezers, since there coherent light is used to image the SLM to create the trap, by including the spherical illumination into the setup.

Chapter 9

Optical Tweezers Setup

This chapter contains the implementation of the optical tweezers, mainly the optical setup. It consists of two building blocks: the optics to generate the trap and the elements to image the trapped atoms. As the experiment contains a retro-reflecting mirror, it is not possible to have two independent setups for the two tasks. The imaging and trapping is done along the same beam path, see Fig. 7.1. This has the advantage that fewer optical elements are required.

9.1 The Trap Setup

The idea of the trap generation is to image the DMD (digital mirror device) onto the mirror in the vacuum chamber. This creates a standing wave pattern along the vertical, which confines the atoms along the vertical axis. The intensity distribution of the image confines the atoms in the horizontal planes. A high-power diode laser, Toptica DLX-110, see Chapter 5.1.2, illuminates the DMD. This illumination is

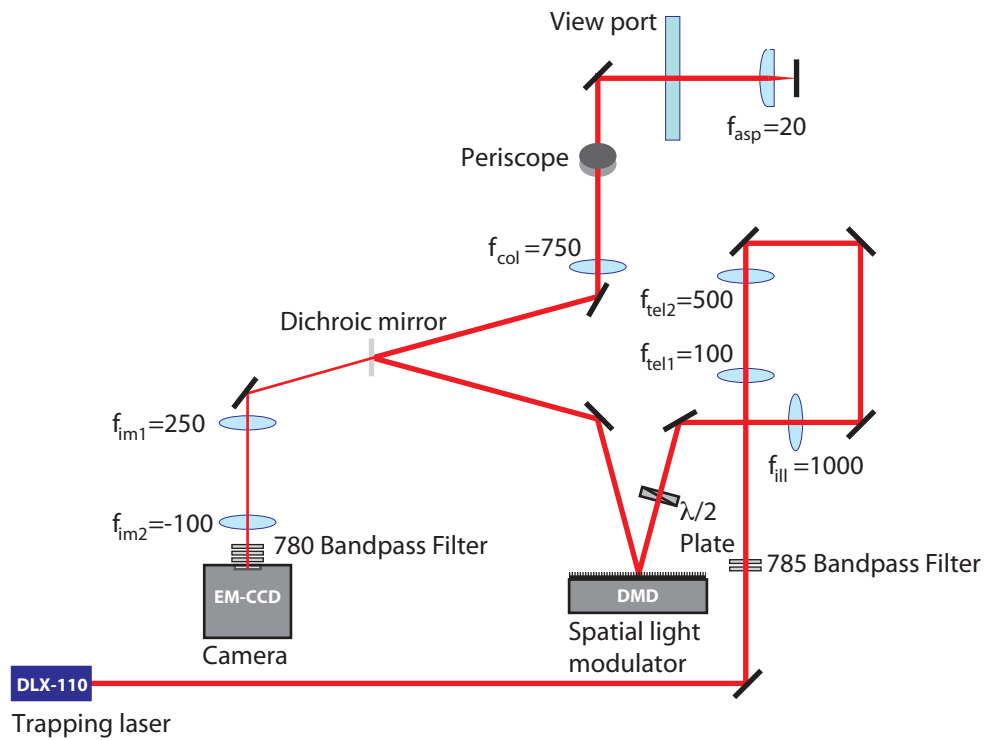


Figure 9.1 Sketch of the laser set up for the optical tweezers.

convergent to achieve isoplanatic imaging of the DMD, see chapter 8. Since it has proven difficult to operate the MOST close to the mirror surface, the tweezers are generated 0.55 mm above the mirror-surface. For large traps the partial standing wave is strong enough to support the atoms along the vertical axis, whereas for small traps, the vertical confinement is due to the divergence of the field.

9.1.1 The Digital-Mirror-Device

The DMD, Texas Instruments DMD Discovery 1100, has an active area that consists of 1024 by 768 bistable mirrors. They can tilt individually by $\pm 12^\circ$, which reflects the light either into the imaging optics or into a beam-stop. This creates a digital

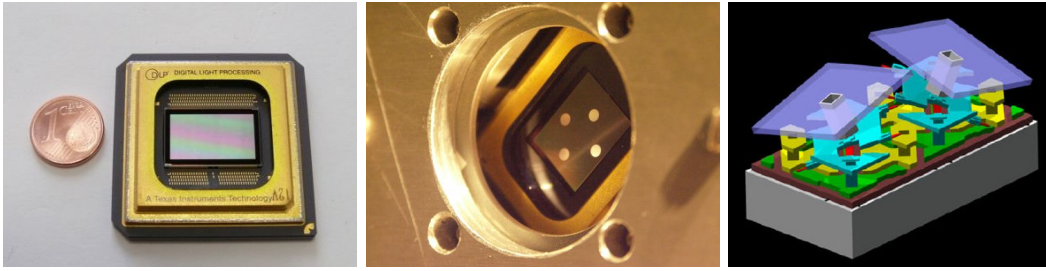


Figure 9.2 On the left is the bare DMD chip. In the centre is the mounted DMD with a pattern is written on it. The left picture is a scheme of the individual micro mirrors.

pattern. Each individual mirror has size of $13.68 \mu m$ by $13.68 \mu m$, so the entire optical surface has a size of $14 mm$ times $10.5 mm$.

Partial absorption of the incident light leads to heating of the DMD. The maximum operation temperature is $65^\circ C$, which is the damage threshold of the system. The DLX-110 illuminates the DMD with $P_{ill} \approx 0.5 W$, this leads to a heating of $P_{ill} \cdot \alpha_{DMD} = 82 mW$, where $\alpha_{DMD} = 16.3\%$ is the absorption coefficient of the DMD. This heating is negligible compared to the electrical operational heating $P_{el} = 2 W$. In case high intensities are required, the DMD can be cooled.

The DMD is computer controlled using a standard desktop PC, with a programme developed in the group. There are two different modes in which the DMD can be controlled, either the whole DMD can be refreshed, this happens with a slow rate of $1/(260 \mu s)$. Alternatively only blocks of 48 by 1024 pixels can be changed at a faster rate of up to $1/(50 \mu s)$.

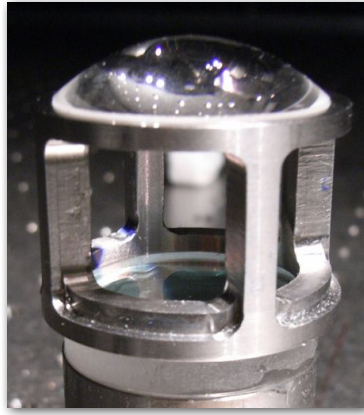


Figure 9.3 Picture of the aspheric lens on a lens holder mounted on a dielectric mirror.

9.1.2 The Optical Setup

The design criteria for the trap generation is to spatially control the atoms with a sub-micron precision, i.e close to the wavelength of the trapping light. Therefore an aberration-free lens system with a high numerical aperture is required, e.g. either a lens system with a number of spherical singlets or a single aspherical lens.

The light transverses the viewport, which is 9 mm thick fused silica, to enter the vacuum chamber. This leads to aberrations when a convergent light beam propagates through it. To counteract the aberration, one can either correct for the aberration through the design of lens system, or let the parallel light propagate through the viewport and use a lens system inside the vacuum chamber. The second option was chosen here and an Aspheric lens was mounted inside the vacuum chamber. This lens, 25-20 HPX-S from Asphericon: $f=20$ mm, $D=25$ mm, $NA=0.54$, design wavelength $\lambda = 780$ nm, made of glass (S-LAH64), and coated with

a broad band antireflection coating (600-1500 nm), is aberration-free (Wavefront error RMS=500 nm) for monochromatic light propagation along its optical axis.

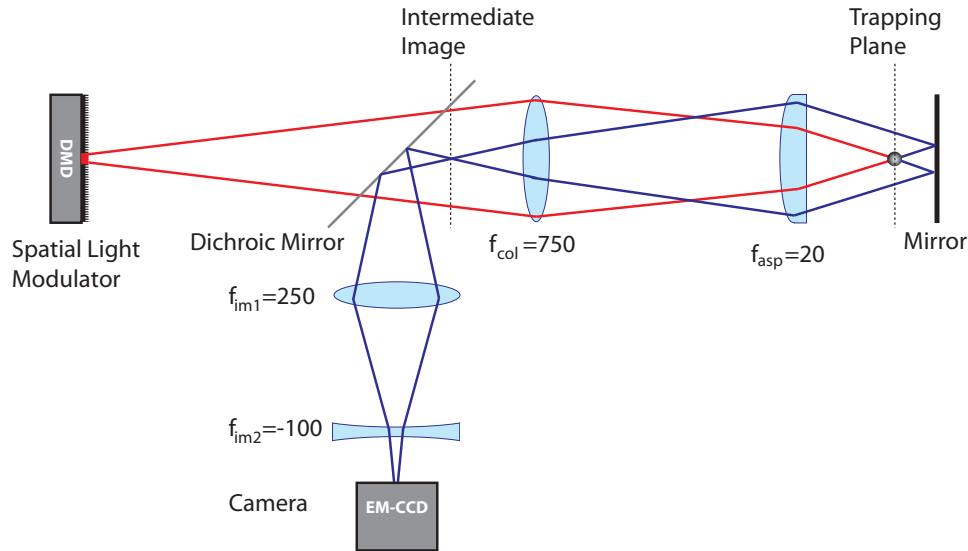


Figure 9.4 Simplified scheme of the optical setup. The collimator and the aspheric lens image the DMD to a plane 0.5 mm in front of the mirror surface (depicted by the red rays). The fluorescence of the trapped atoms (depicted by the blue rays) is reflected of the mirror surface and propagates through the aspheric lens and the collimator. After the collimator a virtual image is formed. The fluorescence light is then split of with a dichroic mirror and imaged onto a EM-CCD camera.

The lens is mounted on a on a stainless steel holder sitting on the MOST-mirror, see Fig. 9.3. The mount is designed to hold the lens 20.1 mm above the mirror surface. To allow for sufficiently large optical access to the MOST the holder design consists of only four fine pillars, which are least obstructive.

To raise the trapping plane 0.5 mm above the mirror surface, a collimating lens ($f_{coll} = 750$ mm) is placed outside the vacuum chamber at a at a distance of 450 mm to the aspheric lens, see Fig. 9.4. These two lenses image the DMD, which is placed

1660 in front of the collimating length lens. The resulting image magnification is $1/58$.

The DMD is illuminated by the light of the DLX 110, see chapter 5. To do so the incoming beam is first widened with a telescope see Fig. 9.1, and then collimated with lens ($f_{ll}=1000$ mm) to illuminate the DMD isoplanatically. Ideally the lens should focus onto the imaging lens, however, in order to have nearly flat face fronts in the trapping area, the lens was focussing one focal length (of the imaging lens) in front of the imaging lens. For a good loading efficiency of the dipole trap from the MOT it is crucial to have linear polarised trapping light^[64]. Since the dielectric mirrors show birefringence for light which has a nonzero angle of incidence, it is crucial to orient the polarisation axis of the light either in the plane of incidence or perpendicular to it, i.e. either horizontal or vertical. Furthermore the DMD is birefringent. Originally one half-wave-plate was placed in front of the DMD to align the polarisation of the light with the birefringend axis of the DMD. Then a second half-wave plate behind the DMD undoes the previous polarisation rotation. It turned out that one half-wave plate is sufficient to achieve a the same loading efficiency as with two, hence the second one was removed.

9.2 The Imaging Setup

The ultimate goal of the optical tweezers is to trap, manipulate and observe single atoms. Hence the imaging setup has to be able to detect small fluorescence signals. Furthermore the trapping involves multiple laser beams of high intensity. Compared

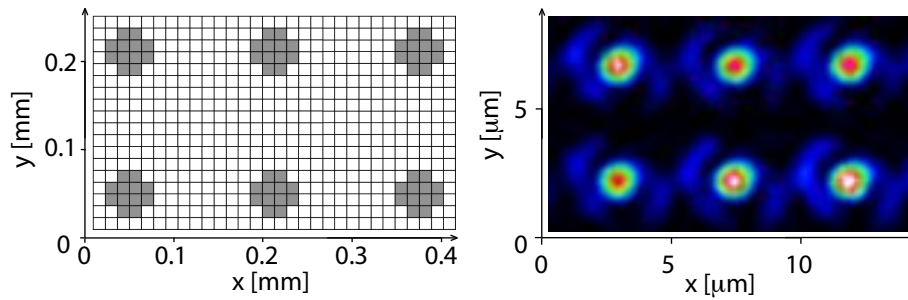


Figure 9.5 On the left is the pattern which is written on the DMD. The right picture shows the resulting intensity distribution. (The picture does not contain atoms.) This picture has been taken by imaging the DMD with the aspherical lens and then imaging the traps with a CCD-camera.

to emission of a single photon into the imaging system $P_{atom} = 10.2 \text{ pW}$, see Eq. (7.4). This is a factor 10^{11} smaller than the radiation produced by the various lasers. So the approach to tackle these challenges is twofold: an extremely sensitive EM-CCD camera (electron-multiplying-CCD) is facilitated to detect very weak signals and additionally optical filters and optical shielding are applied to minimise the background light.

To resolve individual traps the imaging system has to have the same resolution as the one generating the traps. Since the same optics are used for the imaging as for the trap generation, this is the case. The further advantage is that fewer elements have to be used in the setup. The drawback is that it is not possible to independently adjust the trapping and the imaging.

The trap is observed through the reflected image see Fig. 9.4, hence the path length between the aspherical lens and the trap centre is increased by twice the distance trap centre and the mirror surface $\Delta d = 1 \text{ mm}$. This distance increase

leads to a decrease in distance behind the collimating lens and the image is formed 86 mm behind it. This intermediate image is then imaged onto the camera using two lenses $f_{im1} = 250$ mm and $f_{im2} = -100$ mm, see Fig. 9.1 . The magnification of this configuration is 35.8. A dichroic mirror, which reflects the 785 nm radiation at 13° and transmits at 780 nm, separates the fluorescence light from the reflected trap light. It is situated after the collimator lens.

9.2.1 The EM-CCD Camera

CCD cameras are proven to be versatile for imaging, but they suffer from amplifier noise. This is the noise added due to the amplification of the read out CCD signal. Single photons induce a single electrons in the CCD-detector with a quantum efficiency of 40 %, which has to be amplified for further data processing. Since the amplifier noise tends to be significantly larger than the signal of a single photon, CCD-cameras are generally not suited for single photon detection.

EM-CCD cameras combine the versatility of a CCD-camera with a high amplification and a low signal to noise ratio. It differs from an standard CCD by amplifying the signal when passing it down the charge coupled chain. In ordinary devices the potential is changed by only few volts to move the electrons down the chain, whereas in an EM-CCD the potentials are ramped up to 60 V to induce impact-ionisation, see Fig. 9.6, which increases the number of charges. This process only has a low efficiency of up to 1.5%, but if repeated sufficiently often it will amplify the signal well above the amplifier threshold.

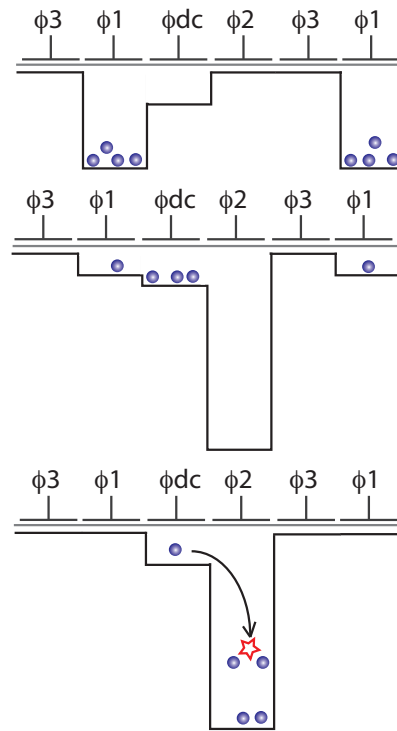


Figure 9.6 The concept of the EM-CCD charge transfer and amplification: In the top picture the charge is trapped in the potential ϕ_1 . It is then transferred into the potential ϕ_2 by decreasing the potential depth of ϕ_1 , while switching on a very deep potential ϕ_2 . When the electrons fall into the deep potential they have enough energy to generate secondary electrons through impact-ionization.

The EM-CCD camera, iXion 885 from Andor, used here has a resolution of 1004 times 1002 pixels. Each pixel has a size of $8\ \mu\text{m} \cdot 8\ \mu\text{m}$. The highest readout rate is 35 MHz, so the maximum full frame rate is 31 /s and a resolution of 14 bit. By cropping the image and by binning pixels, from two by two up to sixteen by sixteen the frame rate can be significantly increased, since the effective number of pixel is reduced. The shortest exposure time is $50\ \mu\text{s}$ and the EM-Gain is up to 1000, but we limit it to 300 to avoid damaging the camera. The camera has an external trigger

input, which is used to link it with the lab control computer.

The overall collection efficiency η_{tot} of the optical system is the product of the collection efficiency of optical system $\eta_{coll} = 0.067$, the losses along the optical beam path $\eta_{opt} = 0.5$ and the quantum efficiency of the camera $\eta_{cam} = 0.4$. The overall efficiency is $\eta_{tot} = 1.3\%$, i.e. the atom scatters 77 photons for a single photon observed with the camera.

9.2.2 Optical Filters and Shielding

There are two sources of background light in the experiment: scattered light from the cooling-laser and the repump-laser, which is near resonant, and far off-resonant light from the dipole-trapping laser. The optical path of the fluorescence and trapping light coincide before the dichroic mirror, hence a significant amount of the light enters the imaging setup through the dichroic mirror, which has a transmission $T_{785} \approx 10^{-3}$ for the dipole-trapping light. The transmitted power of the trapping light still exceeds the intensity of the single-atom fluorescence by a factor of 10^8 . Three bandpass filters, Semrock Maxline LL01-780, with an optical depth of 4.5 at 785 nm each reduce the intensity of the remaining light to a factor of $10^{-5.5}$ with respect to the single-atom fluorescence, which is an insignificant for the imaging with the EM-CCD camera. However, the DLX-110 radiates not only on the narrow resonance, but also contains a weak but broad pedestal of amplified spontaneous emission (ASE), which adds to the background in the imaging and unwanted heating in the trap. Two bandpass filters centred at 785 nm, Semrock Maxline LL01-785,

placed in the beam path before illuminating the DMD to remove this ASE-pedestal.

The near-resonant light of the cooling-laser and the repump-laser cannot be eliminated by a bandpass filter. Hence great care has to be taken to arrange the optical beam paths to minimise the scattering of the repump and cooling beam into the fluorescence imaging. Even the scattering of optical surfaces is observable with the EM-CCD camera. Hence there are multiple optical shields on the optical table to block all possible scattered light.

One particular source of stray light is the illumination laser beam, which is resonantly illuminating the trapped atoms to induce the fluorescence. One possibility would be to use background free fluorescence measurements^[81], which relies on a two step excitation process and subsequent spontaneous emission along a different path, which leads to fluorescence light different to the excitation light. Here I choose a different method. To avoid any scatter of the surface of the mirror, the laser beam, with a beam radius of 1.5 mm and $P = 2\text{ mW}$, is focussed with a lens $f = 300\text{ mm}$ to a waist $w = 50\text{ }\mu\text{m}$. The intensity of the laser in the focal point is $I \approx 20.000I_{sat}$, taking the Gaussian beam shape into account this leads to a diameter of $225\text{ }\mu\text{m}$ where the beam has an intensity greater I_{sat} . This diameter is large enough to illuminate all trapped atoms and is still much smaller than the distance between the trap centre and the mirror. This power was chosen in order to maximise the signal to noise ratio and to illuminate all the trapped atoms. Alternatively a beam with a larger waist and a much lesser peak intensity could have been used. For further measurements, which will be presented in the thesis of Cecilia Muldoon, the spher-

ical lens has been replaced by a cylindrical lens to illuminate one layer of the trap with a thin light sheet.

Chapter 10

Optical Tweezers Results

This chapter shows the first results of atoms captured in various optical tweezers arrangements. These trap geometries are far more complex than those which can be generated with simple gaussian beams. The trapped atoms are observed by absorption imaging and fluorescence imaging.

10.1 Absorption Imaging

The first observed loading of atoms into a complex, i.e. more complex than a single round trap, tweezers was achieved by two relatively large dipole traps, which have roughly the shape of semi circles each, see Fig. 10.1. Each trap has a size of about $31\ \mu\text{m}$ times $41\ \mu\text{m}$ with gap of $39\ \mu\text{m}$ inbetween. This trap geometry was generated by a combination of an oval shaped laser beam, with beam waists of $w_x = 5\ \text{mm}$ and $w_y = 2\ \text{mm}$, and an DMD pattern, where the whole DMD was switched on, except for vertical stripe in the centre with a width of 165 pixels was switched off.

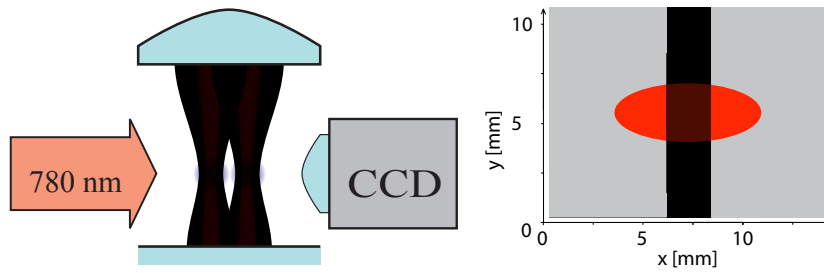


Figure 10.1 (left) Scheme of the absorption imaging. A resonant laser beam illuminates the atoms from the left propagating towards a camera on the right. The trapping plane lies horizontal. (right) The trapping pattern loaded onto the DMD. The light gray areas are switched on, whereas the black area is switched off. The DMD is illuminated with an oval laser beam (red oval). This combination produces two traps, each has roughly a shape of a semi circle. This pattern is demagnified by a factor of 58 in the trapping plane.

The Rayleigh length of this configuration is ≈ 5 mm, which is much larger than the distance between the center of the trap and the mirror surface ≈ 1 mm, therefore a standing wave forms. The power of the trapping beam is 250 mW, which leads to a trap depth of $U_{trap} = 969 \mu\text{K}$ in this configuration.

The atoms were detected by absorption imaging, see Fig. 10.2. The illumination beam was tuned on atomic resonance $F=2 \leftrightarrow F'=3$, it had a width of $w = 5$ mm, a power of $100 \mu\text{W}$ and a duration of $10 \mu\text{s}$. The resulting peak intensity was $I_0 = 0.25 \text{ mW}/\text{cm}^2$, which is a factor six below the saturation intensity. The axis of the imaging lay in the trap-plane, hence the atom distribution along the trap beam axis can be determined. The pictures clearly show a vertical distribution of the atoms. The Atoms are loaded close to the trapping plane from the MOST into the tweezer. Then they start to diffuse along the axis of the traps. If the outgoing and incoming trapping beam would have the same spatial intensity distribution, a standing wave

with full contrast would build up, see Fig. 7.3. However if the shape of the incoming and outgoing beam is not exactly the same, for example due to the imaging or due to a tilt angle with respect to the mirror surface, the contrast of the standing wave is reduced. This might explain the diffusion along the axis as observed in Fig. 10.2.

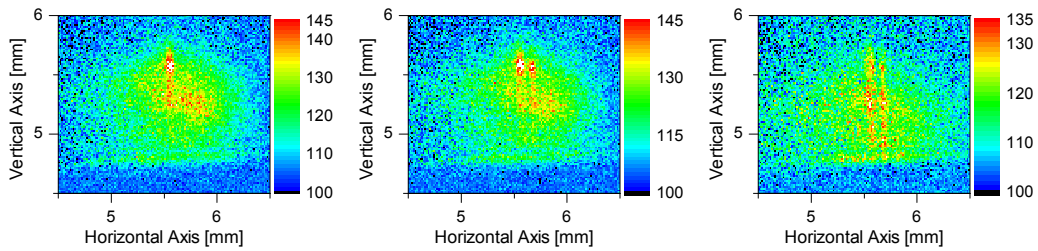


Figure 10.2 The pictures show absorption images of trapped atoms. (left) Atoms in a single circular dipole trap. (middle) Atoms in two circular traps. Both images have been taken directly after the loading of the dipole trap from the MOST. The signal in the background is due to the expanding cloud of un-trapped atoms. (right) The atoms diffuse along the trapaxis after 15 *ms*.

10.2 Fluorescence Imaging

The absorption imaging has two drawbacks. The first is of principle nature, it needs a minimum density of atoms to give reasonable results. The optical cross section for Rubidium for the $D_2(F=2, F'=3)$ transition is $\sigma_0 \approx 2 \cdot 10^{-9} \text{ cm}^2$. Therefore the atom number per cross-section has to be 5 per μm^2 . For a moderately sized trap of $30 \mu\text{m}$ by $30 \mu\text{m}$ roughly 5000 atoms have to be in the trap. The aim of this project is to manipulate few or single atoms. For this regime this method is clearly not feasible. The second disadvantage is due to the geometry of the trapping set up, the absorption imaging is perpendicular to the trapping plane, hence in general

individual traps cannot be resolved.

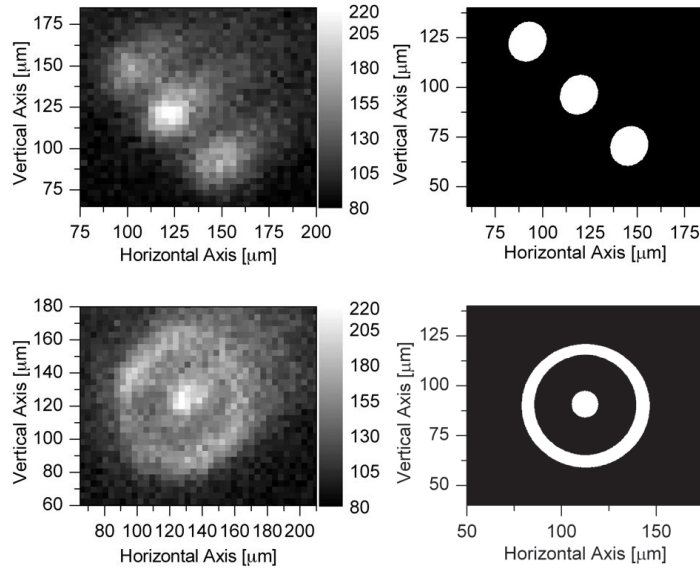


Figure 10.3 In the left column are fluorescence images of trapped atoms. The full trap pattern loaded onto the DMD is shown on the right. A tail of atoms leaking out of the trap is visible in the upper left corner. The illumination laser beam pushes the atoms into this direction.

Fluorescence imaging does not suffer from these disadvantages, it is very sensitive method for the observation of few atoms. It is limited by the signal to noise ratio of the imaging. The factors that contribute to the signal to noise ratio are the amount of stray-light entering the camera, and the signal to noise ratio of the camera itself. The EM-CCD camera observing the atoms is optimised for single and few photon observation, see section 9.2.1. The stray light can be minimised as discussed in section 9.2.2.

The atoms were illuminated while still in the trap. Nonetheless this method is destructive. The combined photon detection efficiency is 1.3%, therefore the atom

is heated by about $145 E_{rec}$ per observed photon, which corresponds to $53.6 \mu\text{K}$. To illuminate the pattern as close as uniformly the beam is $w = 3.2 \text{ mm}$ and 250 mW which corresponds to a maximum trap depth of $163 \mu\text{K}$. Due to the reflection of the mirror the a standing wave is formed, which has a maximum depth of $652 \mu\text{K}$. Compared to the heating of the fluorescence imaging, the trap depth is only about twelve times as big as the heating corresponding to the detection of a single photon. In addition to the heating the illumination beam also exerts light pressure onto the atoms. This becomes visible in the fluorescence imaging where there are tails of un-trapped atoms pointing away from the illumination source, see Fig. 10.3 and Fig. 10.4.

The various patterns have different sizes, the three stripes have a size of 260 pixel times 260 pixel on the DMD, in the strapping plane it has a size of $62.4 \mu\text{m}$ times $62.4 \mu\text{m}$. The star and the phi are of similar dimension.

The structure of the trapping pattern is well observable in the fluorescence image of the captured atoms, but is smeared out. Effects that contribute to it are are the following: The trapping beam is retro-reflected off the mirror surface and hence the intensity distribution is not exactly the one anticipated in the trapping plane. The laser beam which illuminates the DMD is not homogeneous, hence it alters the trap depth across the trapping pattern, which distorts the trapping geometry. Furthermore the illumination beam has an effective diameter of $225 \mu\text{m}$ which in combination with the depth of field of the imaging system leads to blurring, as the camera integrates over many standing wave anti-nodes, which are not in the primary

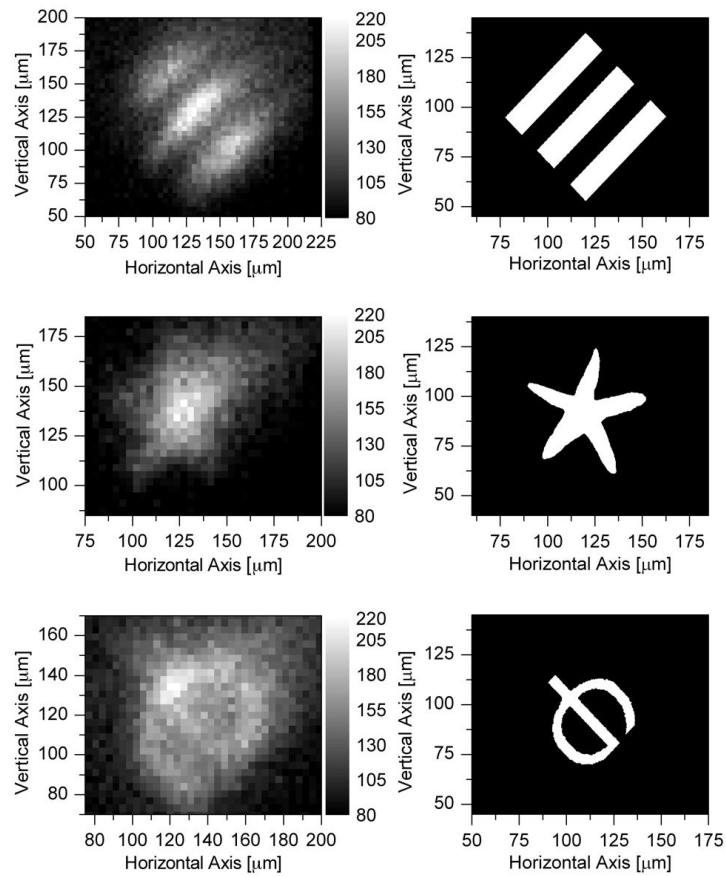


Figure 10.4 On the left hand side there are fluorescence images of trapped atoms. The trap pattern is shown on the right hand side. The stripes have a dimension of 260 pixel by 260 pixel. The star has a diameter of 310 pixel and the phi has a diameter of 190 pixel.

trapping plane.

10.3 Summary

These images of the atomic clouds show that the optical tweezers are capable of generating arbitrary trap shapes and trapping atoms in them. The measurements shown in this thesis are proof of principle and not yet characterised in terms of

temperature and atom number. Currently Cecilia Muldoon is carrying out further work to reduce the individual trap sizes and to characterise the traps. Nevertheless the data presented in this chapter shows that the optical tweezers are a flexible method to create arbitrarily shaped potential landscapes and to trap atoms within them.

Chapter 11

A High-Power Laser Diode for Dipole Trapping

In the preceding chapters I investigated the concept and experimental realisation of optical tweezers. It turned out that there are strong requirements for the trapping laser: the spatial intensity profile has to be smooth, the laser wavelength at about 785 nm or 805-815 nm with a high power output to obtain a deep dipole trap. An obvious candidate is a Titanium-Sapphire laser, which fulfils all the above requirements. The drawback of this laser-system is that it is very expensive. In this chapter I will investigate an alternative laser source: a high power multimode diode laser module.

These devices are normally used to pump solid state laser systems. Hence they have high output power, but suffer from bad beam quality and a spectral multi mode structure. The spectral multi-mode structure can lead to fluctuations in the trap

depth, but this is only of concern for ultra-cold temperatures, i.e. Bose Einstein Condensation. For low temperatures, e.g. atoms loaded from a MOT, the heating effects are less severe. The spatial profile, however, is disadvantageous for the tweezers. A possible remedy would be to use a diffuser to smear out the profile of the laser. This would not make the profile single mode, but since it would be randomly scrambled it would exhibit a smooth intensity distribution. In this chapter I will analyse the application of optical diffusers in atom trapping.

11.1 The High-Power Laser Diode Module

The laser used for the experiment is an Eagleyard EYP-BAL-0808-700-4020-CDL02-0000 laser. It is a high power diode laser, up to 7 W at 815 nm, and is commonly used for pumping solid state laser systems. The laser was driven by a remote controlled programmable linear regulated power supply (Elektro-Automatik EA/PS 3032/10B).

The laser is mounted on a home made pedestal with an integrated Peltier element (HPE-128/10/05 from Multicomp), to regulate the temperature of the laser head. The laser head has a built in NTC resistor to monitor its temperature. To keep the temperature within tolerable limits, it is sufficient to drive the Peltier element with a constant current. The application of far off-resonant dipole trapping does not require a precise frequency stability and hence high temperature stability. A slight variation in temperature has only a slight effect on the laser wavelength and consequently little effect on the trap depth. For example at 815 nm a variation of

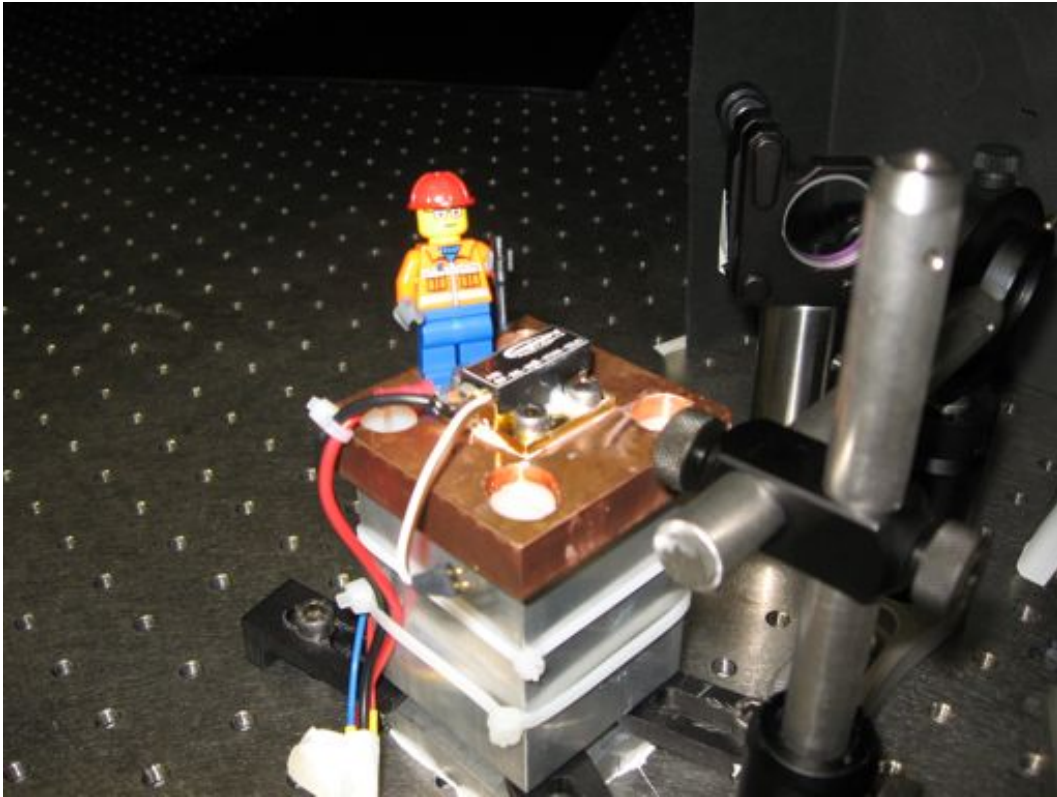


Figure 11.1 Picture of the laser head, mounted on the laser table.

2.5° leads to a variation of roughly 1 nm which corresponds to a change in trapping potential of roughly 5%. This would only be caused by a long time drift effect and is acceptable for most trapping experiments.

In this section I characterise this laser system by measuring the beam profile, the wavelength, and the power output. I measured the beam profile, by moving a $200\ \mu\text{m}$ pinhole on a translation stage through the laser beam and measuring the power of the transmitted light with a power meter (Thorlabs PM30 with a S130A head). Two sets of measurement were taken: one with the pinhole at a distance of 20 cm from the laser, and one at a distance of 40 cm. For each distance I measured

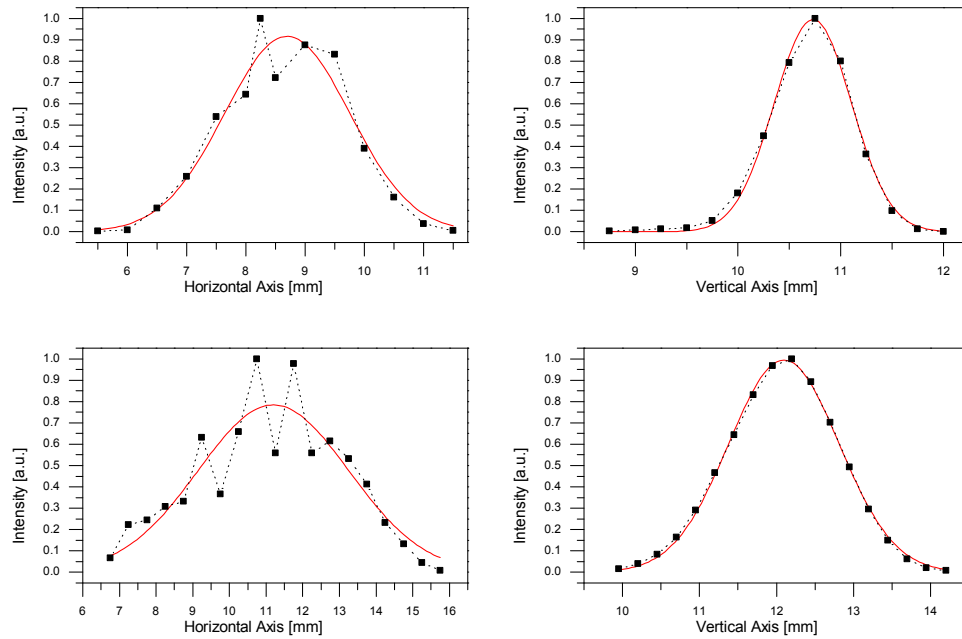


Figure 11.2 Profile of the laser at a distance of 20 cm from the laser (top row) and a distance of 40 cm (bottom row). The left column show the horizontal cut through the laser and the right column shows the vertical cut. The vertical cuts show a nice Gaussian intensity distribution, whereas the horizontal cut exhibits a strong modulation of the Gaussian intensity distribution.

a cut along the x-axis and y-axis through the centre of the profile. The recorded data was fitted with a Gaussian profile ($\sim e^{-2(\frac{x}{w})^2}$, where w is the width of the profile) to determine the beam widths, see Fig. 11.2. These are summarised in the following table. The printed angle is the full opening angle with respect to the full beam width. i.e. from $-w$ to $+w$ which corresponds to 1.7 times the FWHM. I will keep this definition throughout the whole chapter. These results coincide with the data sheet of the laser system.

cut orientation	distance [mm]	beam width w [mm]	opening angle [°]
horizontal	200	2.11	1.21
vertical	200	0.75	0.43
horizontal	400	4.12	1.18
vertical	400	1.43	0.41

For the purpose of energy propagation, for the horizontal and the vertical axis for optical path lengths greater than 20 cm, the laser beam can be modelled as a gaussian beam with two opening angles.

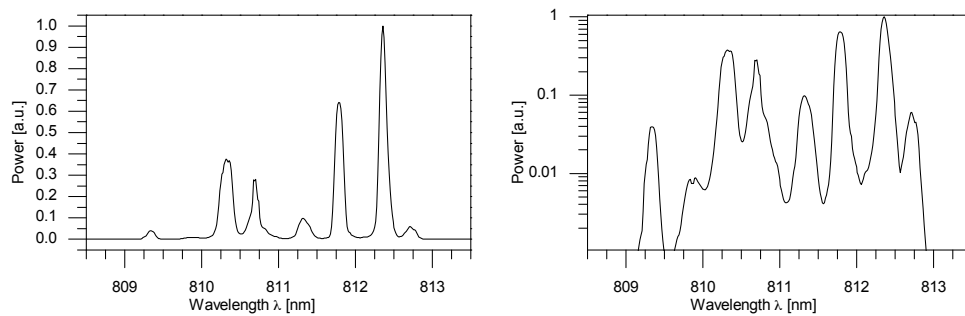


Figure 11.3 Spectrum of the emitted laser radiation in linear (left) and logarithmic (right) representation. The baseline of 0.001 a.u. in the logarithmic plot represents the detection threshold of the optical spectrum analyser.

Next I determined the wavelength at which the laser emits with a spectrum analyser (Ando AQ6317B), which has a dynamical range of 30 dB. The laser emission consists of multiple peaks which each have a line width of roughly 0.1 nm each and are separated by multiples of 0.34 nm. The spectrum was taken at 18 °C and it shows a temperature dependence of about 0.4 nm/K according to the manufacturer.

Last I measured the power output with a power meter (Coherent Fieldmate with

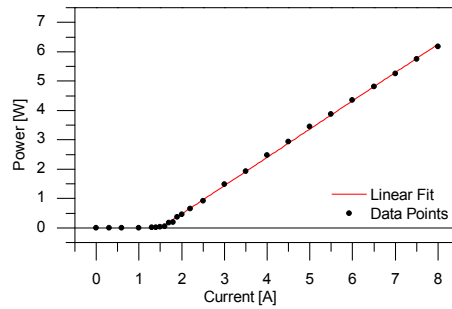


Figure 11.4 Output power of the laser depending on the supply current.

a PM10 head). The output power with respect to the driving current is shown in Fig. 11.4. The laser threshold is at 1.51 A and at a maximum driving current of 8 A the output is 6.18 W.

This diode laser is remarkable since it has a high power output, requires only minimal effort to operate and is very inexpensive compared to other laser systems. The drawbacks are its bad optical profile and the multimode operation.

11.2 Trap Depth of a focused Beam

In this section I investigate if the laser diode module can be used to directly form a dipole trap. The simplest way to achieve this, as I will discuss here, is to simply focus the beam with a single lens. As a first approach this can be modelled as imaging the exit facet of the laser diode onto the trapping plane. The lensmaker's equation $\frac{1}{f} = \frac{1}{l_i} + \frac{1}{l_i}$ relates the position of the focal point l_i with the position of the

light source l_l and the focal lens of the lens f . It can be rearranged into the form:

$$l_i = \frac{f \cdot l_l}{l_l - f}. \quad (11.1)$$

The demagnification of the imaging is given by the ratio:

$$M = \frac{f}{l_l - f}. \quad (11.2)$$

In order for the $D=25$ mm imaging lens to capture most of the radiation, the lens has to be located not farther than one meter from the laser, otherwise the beam diameter will be larger than the lens diameter. A $f = 100$ mm lens was used. $l_l = 1.5$ m results in $M = 1/14$. For an initial beam size of 3 mm by 0.5 mm a size of $261 \mu\text{m}$ by $36 \mu\text{m}$ should be obtained.

11.2.1 Characterisation of the focussed Beam

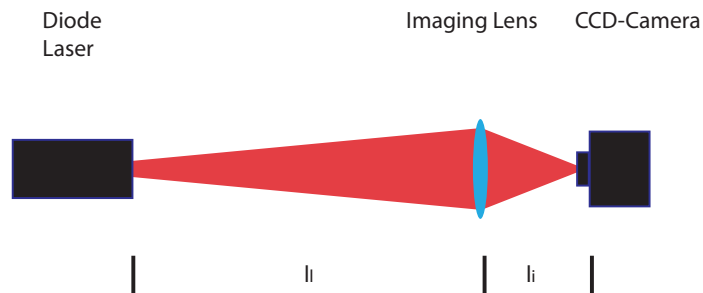


Figure 11.5 Scheme of the imaging set up.

The characterisation of the focussed beam was done with the setup depicted

in Fig. 11.5. A lens with focal length $f = 100$ mm and a diameter $D = 25$ mm was placed 1000 mm behind the high power diode laser. A CCD-camera (Imaging Source DMK 21BF04) was positioned on a translation stage, so that it could be moved along the optical axis. Neutral density filter was placed behind the laser to prevent the CCD-camera from saturating, while the laser was operating above the threshold. The picture that the camera took in the focal plane is displayed in Fig. 11.6.

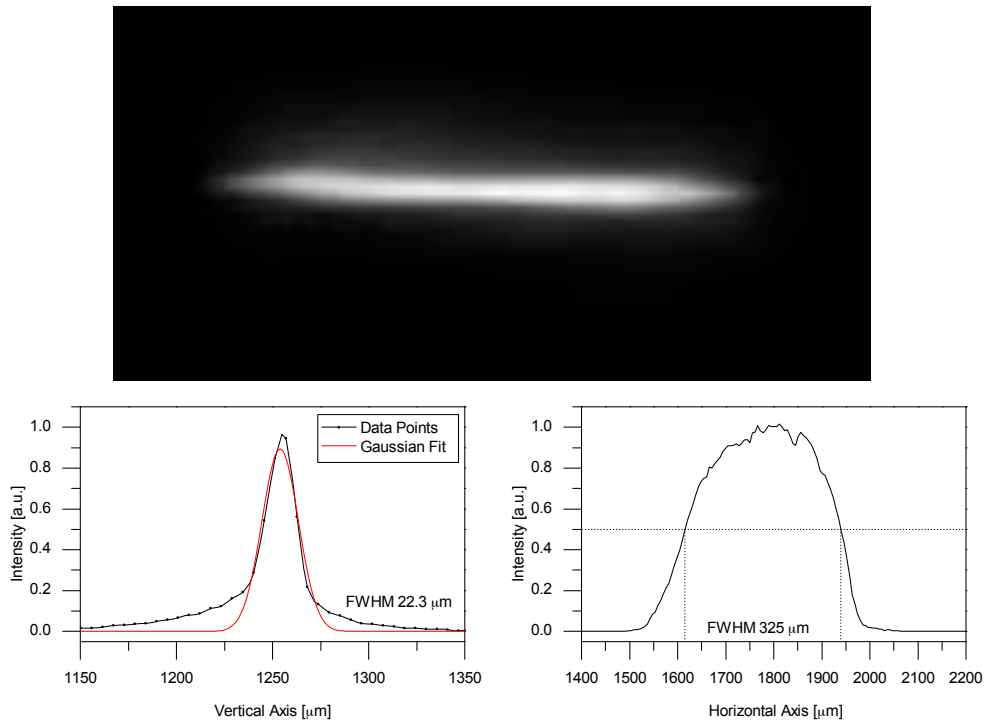


Figure 11.6 Picture of the beam focus(top). Cross-sections through the intensity profile in the focal-plane(bottom).

The measured intensity distribution in the image plane has a FWHM of $325 \mu\text{m}$ along the horizontal axis and of $22.3 \mu\text{m}$ along the vertical axis, see Fig. 11.6. The resulting trap depth is $325 \mu\text{K}$, which is deep enough to efficiently load atoms from

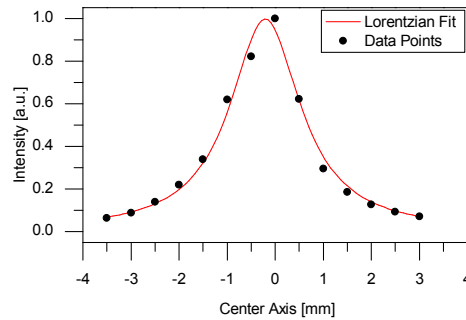


Figure 11.7 Peak intensity along the z-axis of the trap, which is defined by the propagation direction of the trapping light.

the MOT.

To measure the trap depth along the beam I moved the camera along the optical axis (z-axis) and took images of the intensity. I fitted the resulting maximum intensity with a Lorentzian, see Fig. 11.7 and found the FWHM to be 1.79 mm. These values look promising with respect to applying this technique as a dipole trap to trap atoms. However in the focal plane the beam does not exhibit an intensity distribution which is close to a Gaussian distribution, which is required for the application of the optical tweezers.

11.3 The optical Diffuser

An optical diffuser smooths out the profile of a given beam profile in the far field of the diffuser. By placing a collimating lens behind the diffuser, the far field lies one focal length behind the collimating lens.

The diffuser also increases the divergence of the beam. It consists of randomly

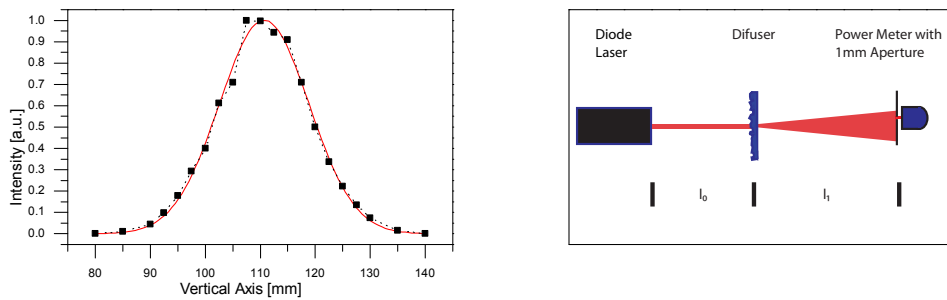


Figure 11.8 Cross-section of the laser beam 20cm after the diffuser and the measurement set up.

distributed micro lenses, which divert the incoming light. When a large enough area of the diffuser is illuminated the light is homogeneously distributed over a solid angle depending on the type of diffuser. This distribution property will be investigated to determine the opening angle. When the diffuser is illuminated with coherent light the pattern will actually show a diffraction pattern, which will be visible on small scales.

I measured the divergence by illuminating the diffuser, according to Fig. 11.8, with a distance of $l_0 = 20$ cm between the laser and the diffuser; and used a power meter with a 1 mm aperture at a distance $l_1 = 20$ cm behind the diffuser. The power meter was moved horizontally through the centre of the expanding beam. The recorded data was then fitted with to Gaussian profile with a beam width of 16.34 mm. The finite size of the laser beam and of the aperture has to be taken into account and results in a width of 15.81 mm. This corresponds to a full divergence angle of 9.1° .

11.4 The Application of the Diffuser

The optical tweezers are designed to transport atoms over some distance. To avoid heating of the atoms the change of potential should be smooth. This requires that the illumination light, which shapes the illumination of the DMD pattern and thus the trapping potential, should be as smooth as well. Clearly that is not the case for the profile of the high power diode laser, but this is where the optical diffuser comes into play.

The model setup for the optical tweezers including the diffuser is shown in Fig. 11.9. To simulate the DMD an iris aperture is placed in the setup. The high power diode laser illuminates the diffuser and the collimating lens situated behind the diffuser creates the far field of the diffuser at a distance of one focal length with respect to the collimator. In this plane the iris aperture is placed, which is then imaged with another lens, the imaging lens, to form the trapping potential.

The optical tweezers should be sufficiently deep to trap atoms. This requires achieving a high demagnification of the DMD image, while keeping the diameter of the beam small enough to avoid clipping losses through the optical elements. This problem will be analysed in the following subsections.

11.4.1 Initial Conditions

The optimisation of the trapping setup depends on various parameters: I will treat the distances $l_0 - l_4$ as well as the focal length f_{coll} and f_{im} as variables which can be chosen freely. l_0 determines the spot size. This should be treated as fixed here,

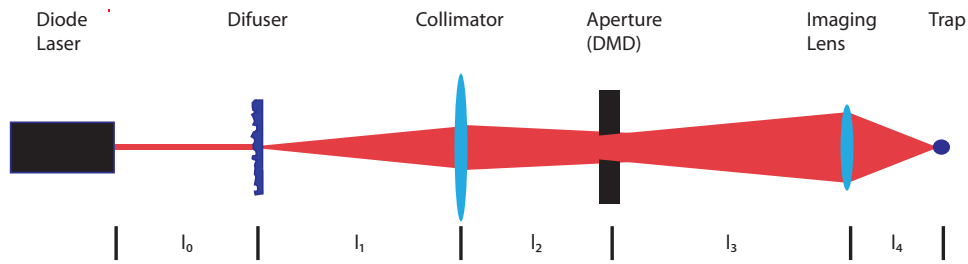


Figure 11.9 Scheme of the model setup for the optical tweezers including the high power diode laser module and the diffuser. The high-power laser beam passes through the diffuser and the far field of the diffused radiation is established by the collimator lens one focal length behind it. In this plane an iris aperture is placed to simulate the DMD. It is imaged by the imaging lens to form the trap.

since it largely depends on experimental convenience. Therefore the determination of the remaining variables can be thought of as an optimisation problem. There are some physical and technical constraints and relations which have to be taken into account:

- The diffuser smooths out the profile in the far field. Behind a lens the far field is formed exactly one focal length behind the lens. Therefore l_2 is given by the focal length of the collimator.

$$l_2 = f_{col} \quad (11.3)$$

- The DMD has to be imaged by the imaging lens. The magnification M of this imaging is given by the ratio of l_3 and l_4 .

$$M = \frac{l_3}{l_4} \quad (11.4)$$

The lens makers equation also relates l_3 to l_4 :

$$\frac{1}{f_{im}} = \frac{1}{l_3} + \frac{1}{l_4} \quad (11.5)$$

- The total angle $\alpha_{tot} = \sqrt{\alpha_{dif}^2 + \alpha_{laser}^2}$ -which is the geometrical sum of the diffusion angle α_{dif} and the divergence angle of the the laser α_{laser} -determines to the size in the far field of the collimator d_{ff} of a point source.

$$d_{ff} = 2f_{col} \tan(\alpha_{tot}/2) \quad (11.6)$$

- In order to get the maximum power through the imaging lens the collimator has to image the surface of the diffuser onto the imaging lens.

$$1/f_{col} = 1/l_1 + 1/(l_2 + l_3) \quad (11.7)$$

11.4.2 The Optimisation Problem

With the relations from the previous subsection l_1, l_2, l_4 can be expressed as functions of l_3, f_{coll} and f_{asp} . Furthermore the diameters of the optical elements are limited, so the design should aim to maximise the energy propagating through the elements. Let me state the new formulas first: Eq. (11.7) together with Eq. (11.3) gives the following equation:

$$\frac{1}{l_1} = \frac{1}{f_{col}} - \frac{1}{l_3 + f_{col}} \quad (11.8)$$

This equates to:

$$l_1 = \frac{f_{col}(f_{col} + l_3)}{l_3} \quad (11.9)$$

Eq. (11.5) equates to:

$$l_4 = \frac{l_3 \cdot f_{im}}{l_3 - f_{im}} \quad (11.10)$$

Now the next step is to calculate the diameter of the intensity distributions on the optical elements. First of all the spot size of the illuminating laser on the diffuser d_{dif} is given by the beam divergence of the laser α_l , the initial size of the laser d_l as well as the distance to the laser l_0 .

$$\tilde{d}_{dif} = 2l_0 \tan(\alpha_l/2) \quad (11.11)$$

Together with the initial size on the at the laser d_l this leads to the total spot size on the diffuser:

$$d_{dif} = \sqrt{\tilde{d}_{dif}^2 + d_l^2} \quad (11.12)$$

The size of this beam on the collimator is a combination of the beam spread after the diffuser:

$$\tilde{d}_{col} = 2l_1 \tan(\alpha_{tot}/2) \quad (11.13)$$

and the spot size on the diffuser d_{dif} :

$$d_{col} = \sqrt{\tilde{d}_{col}^2 + d_{dif}^2} \quad (11.14)$$

This then propagates according to Eq. (11.6). The size on the imaging lens is given by the imaging law:

$$d_{im} = d_{dif} \left(\frac{f_{col} + l_3}{l_1} \right) \quad (11.15)$$

Together with (11.9):

$$d_{im} = d_{dif} \frac{l_3}{f_{col}} \quad (11.16)$$

The size of the trap is finally given by the following expression:

$$d_{trap} = d_{ff} \frac{l_4}{l_3} \quad (11.17)$$

Together with Eq. (11.10):

$$d_{trap} = d_{ff} \frac{f_{im}}{l_3 - f_{im}}, \quad (11.18)$$

and (11.6) this leads to:

$$d_{trap} = 2 \tan(\alpha_{tot}/2) \frac{f_{col} \cdot f_{im}}{l_3 - f_{im}} \quad (11.19)$$

With this last equation we have now all the relevant equations to go on and choose the parameters to minimise the trap diameter.

11.4.3 Solving the Optimisation Problem

To maximise the trap depth the trapping area has to be minimised. For a fixed total divergence angle α_{tot} , this requires $l_3 \gg f_{im}$ and $l_3 \gg (f_{col} \cdot f_{im})$ according to Eq. (11.19). In fact this equation implies that for $d_{trap} \rightarrow 0$ for $l_3/f_{im} \rightarrow \infty$ and

$l_3/(f_{col} \cdot f_{im}) \rightarrow \infty$, but some technical constrains apply: at the points wherever the beam propagates through an optical element, its diameter has to be smaller than the diameter of the optical element. Furthermore the imaging lens can not have a focal length less than $f = 20$ mm if mounted inside the vacuum chamber and $f = 75$ mm if mounted outside the vacuum chamber.

The diameter of the imaging lens D_{im} (I introduce the convention that large D indicate the diameter of optical elements, whereas small d denote the beam diameter) has to be larger than the beam diameter at the imaging lens d_{im} , which is given by Eq. (11.16). Hence $D_{im} > d_{dif} \frac{l_3}{f_{col}}$, this give the ratio:

$$\frac{l_3}{f_{col}} < \frac{D_{im}}{d_{dif}} \quad (11.20)$$

This relation inserted into the expression for the trapp diameter Eq.(11.19) and assuming $l_3 \gg f_{im}$ one obtains:

$$d_{trap} > 2 \tan\left(\frac{\alpha_{tot}}{2}\right) d_{dif} \frac{f_{im}}{D_{im}} \quad (11.21)$$

This equation states that the trap diameter is determined by the spot size on the diffuser d_{dif} , the total divergence angle α_{tot} , and by the f-number of the imaging lens $N_{im} = \frac{f_{im}}{d_{im}}$.

To obtain a deep and hence small trap, the total diffusion angle α_{tot} has to be as small as possible, i.e. the diffuser should be chosen, so that its diffusion angle α_{dif} is as small as possible, but big enough to smooth out the laser profile. The

spot size on the diffuser should also be as small as possible, but big enough so that enough area of the diffuser is illuminated to average over many micro lenses. Finally the F-number of the imaging lens should be as small as possible, but commercially available ones are limited to $N \approx 1$. For example lens configuration see section 11.6.

Furthermore the parameters of the collimating lens are restricted as well, but this does not impose any severe restrictions, as is shown in the appendix F.

11.5 The experimental Check of the Setup

11.5.1 The stationary Diffuser

In this section I will experimentally investigate the scheme which has been theoretically treated in the previous section. A CCD-camera (The Imaging Source DMK 21BF04) is placed in the trapping plane to measure the light intensity of the trap. Neutral density filters in front of the diffuser reduce the light intensity sufficiently to not saturate the camera while the laser is still operating above the laser threshold. The iris is set to a diameter of 15 mm to simulate the spatial light modulator.

The images in Fig. 11.10 are produced according to the scheme Fig. 11.9, where the distances are as following: $l_0 = 30$ cm, $l_1 = 35$ cm, $l_3 = 165$ cm and l_4 is adjusted to that that the iris aperture is imaged clearly. The collimator is a $f_{col} = 200$ mm lens with $D_{col} = 25$ mm diameter. The imaging lens has a focal length of $f_{im} = 75$ mm and a diameter of $D_{im} = 25$ mm. The picture displayed on the left hand side was taken with stationary diffuser. Underneath a fit through the centre is displayed. It

is obvious that this picture exhibits strong intensity fluctuation. These fluctuations are caused by the random nature of the diffuser, which results in a random length of each optical path combining at one point on the camera. This results in random interference and hence fluctuation in the intensity.

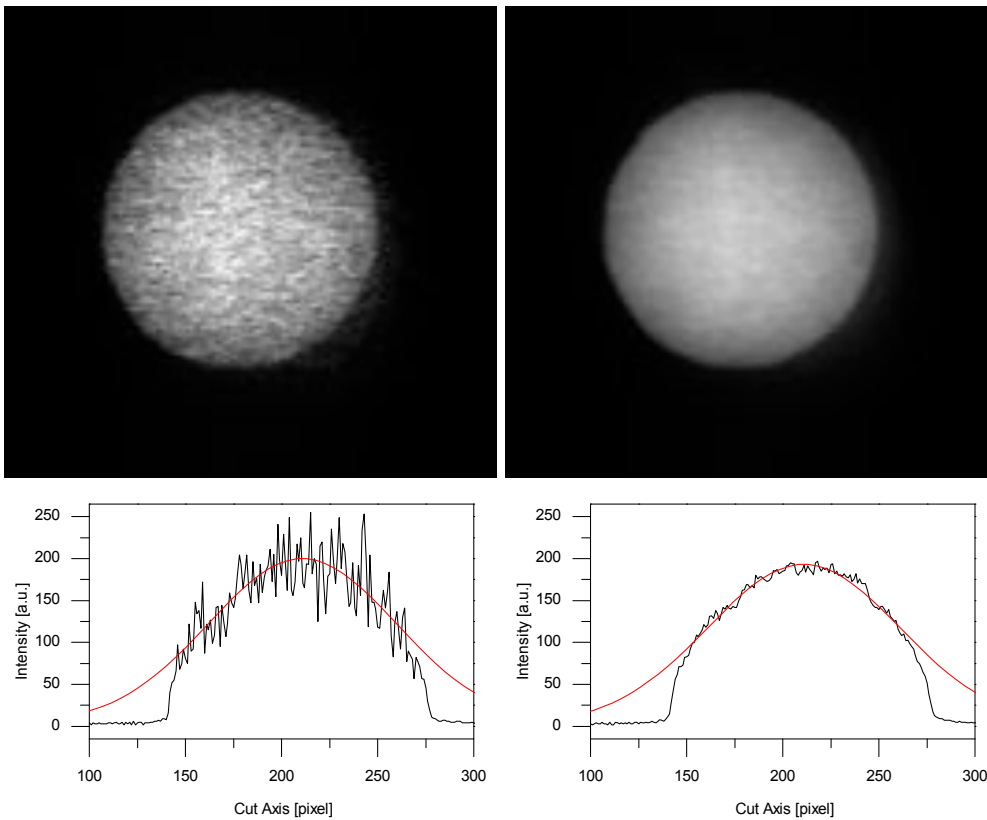


Figure 11.10 Top: Intensity distribution in the image plane of the far field of the diffuser for a non-rotating and rotating diffuser left and right respectively. Bottom: Cut through the centre of the above pictures. The intensity distribution is fitted with a gaussian peak.

11.5.2 The rotating Diffuser

To avoid the random speckle pattern one could average over multiple speckle patterns to smooth it out. A different speckle pattern can be simple obtained by laterally displacing the diffuser with respect to the beam. This has to be done on a time scale much faster than the trapped atoms can follow the changing trapping landscape. The trapping frequency, which defines the relevant time scale for atoms trapped in the potential, is on the order of 1 kHz. Therefore the averaging has to be done well below 1 ms. To achieve that I mount a disk diffuser of 100 mm diameter onto a electric motor. This motor is able to rotate with rates up to 100 Hz. Above 70 Hz the disk starts to flutter, hence I restrict the motor to 60 Hz for the experiments. With the diameter of the disk of 100 mm the speed of the diffuser at the edge is 18.9 m/s. This configuration proves capable to sufficiently smooth over a profile at a timescale of 0.1 ms, see Fig. 11.10 left, the shortest exposure time of the ccd-camera.

The cross sections show that the picture taken with the diffuser rotating at 60Hz with an exposer time of $1/10.000$ sec is much smoother than the picture with the diffuser not moving. With respect to the fit the root mean square error is 6.1 a.u. and 29.1 a.u. for the rotating and stationary diffuser respectively. The error which is caused by the interference within the pattern is probably even smaller, because effects like camera read-out noise add to the noise as well.

The investigation of the speckle pattern has been limited by 3 factors: 1. The readout of the CCD-camera exhibits some intrinsic noise, which seems to be the dominating contribution in the averaged picture. Therefore a lower noise would be

desirable to characterise the system. 2. The shortest exposer time of the camera is $1/10.000$ s. To see fluctuations on a shorter time-scale a corresponding shorter exposer-time is required. 3. The pixel size is 5.6 mm by 5.6 mm. This is almost an order of maximum larger than the wavelength of the laser radiation. It would be important to see how the fluctuation behave on a smaller scale, since spatially small fluctuations lead to steep gradients and therefore can exert strong forces on the trapped atoms.

So far I have investigated the behaviour of the laser radiation in the image plane of the imaging lens. In the following I will investigate how the profile of the laser radiation looks outside the image plane. This is important since the point of highest intensity determines the centre of the trap along the optical axis. Unfortunately it turns out that it is in fact slightly displaced from the image plane. This effect arises because the object is at a finite distance in front of the imaging lens, hence the image is formed behind the focal point. This focussing effect becomes stronger as the size of the object increases. Furthermore the variation of intensity along the trap depth determines the confinement of the trap as well.

Again the setup according the scheme Fig. 11.9 is used, where the distances are chosen as following: $l_0 = 20$ cm, $l_1 = 35$ cm, $l_3 = 165$ cm. The collimator is a $f_{col} = 200$ mm lens with $D_{col} = 25$ mm diameter. The imaging lens has a focal length of 75 mm and a diameter of 25 mm. The only difference is that now a aperture with a 10 mm diameter is used. I took a series of pictures with various displacements with respect to the image plane.

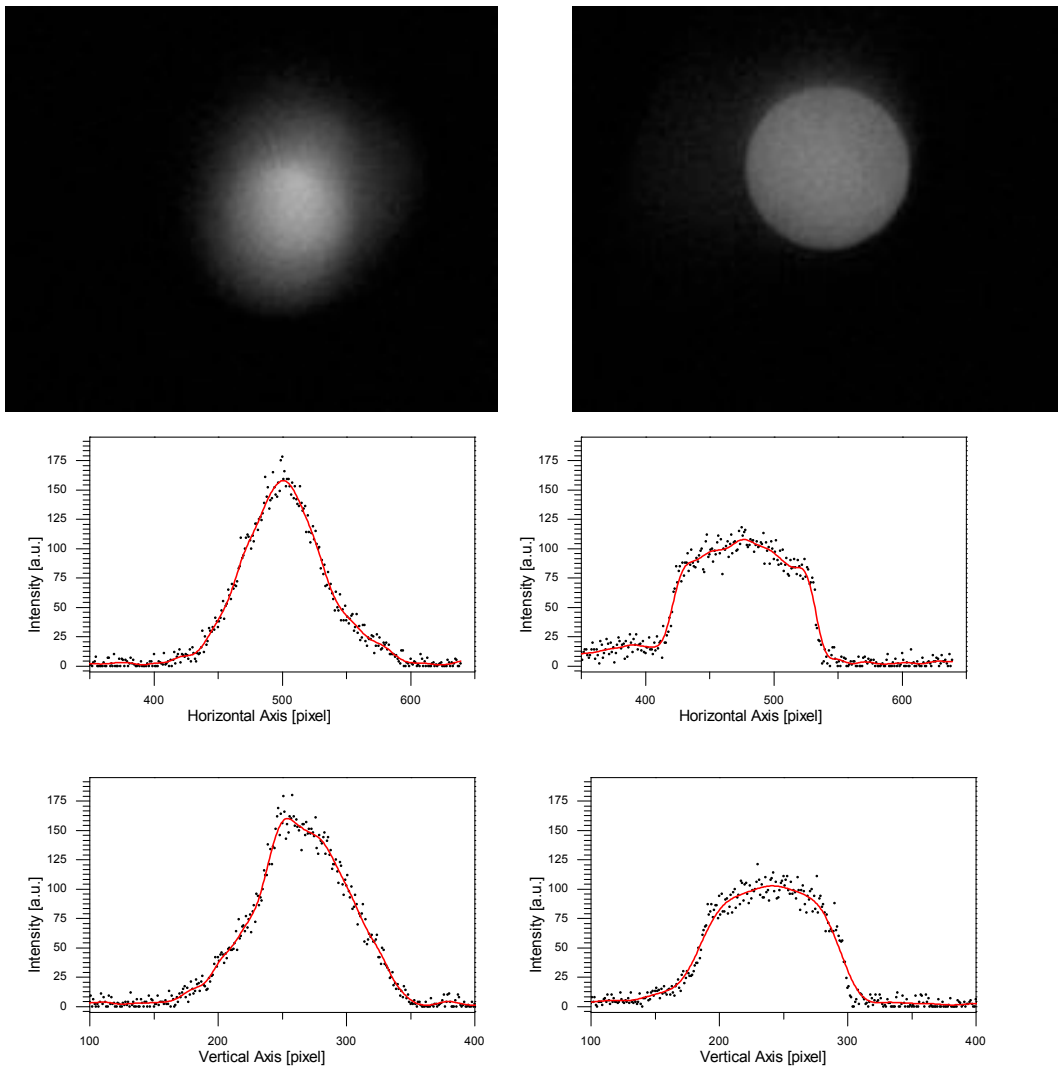


Figure 11.11 Image of an aperture, which is in the far field of the diffuser, taken with a camera. The left picture is 3 mm in front of the image plane and the right one is in the image plane. Below are cuts through the images. In the image plane the light intensity is fairly homogenous, whereas out of the focal plane the intensity distribution is as anticipated rather inhomogeneous, but the highest intensity is larger than in the case where the camera is in the image plane. This effect arises because the object is at a finite distance from the imaging lens.

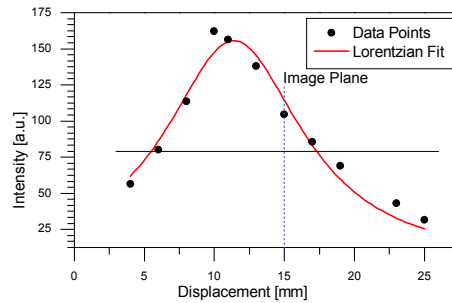


Figure 11.12 Measured trap depth for various displacements. Here 15 mm corresponds to the image plane. The graph shows that around the centre position the figure behaves well like a Lorentzian curve with a full width half maximum of 12 mm.

Two pictures of important planes are shown in Fig. 11.12. The intensity distribution is as expected in the image plane. But it turns out that in a plane 3 mm in front of the image plane the intensity is much higher, than in the centre of the image plane, see also the cuts through the planes in Fig. 11.11.

I have taken a series of images of different planes along the axis and plotted the highest intensity per image in Fig. 11.12. The graph shows that that the FWHM in of intensity along the z-axis is 12 mm. The confinement along the x- and y-axis is about a factor 20 tighter. This intensity profile depends strongly on the mask which is used to block radiation in the image plane. So with a different configuration much higher confinement seems possible.

Taking the previous results together it seems possible to create a dipole trap with this technique provided that the trap can be made deep enough. This will be theoretically investigated in the next section, by applying the numbers found in this section with the formulas derived in the previous section.

11.6 Feasibility Study

To determine if the setup described in the previous section produces a trap deep enough to capture atoms, I will calculate the trap depth for 3 different imaging lenses. The parameters that cannot be changed are the available laser power $P_L = 6$ W at a wavelength $\lambda_L = 815$ nm, the full divergence angle after the diffuser $\alpha_{tot} = 9.1^\circ$ and the spot size on the diffuser $d_{dif} = 2.1$ mm at a distance of $l_0 = 20$ cm from the diode laser.

I choose a collimating lens with $f_{coll} = 200$ mm. According to (11.12) this gives a spot size of $d_{dif-h} = 6.03$ mm by $d_{dif-v} = 2.15$ mm. I calculate the parameters for 3 lenses with focal lengths of: 20 mm, 75 mm, and 100 mm, all with a diameter of $D_{im} = 25$ mm. The first lens would be an aspherical lens, whereas the other two can be standard semi-spherical ones. The aspheric lens needs to be placed inside the vacuum chamber, whereas the other two could be located outside.

With Eq. (F.3) this results in a value of $l_3 = 2380$ mm. Eq. (11.9) fixes $l_1 = 216.8$ mm. This leads to a size of the far field of $d_{ff} = 31.8$ mm. This is a useful value since the set up is to be used in conjunction with a spatial light modulator which has in turn a digonal of about 18 mm, so the central beam illuminates the DMD nearly homogeniously.

The value which is left to be determined is the distance l_4 , which defines the magnification M_{im} between the far field and the trap as well as the trap diameter d_{trap} . This value depends on f_{col} . The power of the laser beam P_r is reduced to the assumed losses of 10% at the diffuser and a loss of 5% due to the limited aperture

of the imaging lens. From this value the trap depth is derived with Eq. 2.12. The results are summarised in the following table.

To calculate the trap depth in the image plane the peak intensity given by the formula $I_p = \frac{2P_r}{\pi\omega^2}$, where ω is the width as calculated as the diameter in the trap and

f_{im} [mm]	l_4 [mm]	M_{im}	d_{trap} [mm]	U_{trap} [μ K]
20	20.17	0.0085	0.121	192.5
75	77.44	0.0325	0.466	13.0
100	104.4	0.0434	0.628	7.2

The values for the trap depth are to be compared with the temperature of cold atoms in a magneto optical trap, which are on the order of several hundred μ K. So the configurations with the 75 mm and 100 mm will not produce a trap which is deep enough to capture a significant number of atoms. Only the configuration with the 20 mm lens seems to be promising to capture atoms.

11.7 Outlook

To conclude the feasibility study of the high power laser in combination with the diffuser seems to be a very promising way of trapping atoms. It will not work with the current components investigated, but it seems very likely that it is possible to achieve the trapping with a specially designed set up. There are numerous possibilities to increase the trap depth:

- A laser diode which lases at 805 nm can be used. This improves the trap depth by about 30% compared to the current laser.
- The $f_{im} = 75$ mm and $f_{im} = 100$ mm lenses can be replaced with some higher numerical aperture lenses.
- Multiple laser sources can be used to increase the available power.
- A diffuser with a smaller opening angle could reduce the divergence of the laser beam and hence reduce the diameter of the trap size.

Out of these it seems to be crucial to use a lens with a high numerical aperture preferable an aspheric lens. Though the light will be strongly collimated, the thick viewport will result in aberrations. Hence the optical quality of the set-up can be greatly increased if the lens is placed inside the vacuum chamber. A diffuser with a smaller opening angle will result in a less divergent beam and hence the setup will be able to produce a smaller trap size and hence a deeper trap. With these two measures it looks very promising to generate traps, which are deep enough to successfully trap atoms pre-cooled in the magneto-optical-trap.

The diffuser leads to a microscopic fluctuation of the light in the trapping plane, due to the random phases acquired in the diffuser. These fluctuations can be averaged by spinning the diffuser. This is an averaging in time, hence it is important to average faster than the atoms can follow the fluctuations of the potential. To test whether this effect has an impact can only be done experimentally, by loading atoms into the tweezers and observe the life time of the trapped atoms.

To summarise if a configuration can be implemented with a deep enough trap depth and the intensity fluctuations do not lead to a high heating rate, the application of the high power dipole laser in combination with a diffuser seems to be a very promising alternative to the costly solid state laser systems.

Chapter 12

Conclusion

12.1 Summary

The subject of this thesis are the optical tweezers for the trapping and manipulation of single atoms in real time. So far first proof of principle results are presented, which show that the tweezers can produce arbitrary trap geometries and trap atoms therein. This is an very significant milestone towards the single atom tweezers.

The work described in this thesis started from scratch, i.e. from an empty lab, hence the first step was to set up the laser lab. To realise the Magneto-Optical-Surface-Trap, the u-shaped wire had to be designed first, then the laser systems, the optics as well as all the vacuum technology had to be set up. As a test of the DLX-laser system atoms were loaded from the MOST into a dipole trap, just formed by focussing the laser beam. While testing the aspherical lens, which is used to image the DMD, the image degradation due to the non-isoplanatic was

discovered, but this degradation can be avoided by convergent illumination. With this problem eliminated it was possible to generate the tweezers and trap atoms with them. Various trapping geometries have been generated and used to capture atoms therein. Those atoms have been observed with absorption and fluorescence imaging. The optical tweezers have proven to be versatile, since they can generate potential landscape beyond what can be archived with simple gaussian beam and to trap atoms therein.

Additionally I investigate the use of a high power diode laser to be used as a source for the trapping light. It turned out that the divergence was too large and the numerical aperture of the used lenses too small to generate traps which are deep enough to trap atoms. But these shortcomings are only technical and not fundamental in nature, hence it should be possible to apply this technique to atom trapping. Though it still has to be determined if the micro-intensity-fluctuation can be overcome by fast rotation of the diffuser and if the resulting heating rate is within tolerable limits. Then this method would be a rather affordable alternative to expensive solid state laser systems.

12.2 Outlook

So far I have presented some first images of atoms trapped in arbitrarily shaped traps. These are proof of principle results and the characterisation and improvement of the tweezers is currently ongoing. The next issues to tackle are:

- The reduction of the trap size, will reduce the effect for multiple trapping lay-

ers, since with a reduction of the Rayleigh length the forming partial standing lens will be less pronounced and the tweezers will act more like running wave traps. Furthermore it should be possible to reduce the atom number in this way.

- The fluorescence imaging can be improved by changing the illumination from a focussed beam to a light sheet. The light sheet is generated by focussing the illumination light with a cylindrical lens. A width of $10\ \mu\text{m}$ can be easily achieved, hence only about 20 layers of the partly standing wave are illuminated. By retro-reflecting the light-sheet the light pressure can be eliminated to avoid the atoms are being pushed out of the trap.
- The optical tweezer can be operated dynamically, by changing the trapping potential whilst the atoms are trapped therein, which enables the transport of atoms. This should lead to interesting experiments fully exploiting the potential of the optical tweezers.

In the long run it would be advantageous to reduce the trap to a single layer 2-dimensional system. For example a trapping light sheet can confine the atoms to a plane, while the tweezers are moving them within the plane. This scheme would work without the mirror in the vacuum chamber. Alternatively more involved surface traps using evanescence fields could be used^[18,82]. During the imaging the atoms are heated by the illumination beam, to counter this the atoms could be actively cooled while being in the trap^[83]. This would enable a continuous observation

of the atoms. With improved imaging it seems feasible to observe single atoms. Light assisted collision reduce the atom number to 0 or 1 in small traps with high fidelity^[71,84] combined with post-selection this method should be suitable to deliver single atoms on demand.

With these improvements included the optical tweezers seem to offer the flexibility and precision needed to deterministically couple single atoms to optical cavities, like fibre tip cavities^[85,86], bottle neck cavities^[87–89], cavities in photonic bandgap materials^[90], toroidal cavities^[91,92], bottle cavities^[93], micro-sphere resonators^[94]. Alternatively to CEQD, Rydberg atoms^[95,96] in the tweezers can strongly interact to create entanglement between them and this can be applied to quantum information processing^[97–99]. A further alternative would be the use of controlled collisions^[100], which one could implement through a spin-selective trapping scheme^[15].

Chapter 13

List of Publications

Trace Isotope Detection Enhanced by Coherent Elimination of Power Broadening, Alvaro Peralta Conde, Lukas Brandt, and Thomas Halfmann, Phys. Rev. Lett. 97, 243004 (2006)

Towards a Scalable Dipole-Trapping Scheme for Neutral Atoms, Lukas Brandt, Cecilia Muldoon, Edouard Brainis, and Axel Kuhn, in Conference on Lasers and Electro-Optics/Quantum Electronics and Laser Science Conference and Photonic Applications Systems Technologies 2008 Technical Digest (Optical Society of America, Washington, DC, 2008), JThA105

Coherent imaging of extended objects Edouard Brainis, Cecilia Muldoon, Lukas Brandt, and Axel Kuhn, Optics Communications Volume 282, Issue 4, 15 February 2009, Pages 465-472

Optical Tweezers for manipulating Single Atoms, Lukas Brandt, Cecilia

Muldoon, Edouard Brainis, and Axel Kuhn, Conference on Lasers and Electro-Optics Europe & the European Quantum Electronics Conference (CLEO/Europe - EQEC 2009), Conference digest JSS2.1.

Implementation of Atom-Photon Interfaces for Quantum Networking,

Lukas Brandt, Cecelia Muldoon, Tobias Thiele, Jerome Dilley, Peter Nisbet, Gunnar Langfahl-Klabes, and A. Kuhn, Conference on Lasers and Electro-Optics (CLEO) and the Quantum Electronics and Laser Science Conference (QELS) (Optical Society of America, Washington, DC, 2010), QThA2.

Spatial light modulators for the manipulation of individual atoms, Lukas

Brandt, Cecilia Muldoon, Tobias Thiele, Jian Dong, Edouard Brainis, and Axel Kuhn, Appl. Phys. B 102, 443-450 (2011)

Appendix A

Supplement to Theory

A.1 Rotating Wave Approximation

In the theory chapter 2 I apply the rotating wave approximation to the atom field interaction, here I will derive it in detail. To simplify the treatment I restrict the treatment on a two level system, without considering the external degrees of freedom.

In this case the Hamilton operator can be written in matrix form:

$$\hat{H} = \begin{pmatrix} 0 & -\hat{\mathbf{d}} \cdot \mathcal{E}(t) \\ -\hat{\mathbf{d}} \cdot \mathcal{E}(t) & E_e \end{pmatrix}. \quad (\text{A.1})$$

This Hamilton operator (A.1) acts on the state vector $\psi = \begin{pmatrix} c_g(t) \\ c_e(t) \end{pmatrix}$ can be transformed with the unitary matrix

$$U = \begin{pmatrix} e^{\frac{i}{2\hbar}(E_e - \hbar\omega)t} & 0 \\ 0 & e^{\frac{i}{2\hbar}(E_e + \hbar\omega)t} \end{pmatrix} \quad (\text{A.2})$$

into the rotating frame:

$$i\hbar \frac{\partial}{\partial t} |\tilde{\psi}\rangle = \hat{H} |\tilde{\psi}\rangle \quad (\text{A.3})$$

where:

$$|\tilde{\psi}\rangle = U |\psi\rangle, \quad (\text{A.4})$$

is the rotating frame state.

$$\hat{H}_{WW} = U \hat{H} U^{-1} - i\hbar \left(\frac{\partial}{\partial t} U \right) U^{-1} \quad (\text{A.5})$$

In this picture the Hamilton Operator has the following appearance:

$$\hat{H}_{WW} = \frac{\hbar}{2} \begin{pmatrix} \Delta & \Omega^*(1 + e^{-i2\omega t}) \\ \Omega(1 + e^{+i2\omega t}) & -\Delta \end{pmatrix} \quad (\text{A.6})$$

In this picture the Rabi frequency $\Omega = \mathbf{d} \cdot \mathcal{E}(t)/\hbar$ and the detuning $\Delta = \frac{\hbar\omega - E_e}{\hbar}$ are introduced

The non-diagonal terms of this Hamilton operator (A.6) contain fast oscillating terms. In case that the Rabi frequency Ω is much smaller than the frequency of the electric field ω this interaction term averages out and can be neglected. This

approximation requires furthermore that $\Delta \ll E_e/\hbar$, i.e. the detuning is small with respect to the driving field. This approximation is called the rotating wave approximation, or RWA. With this approximation the Hamilton operator reads:

$$\hat{H}_{RWA} = \frac{\hbar}{2} \begin{pmatrix} \Delta & \Omega^* \\ \Omega & -\Delta \end{pmatrix} \quad (\text{A.7})$$

This form of the Hamilton operator leads to oscillations in the population.

A.2 The Adiabatic States

To allow for a time dependence of the electromagnetic fields I will from now on treat the Rabi frequency as function of time $\Omega(t)$. For a given point in time the matrix A.7 can be diagonalized. The corresponding eigenstates $|a^\pm(t)\rangle$ of the Hamiltonian:

$$H(t)|a^\pm(t)\rangle = \lambda(t)|a^\pm(t)\rangle \quad (\text{A.8})$$

are the adiabatic states. Here $\lambda(t)$ are the adiabatic eigenvalues. The matrix A.7 can be diagonalized with the matrix:

$$R(\vartheta(t)) = \begin{pmatrix} \cos \vartheta(t) & -\sin \vartheta(t) \\ \sin \vartheta(t) & \cos \vartheta(t) \end{pmatrix}, \quad (\text{A.9})$$

where $\vartheta(t) = \frac{1}{2} \arctan \frac{\Omega(t)}{\Delta}$ is the mixing angle. This diagonalisation leads to the eigenstates:

$$|a^-(t)\rangle = \cos \vartheta(t)|g\rangle - \sin \vartheta(t)|e\rangle \quad (\text{A.10})$$

$$|a^+(t)\rangle = \sin \vartheta(t)|g\rangle + \cos \vartheta(t)|e\rangle, \quad (\text{A.11})$$

with the corresponding eigenstates:

$$\lambda^\pm = \pm \sqrt{\Delta(t)^2 + |\Omega(t)|^2}. \quad (\text{A.12})$$

From this expression the dynamic Stark shift can be directly derived. It is $\hbar\Delta\omega_{Stark} = (\lambda_+ - \lambda_- - \hbar\Delta(t))/2$. In case of a large detuning $|\Omega(t)| \ll |\Delta(t)|$ the following expression is valid:

$$\Delta\omega_{Stark} = \frac{\hbar \Omega(t)^2}{2 \Delta(t)} \quad (\text{A.13})$$

This dynamic Stark shift can be used to trap atoms, since it is proportional to the intensity of the light field.

A.3 Connection between Transition Rates and Rabi Oscillations

It is interesting to see that the transition rate (2.9) is closely related to the Rabi oscillation^[50]. The expansion of the transition rate at detuning of $\Delta = 0$ around $c_e = 0$ (2.14)

$|c_e(t)|^2 = \frac{\Omega^2}{2\Omega_{eff}^2}(1 - \cos(\Omega_{eff}t))$ leads to:

$$|c_e(t)|^2 = \frac{(\Omega t)^2}{4} + O((\Omega t)^4) \tag{A.14}$$

Comparing this result to the transition rate (2.9): $L_{n,m} = -2\pi i\delta(E_m - E_n)V_{m,n}$ requires one to calculate the transition rate for the population first:

$$P_{n,m}(t) = |L_{n,m}|^2 = (2\pi)^2\delta(E_m - E_n)^2|V_{nm}|^2. \tag{A.15}$$

To evaluate this expression the δ function can be treated in the limit of $\lim_{(E_n - E_m) \rightarrow 0}$:

$$\delta(E_m - E_n)^2 = \frac{1}{\pi^2} \frac{\sin^2((E_m - E_n)\frac{t}{2\hbar})}{(E_m - E_n)^2} \tag{A.16}$$

Hence

$$P_{n,m}(t) = |L_{n,m}|^2 = 4|V_{nm}|^2 \frac{\sin^2((E_m - E_n)\frac{t}{2\hbar})}{(E_m - E_n)^2} \tag{A.17}$$

Expanding this in the lowest order in $(E_n - E_m)$ results in:

$$P_{n,m}(t) = |L_{n,m}|^2 = 4|V_{nm}|^2 \left(\frac{t}{2\hbar}\right)^2 = \frac{|V_{nm}|^2}{\hbar^2} t^2 \tag{A.18}$$

with $V_{n,m} = -\frac{\hbar}{2}|\Omega_{n,m}|$:

$$P_{n,m}(t) = \frac{|\Omega_{n,m}|^2}{4} t^2 \tag{A.19}$$

A.4 The Density Matirix Formalism including Decay

The Schrödinger equation, Eq. (2.1), describes pure states. When processes like spontaneous decay is included into the calculations, it is much easier to treat the problem statically with the density matrix formalisms. For the two pure two level atom the density matrix is defined as:

$$\rho = \begin{pmatrix} c_g c_g^* & c_g c_e^* \\ c_e c_g^* & c_e c_e^* \end{pmatrix}, \quad (\text{A.20})$$

where c_g and c_e are the complex amplitudes of the state vectors, as used in Eq. (2.14). The dynamics of the density matrix ρ is given by the Liouville equation, which is equivalent to the Schrodinger equation, including the rotating wave aproximation:

$$i\hbar\dot{\rho} = [H_{RWA}, \rho], \quad (\text{A.21})$$

where H_{RWA} is the rotating wave Hamiltonian from Eq. (A.7). To account for the spontaneous decay the empirical factor ρ_{relax} is introduced:

$$\rho_{relax} = \begin{pmatrix} \Gamma\rho_{ee} & \frac{\Gamma}{2}\rho_{ge} \\ \frac{\Gamma}{2}\rho_{eg} & -\Gamma\rho_{ee} \end{pmatrix}, \quad (\text{A.22})$$

where ρ_{xx} denote the elements of the density matrix. The full matrix evolution equation reads: $i\hbar\dot{\rho} = [H_{RWA}, \rho] + \rho_{relax}$. If the components are written out the Bloch equations are obtained:

$$\dot{\rho}_{gg} = -i\frac{\Omega}{2}(\rho_{eg} - \rho_{ge}) + \Gamma\rho_{ee} \quad (\text{A.23})$$

$$\dot{\rho}_{ee} = i\frac{\Omega}{2}(\rho_{eg} - \rho_{ge}) - \Gamma\rho_{ee} \quad (\text{A.24})$$

$$\dot{\rho}_{ge} = -i\Delta\rho_{ge} - i\frac{\Omega}{2}(\rho_{ee} - \rho_{gg}) - \frac{\Gamma}{2}\rho_{ge} \quad (\text{A.25})$$

$$\dot{\rho}_{eg} = i\Delta\rho_{eg} + i\frac{\Omega}{2}(\rho_{ee} - \rho_{gg}) - \frac{\Gamma}{2}\rho_{eg}. \quad (\text{A.26})$$

These equations can analytically be solved for the steady state, i.e. for $\dot{\rho} = 0$:

$$\rho_{ee} = \frac{\Omega}{2} \frac{1}{\Gamma} (\rho_{eg} - \rho_{ge}) \quad (\text{A.27})$$

$$\rho_{ge} = i\frac{\Omega}{2} \frac{1}{\frac{\Gamma}{2} + i\Delta} (\rho_{gg} - \rho_{ee}). \quad (\text{A.28})$$

By conservation of population $\rho_{gg} + \rho_{ee} = 1$ the equations can be solved:

$$\rho_{ee} = \frac{\Omega^2}{4} \frac{1}{\Delta^2 + \frac{\Gamma^2}{4} + \frac{1}{2}\Omega^2} \quad (\text{A.29})$$

$$\rho_{ge} = i\frac{\Omega^2}{4} \frac{1}{\Delta^2 + \frac{\Gamma^2}{4} + \frac{1}{2}\Omega^2}. \quad (\text{A.30})$$

These equation describe the population in the upper state and the coherence of the atomic system.

Appendix B

Rubidium Reference Data

The reference data presented here is taken from^[53] unless otherwise stated.

B.1 Universal Physical Constants

Speed of Light	c	299 792 458 m/s
Plank's Constant	h	$6.626 \cdot 10^{-34}$ Js $4.135 \cdot 10^{-15}$ eVs
Reduced Plank's Constant	\hbar	$1.054 \cdot 10^{-34}$ Js $6.582 \cdot 10^{-16}$ eVs
Reduced Boltzmann's Constant	k_B	$1.388 \cdot 10^{-23}$ JK ⁻¹
Elementary Charge	e	$1.602 \cdot 10^{-19}$ C
Electron Mass	m_e	$5.485 \cdot 10^{-31}$ kg
Atomic Mass Unit	u	$1.661 \cdot 10^{-27}$ kg
Bohr Magnetron	μ_B	$9.274 \cdot 10^{-24}$ J/T

B.2 Values of Rubidium

natural Abundance Rb ⁸⁵		72.2 %
natural Abundance Rb ⁸⁷		27.8 %
Vapor Pressure at Room Temp.		$33 \cdot 10^{-7}$ hPa

B.3 Other Physical Values

Specific Resistivity Copper (20°)	σ_{Cu}	$16.78 \cdot 10^{-9} \Omega\text{m}^{[101]}$
Thermal Conductivity Copper (20°)	k_{Cu}	$401 \text{ Wm}^{-1}\text{K}^{-1} [101]$
Thermal Expansion Copper (25°)	$\alpha_{L(Cu)}$	$16.5 \cdot 10^{-6} \text{ K}^{-1} [101]$

B.4 Rubidium 87 D₁ Transition

Transition Energy	$\hbar\omega$	1.559 eV
Vacuum Wavelength	λ	794.979 nm
Decay Rate	Γ	$36.129 \cdot 10^6 \text{ s}^{-1}$
Life time	τ	$27.679 \cdot 10^{-9} \text{ s}$
Effective Far-Detuned Saturation Intensity (π polarised)	$I_{sat(ef\text{f},D_1)}$	4.49 mw/cm^2

B.5 Rubidium 87 D₂ Transition

Transition Energy	$\hbar\omega$	1.589 eV
Vacuum Wavelength	λ	780.241 nm
Decay Rate	Γ	$38.12 \cdot 10^6 \text{ s}^{-1}$
Life time	τ	$26.24 \cdot 10^{-9} \text{ s}$
Effective Far-Detuned Saturation Intensity (π polarised)	$I_{sat(ef,D_2)}$	2.5 mW/cm ²
Cycling transition (π polarized) F=2,MF=±2 ↔ F'=3,MF=±3		
Saturation Intensity	$I_{sat(cyc)}$	1.67 mW/cm ²
Resonant Cross Section	$\sigma_{0(cyc)}$	0.291 μm ²

Appendix C

Pound-Drever-Hall Laser Stabilisation

The intensity and frequency of a laser tends to fluctuate randomly on short timescales as well as often showing some long term drift. For the experiments carried out in this thesis the frequency stabilisation is required to be accurate to about 1 MHz, which is on the order of $\frac{\Delta f}{f_0} = 2.5 \cdot 10^{-9}$, whereas intensity fluctuations on the order $\frac{\Delta I}{I} = 10^{-2}$ pose no problem. A straight forward approach to laser locking would be to lock onto the side of a transmission line in an atomic vapour cell, but a change in intensity I would be indistinguishable from a change in frequency ν . Hence a nulled locked-in detection is required to decouple intensity and frequency fluctuations. The Pound-Drever-Hall^[102] detection method does exactly that.

The Pound-Drever-Hall spectroscopy measures the phase delay of light instead of the absorption caused by a resonance. This could be an atomic resonance or

the resonance of an Fabry Perot interferometer. To measure the phase delay two symmetric side bands, with a detuning of a couple line-widths of the resonance, have to be modulated on top of the laser line. The phase shifts, above and below the resonance are opposite. By measuring these phase shifts, one can determine the laser detuning from resonance. I give a more quantitative description in the following paragraphs.

Usually the sidebands of the laser are generated by phase modulation of the electromagnetic wave. When it propagates through a medium whose index of refraction is modulated with a frequency of ω_m it picks up such a phase modulation. The magnitude of the modulation is determined by the modulation depth, M . Through modulating the driving current of the laser diode such a modulation of the index of refraction of the laser diode is obtained. This method easy to realise in the lab, but has the drawback that the entire laser radiation has sidebands. To avoid having the sidebands on the entire laser radiation a Pockels cell could be used to only generate the sidebands on the light which is used for locking.

The modulated electric field with a centre frequency of ω_0 can be written as:

$$E(t) = \frac{E_0}{2} \exp(i(\omega_0 t + M \sin(\omega_m t))) + c.c. \quad (\text{C.1})$$

The exponential function can be expanded using the Bessel functions $J_k(x)$:

$$E(t) = \frac{E_0}{2} \sum_{k=-\infty}^{\infty} J_k(M) \exp(i(\omega_0 + k\omega_m)t) + c.c. \quad (\text{C.2})$$

For sufficiently small M is sufficient to only take the the first two terms into account, since the lowest order of the expansion of the Bessel functions reads

$J_k(x) \approx \frac{1}{k!} \left(\frac{1}{2}x\right)^k$. Hence the expansion of the electric field reads:

$$E(t) = \frac{E_0}{2} [J_0(M) + J_{-1}(M)e^{-i\omega_m t} + J_1(M)e^{i\omega_m t}] e^{i\omega_0 t} + c.c \quad (C.3)$$

The intensity of the centre frequency is $P_c = \frac{c\epsilon_0}{2} J_0^2(M) E_0^2$ and of the sidebands $P_s = \frac{c\epsilon_0}{2} J_1^2(M) E_0^2$. After passing through the atomic sample the expansion (C.2) has to be extended by the transmission coefficients: $T_k = \exp(-\delta_k - i\phi_k)$, where δ_k is the absorption coefficient and ϕ_k is the phase delay coefficient. The transmitted Intensity I_t contains terms with various dependence of ω_m :

$$I_{ref} = P_c |T_0|^2 + P_s (|T_1|^2 + |T_{-1}|^2) \quad (C.4)$$

$$+ 2\sqrt{P_c P_s} \text{Re}(T_0 \bar{T}_1 - \bar{T}_0 T_{-1}) \cos(\omega_m t) \quad (C.5)$$

$$+ 2\sqrt{P_c P_s} \text{Im}(T_0 \bar{T}_1 - \bar{T}_0 T_{-1}) \sin(\omega_m t) \quad (C.6)$$

$$+ (\text{Terms depending on } 2\omega_m) \quad (C.7)$$

The terms (C.5, C.6) describe the mixing the carrier with the side bands. The first term is related to the absorption, whereas the second term relates to the phase delay. The term imaginary part (C.6) expands to:

$$\text{Im}(T_0 \bar{T}_1 - \bar{T}_0 T_{-1}) \approx e^{-\delta_0} (\phi_1 + \Phi_{-1} - 2\phi_0). \quad (C.8)$$

To access the term (C.6) experimentally, the signal of the oscillator modulation the current of the laser has to mixed with the photodetector output signal. The frequency mixing is described by the formula:

$$\begin{aligned} \sin(\omega_1 t + \phi_1) \sin(\omega_2 t + \phi_2) = & \frac{1}{2}(\cos(\omega_1 t + \phi_1 - \omega_2 t - \phi_2) \\ & - \cos(\omega_1 t + \phi_1 + \omega_2 t + \phi_2)). \end{aligned} \quad (\text{C.9})$$

The frequency mixing produces a low frequency and a high frequency part. If the frequencies ω_1 , ω_2 are the same the first term in (C.9) is a dc term which magnitude depends on the phase difference: $\cos(\phi_1 - \phi_2)$. Hence the in phase term can be singled out. This is done by including a phase delay into the setup, see Fig. C.1.

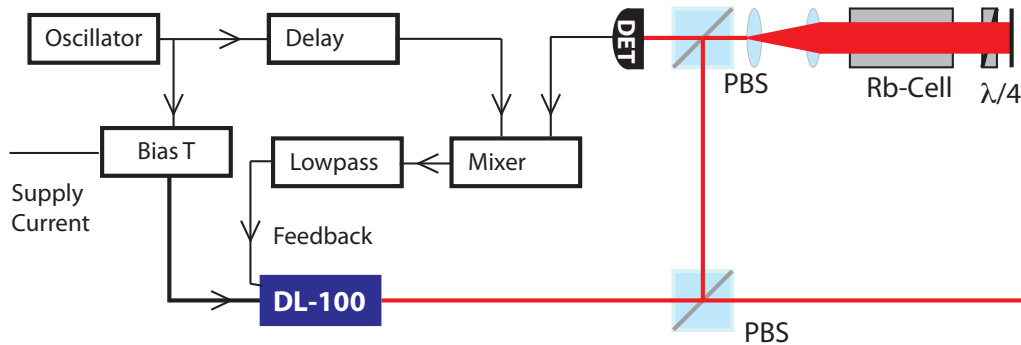


Figure C.1 Scheme of the Pound-Drever-Hall set up. The driving current of the laser is modulated through a local oscillator. Some light of the laser is split for the spectroscopy. The output signal is then frequency mixed with the local oscillator. Through a delay the in phase component of the photodetector signal can be selected and is singled out through the lowpass filter.

Appendix D

The Computer Control

The software which I developed using LabView, deals with a variety of things:

The MOST depends on many parameters that need to be controlled dynamically for experiments like time of flight measurement and the loading of the dipole-force trap. The time scale required for the control is determined by the speed of the atoms, which at the doppler cooling limit is about $170 \mu\text{m}/\text{ms}$. Since the dimension of the trap is on the order of $100 \mu\text{m}$, a sub-millisecond time scale is required.

All the measurements on the trapped atoms carried out in this thesis rely on imaging either the atomic fluorescence or absorption, which are observed with CCD-cameras. A real-time analysis of these images is required for the efficient optimisation of the trapping procedures.

Here is a list of the parameters that need to be controlled:

No	Description	Parameter
1	Cooling Laser	Amplitude
2	Cooling Laser	Frequency
3	Repumping Laser	Amplitude
4	Illumination Laser	Amplitude
5	U-shaped wire	Current
6	Bias-Coils	Current
7	Y-Compensation Coils	Current
8	Z-Compensation Coils	Current
9	Camera	Trigger

I use a self programmed software based of Labview, to operate the experiment. The software runs on a standard Windows desk top computer (Dell). The computer contains two two Adlink DAQ-2502 IO-board, which are synchronised to operate with a repetition rate of 100 kHz. The programme can be either run in a continuous mode or execute predefined sequences. In the continuous mode the parameters can be changed in real time and further image analysis tools determine a relative atom number from fluorescence of the atoms in the MOT as well as cross section through the trap. These features turn out to be very useful for the beam alignment. To configure the sequences the program contains an sequence editor. This editor also allows a one or two dimensional scan in multiple parameters. There are furthermore standard functions included to load the MOT prior to a sequence and to automatically execute and analyse absorption imaging. This programme has proven versatile

and easy to modify to operate the experiment.

Appendix E

The Gaussian Beam Optics

In optics the Gaussian Beam describes a beam of light, which is identical to the fundamental transverse mode of a laser resonator.

E.1 The Electric Field

The electric field is given by the following expression for linear polarization:

$$E(r, z) = E_0 \frac{w_0}{w(z)} \exp\left(\frac{-r^2}{w^2(z)}\right) \exp\left(-ikz - ik\frac{r^2}{2R(z)} + i\zeta(z)\right) + c.c., \quad (\text{E.1})$$

where r is the radial coordinate, z is the axial coordinate, $k = \frac{2\pi}{\lambda}$ is the wave number,

$$w(z) = w_0 \sqrt{1 + \left(\frac{z}{z_0}\right)^2} \quad (\text{E.2})$$

is the beam waist with z_r is the Rayleigh range, which is defined as $w(\pm z_0) = w_0\sqrt{2}$.

The Rayleigh range is determined by the beam waist $z_r = \frac{\pi w_0^2}{\lambda}$.

$$R(z) = z \left(1 + \frac{z_0^2}{z^2} \right) \quad (\text{E.3})$$

is the radius of field curvature and

$$\zeta(z) = \arctan \left(\frac{z}{z_0} \right) \quad (\text{E.4})$$

is the Gouy phase, which shifts the phase by π when it goes through the focus.

E.2 Beam Expansion

The beam expands with an angle $\theta = \lim_{z \rightarrow \infty} \arctan \left(\frac{w(z)}{z} \right)$, which is for small angles $\theta \approx \frac{\lambda}{\pi w_0}$. This angle is related to the numerical aperture with $NA = n \sin \theta$, where n is the refractive index which can be set to 1 for lenses being placed in air or vacuum. For small angles θ it is $N \approx \frac{D/2}{f}$, where f is the focal length of the lens and D is the clear aperture of the lens. The f-number is defined as the ratio between the clear aperture of the lens and the lens and the focal length of the lens $N = f/D$, which is for small angles θ : $N = \frac{1}{2NA}$. It has to be noted though that that a gaussian beam with an opening angle of θ requires a length which has an numerical aperture $N \ll \sin \theta$ since its field is not completely contained into the beam waist of $w(z)$.

E.3 The Intensity and Power

The time average intensity is related to the electric field by $I = \frac{1}{2\epsilon_0 c} |E^2|$ hence:

$$I(r, z) = I_0 \left(\frac{w_0}{w(z)} \right)^2 \exp \left(\frac{-2r^2}{w^2(z)} \right). \quad (\text{E.5})$$

The power of a Gaussian beam is:

$$P_0 = \frac{1}{2} \pi I_0 w_0^2. \quad (\text{E.6})$$

The power which propagates through a circle of radius r is :

$$P(r, z) = P_0 \left(1 - \exp \left(\frac{-2r^2}{w^2(z)} \right) \right), \quad (\text{E.7})$$

which for the following values of $r = 1, 1.5, 2$: $P(r = 1 w, 0) = 0.865 P_0$,

$P(r = 1.5 w, 0) = 0.989 P_0$, $P(r = 2 w, 0) = 0.9997 P_0$.

E.4 The retro-reflected Beam

A Gaussian beam which is focussed with a distance of L in front of a mirror interferes with the reflected image. The electric field can be described as the sum of the incoming and outgoing field, where $z = 0$ defines the focal point of the incoming beam:

$$E_{tot}(r, z) = E_{in}(r, z) + E_{out}(r, -(z + 2L))$$

The Intensity is given by $I = \frac{1}{2\epsilon_0 c} |(E_{in} + E_{out})^2|$, which can be decomposed into an

static term $I_{av} = \frac{1}{2\epsilon_0 c} |(E_{in})^2 + (E_{out})^2|$ and an oscillating term $I_{osc} = \frac{1}{\epsilon_0 c} |E_{in} \cdot E_{out}|$.

The average Intensity along the z-axis is:

$$I_{av}(z) = I_0 \left(\frac{1}{1 + \frac{z^2}{z_0^2}} + \frac{1}{1 + \frac{(z+2L)^2}{z_0^2}} \right), \quad (\text{E.8})$$

where I_0 is the maximum field intensity for one running wave only. Around the average value $I_{av}(z)$ there is a oscillation of the intensity with a peak to peak amplitude of:

$$A(z) = \frac{4U_0}{\sqrt{1 + z^2/z_0^2} \sqrt{1 + (2L + z)^2/z_0^2}}, \quad (\text{E.9})$$

with a periodicity of $\approx \lambda/2$, a small deviation from $\lambda/2$ is due to the Gouy phase phase of the electric field, which changes by π , while the beam propagates through the focal point.

Appendix F

The Collimator in the Diffuser Setup

The parameter of the collimator lens in the diffuser setup have to be chosen so that most of the radiation propagates through its clear aperture and to illuminate the DMD with a suitable beam diameter.

The DMD will be placed in the far field of the diffusers, which lies one focal length behind the collimator lens. The DMD should be nearly homogeneously illuminated, hence $d_{ff} \approx D_{dmd}$. The far field diameter is given by Eqn. (11.6), which leads to:

$$f_{col} \approx \frac{D_{dmd}}{2 \tan(\alpha_{tot}/2)}. \quad (\text{F.1})$$

A second restraint is that the diameter of the collimating lens has to be bigger than the beam diameter: $D_{col} > d_{coll}$, but it poses no substantial restriction, as I

will show next. Assuming that the spread after the diffuser is much larger than the spot size on the diffuser, i.e. $l_1 \tan(\alpha_{tot}/2) \gg d_{dif}$, Eq. (11.13) together Eq. (11.14) yields:

$$d_{col} \approx l_1 \cdot 2 \tan(\alpha_{tot}/2) \quad (\text{F.2})$$

Eq. (11.16) relates the spot size on the diffuser d_{dif} with the spot size on the imaging lens d_{im} , it can be expressed as:

$$l_3 = f_{col} \frac{d_{im}}{d_{dif}} \quad (\text{F.3})$$

to choose the distance l_3 for a given focal length of the diffuser. Together with 11.9 which fixes the distance l_1 , with respect to l_3 and f_{col} one obtains:

$$l_1 = f_{col}(d_{dif}/d_{im} + 1) \quad (\text{F.4})$$

Since the spot-size on the imaging lens is much larger than the spot size on the diffuser $d_{im} \ll d_{dif}$, the following holds $l_1 \approx f_{col}$. Putting it all together one obtains:

$$D_{col} > 2f_{col} \tan(\alpha_{tot}/2) \quad (\text{F.5})$$

The diffuser in used has a divergence angle of 9.1° , which leads to a required numerical aperture of $2 \tan(\alpha_{tot}/2) = 0.16$, for which commercially available singlets can be found.

Bibliography

- [1] Einstein, A., Podolsky, B., & Rosen, N. *Physical Review* **47**, 777 (1935).
- [2] Aspect, A., Grangier, P., & Roger, G. *Physical Review Letters* **49**, 91 (1982).
- [3] MAIMAN, T. H. *Nature* **187**, 493 (1960).
- [4] Arimondo, E. In *Progress in Optics*, vol. Volume 35, pages 257–354. Elsevier (1996).
- [5] Vitanov, N. V., Halfmann, T., Shore, B. W., & Bergmann, K. *Annual Review of Physical Chemistry* **52**, 763 (2001).
- [6] Fleischhauer, M., Imamoglu, A., & Marangos, J. P. *Reviews of Modern Physics* **77**, 633 (2005).
- [7] Hong, C. K., Ou, Z. Y., & Mandel, L. *Physical Review Letters* **59**, 2044 (1987).
- [8] Kwiat, P. G., Mattle, K., Weinfurter, H., Zeilinger, A., Sergienko, A. V., & Shih, Y. *Physical Review Letters* **75**, 4337 (1995).
- [9] Holzscheiter, M. H. *Physica Scripta* **T59**, 69 (1995).

-
- [10] Itano, W. M., Bergquist, J. C., Bollinger, J. J., & Wineland, D. J. *Physica Scripta* **T59**, 106 (1995).
- [11] DiVincenzo, D. *Fortschr. Phys.* **48**, 771 (2000).
- [12] Buluta, I. & Nori, F. *Science* **326**, 108 (2009).
- [13] Häffner, H., Roos, C., & Blatt, R. *Physics Reports* **469**, 155 (2008).
- [14] Blatt, R. & Wineland, D. *Nature* **453**, 1008 (2008).
- [15] Karski, M., Förster, L., Choi, J., Steffen, A., Alt, W., Meschede, D., & Widera, A. *Science* **325**, 174 (2009).
- [16] Beugnon, J., Tuchendler, C., Marion, H., Gaetan, A., Miroshnychenko, Y., Sortais, Y. R. P., Lance, A. M., Jones, M. P. A., Messin, G., Browaeys, A., & Grangier, P. *Nat Phys* **3**, 696 (2007).
- [17] Bloch, I. *Nature* **453**, 1016 (2008).
- [18] Grimm, R., Weidemüller, M., & Ovchinnikov, Y. *Adv. At. Mol. Opt. Phys.* **42**, 95 (2000).
- [19] Schrader, D., Dotsenko, I., Khudaverdyan, M., Miroshnychenko, Y., Rauschenbeutel, A., & Meschede, D. *Physical Review Letters* **93**, 150501 (2004).
- [20] Riebe, M., Monz, T., Kim, K., Villar, A. S., Schindler, P., Chwalla, M., Henrich, M., & Blatt, R. *Nat Phys* **4**, 839 (2008).

- [21] Sewell, R. J., Dingjan, J., Baumgärtner, F., Llorente-García, I., Eriksson, S., Hinds, E. A., Lewis, G., Srinivasan, P., Muktadir, Z., Gollasch, C. O., & Kraft, M. *Journal of Physics B: Atomic, Molecular and Optical Physics* **43**, 051003 (2010).
- [22] Heine, D., Wilzbach, M., Raub, T., Hessmo, B., & Schmiedmayer, J. *Physical Review A* **79**, 021804 (2009).
- [23] Hansel, W., Hommelhoff, P., Hansch, T. W., & Reichel, J. *Nature* **413**, 498 (2001).
- [24] Reichel, J. *Applied Physics B: Lasers and Optics* **74**, 469 (2002).
- [25] Rosenfeld, W., Weber, M., Volz, J., Henkel, F., Krug, M., Cabello, A., Zukowski, M., & Weinfurter, H. *Adv. Sci. Lett* **2**, 469 (2009).
- [26] Henkel, F., Krug, M., Hofmann, J., Rosenfeld, W., Weber, M., & Weinfurter, H. *Physical Review Letters* **105**, 253001 (2010).
- [27] Gehr, R., Volz, J., Dubois, G., Steinmetz, T., Colombe, Y., Lev, B. L., Long, R., Estève, J., & Reichel, J. *Physical Review Letters* **104**, 203602 (2010).
- [28] Fuhrmanek, A., Sortais, Y. R. P., Grangier, P., & Browaeys, A. *Physical Review A* **82**, 023623 (2010).
- [29] Sherson, J. F., Weitenberg, C., Endres, M., Cheneau, M., Bloch, I., & Kuhr, S. *Nature* **467**, 68 (2010).

- [30] Weitenberg, C., Endres, M., Sherson, J. F., Cheneau, M., Schausz, P., Fukuhara, T., Bloch, I., & Kuhr, S. *Nature* **471**, 319 (2011).
- [31] Bakr, W. S., Gillen, J. I., Peng, A., Folling, S., & Greiner, M. *Nature* **462**, 74 (2009).
- [32] Lengwenus, A., Kruse, J., Schlosser, M., Tichelmann, S., & Birkl, G. *Physical Review Letters* **105**, 170502 (2010).
- [33] Bergamini, S., Darquié, B., Jones, M., Jacubowicz, L., Browaeys, A., & Grangier, P. *Journal of the Optical Society of America B* **21**, 1889 (2004).
- [34] Zimmermann, B., Müller, T., Meineke, J., Esslinger, T., & Moritz, H. *New Journal of Physics* **13**, 043007 (2011).
- [35] MacAulay, C. & Dlugan, A. *Proc. Spie* **3260**, 201 (1998).
- [36] Hanley, Verveer, Gemkow, Arndt-Jovin, & Jovin. *Journal of Microscopy* **196**, 317 (1999).
- [37] Ashkin, A. & Dziedzic, J. M. *Science* **235**, 1517 (1987).
- [38] Thompson, R. J., Rempe, G., & Kimble, H. J. *Physical Review Letters* **68**, 1132 (1992).
- [39] Nuzmann, S., Murr, K., Hijlkema, M., Weber, B., Kuhn, A., & Rempe, G. *Nat Phys* **1**, 122 (2005).

-
- [40] Maunz, P., Puppe, T., Schuster, I., Syassen, N., Pinkse, P. W. H., & Rempe, G. *Nature* **428**, 50 (2004).
- [41] McKeever, J., Boca, A., Boozer, A. D., Miller, R., Buck, J. R., Kuzmich, A., & Kimble, H. J. *Science* **303**, 1992 (2004).
- [42] Hijlkema, M., Weber, B., Specht, H. P., Webster, S. C., Kuhn, A., & Rempe, G. *Nat Phys* **3**, 253 (2007).
- [43] Brune, M., Schmidt-Kaler, F., Maali, A., Dreyer, J., Hagley, E., Raimond, J. M., & Haroche, S. *Physical Review Letters* **76**, 1800 (1996).
- [44] Goy, P., Raimond, J. M., Gross, M., & Haroche, S. *Physical Review Letters* **50**, 1903 (1983).
- [45] Keller, M., Lange, B., Hayasaka, K., Lange, W., & Walther, H. *Nature* **431**, 1075 (2004).
- [46] Brennecke, F., Donner, T., Ritter, S., Bourdel, T., Kohl, M., & Esslinger, T. *Nature* **450**, 268 (2007).
- [47] Colombe, Y., Steinmetz, T., Dubois, G., Linke, F., Hunger, D., & Reichel, J. *Nature* **450**, 272 (2007).
- [48] Pellizzari, T. *Physical Review Letters* **79**, 5242 (1997).
- [49] Raussendorf, R. & Briegel, H. J. *Physical Review Letters* **86**, 5188 (2001).

-
- [50] Cohen-Tannoudji, C., Dupont-Roc, J., & Grynberg, G. *Atom-Photon-Interactions*. Wiley-VCH, Weinheim (2004).
- [51] Shore, B. *Acta Physica Slovaca. Reviews and Tutorials* **58**, 243 (2008).
- [52] Foot, C. *Atomic Physics*. Oxford University Press (2005).
- [53] Steck, D. *Rubidium 87 D Line Data*. <http://steck.us/alkalidata> (2010).
- [54] Metcalf, H. & van der Straten, P. *Laser Cooling and Trapping*. Springer, New York (1999).
- [55] Himsforth, M. & Freearde, T. *Physical Review A* **81**, 023423 (2010).
- [56] Smith, D. & Hughes, I. *Am. J. o. Phys.* **72**, 631 (2004).
- [57] Jack Devlin. *Electromagnetically induced transparency in rubidium-87 vapour*. Master's thesis, University of Oxford (2011).
- [58] Hänsch, T. & Schawlow, A. *Opt. Commun.* **15**, 68 (1975).
- [59] Chu, S., Hollberg, L., Bjorkholm, J. E., Cable, A., & Ashkin, A. *Physical Review Letters* **55**, 48 (1985).
- [60] Youk, H. *CUPJ* **111**, 13 (2005).
- [61] Reichel, J. *Applied Physics B* **74**, 469 (2002).
- [62] Wildermuth, S., Krüger, P., Becker, C., Brajdic, M., Haupt, S., Kasper, A., Folman, R., & Schmiedmayer, J. *Physical Review A* **69**, 030901 (2004).

- [63] Demtröder, W. *Laser Spectroscopy*. Springer (2003).
- [64] Kuppens, S. J. M., Corwin, K. L., Miller, K. W., Chupp, T. E., & Wieman, C. E. *Physical Review A* **62**, 013406 (2000).
- [65] Brandt, L., Muldoon, C., Thiele, T., Dong, J., Brainis, E., & Kuhn, A. *Applied Physics B* **102**, 443 (2010).
- [66] Benseny, A., Fernández-Vidal, S., Bagudà, J., Corbalán, R., Picón, A., Roso, L., Birkl, G., & Mompart, J. *Physical Review A* **82**, 013604 (2010).
- [67] van Kessel, P., Hornbeck, L., Meier, R., & Douglas, M. *Proc. IEEE* **86**, 1687 (1998).
- [68] Brainis, E., Muldoon, C., Brandt, L., & Kuhn, A. *Optics Communications* **282**, 465 (2009).
- [69] Alt, W. *Optik - International Journal for Light and Electron Optics* **113**, 142 (2002).
- [70] Sortais, Y. R. P., Marion, H., Tuchendler, C., Lance, A. M., Lamare, M., Fournet, P., Armellin, C., Mercier, R., Messin, G., Browaeys, A., & Grangier, P. *Physical Review A* **75**, 013406 (2007).
- [71] Schlosser, N., Reymond, G., Protsenko, I., & Grangier, P. *Nature* **411**, 1024 (2001).
- [72] Schlosser, N., Reymond, G., & Grangier, P. *Physical Review Letters* **89**, 023005 (2002).

- [73] Frese, D., Ueberholz, B., Kuhr, S., Alt, W., Schrader, D., Gomer, V., & Meschede, D. *Physical Review Letters* **85**, 3777 (2000).
- [74] Dotsenko, I., Alt, W., Khudaverdyan, M., Kuhr, S., Meschede, D., Miroshnychenko, Y., Schrader, D., & Rauschenbeutel, A. *Physical Review Letters* **95**, 033002 (2005).
- [75] Mücke, M., Figueroa, E., Bochmann, J., Hahn, C., Murr, K., Ritter, S., Villas-Boas, C. J., & Rempe, G. *Nature* **465**, 755 (2010).
- [76] Born, M. & Wolf, E. *Principles of Optics*. Cambridge University Press, Cambridge, 7 ed. (2006).
- [77] Goodman, J. *Introduction to Fourier Optics*. Roberts & Company, Englewood, 3 ed. (2005).
- [78] Dumontet, P. *Optica Acta* **2**, 53 (1955).
- [79] Tichenor, D. & Goodman, J. *J. Opt. Soc. Am.* **62**, 293 (1972).
- [80] E. Hecht. *Optics*. Addison Wesley, San Francisco, 4 ed. (2002).
- [81] Ohadi, H., Himsworth, M., Xuereb, A., & Freegarde, T. *Optics Express* **17**, 23003 (2009).
- [82] Gillen, J. I., Bakr, W. S., Peng, A., Unterwaditzer, P., Fölling, S., & Greiner, M. *Physical Review A* **80**, 021602 (2009).
- [83] Nelson, K. D., Li, X., & Weiss, D. S. *Nat Phys* **3**, 556 (2007).

- [84] Grunzweig, T., Hilliard, A., McGovern, M., & Andersen, M. F. *Nat Phys* **6**, 951 (2010).
- [85] Steinmetz, T., Colombe, Y., Hunger, D., Hänsch, T. W., Balocchi, A., Warburton, R. J., & Reichel, J. *Applied Physics Letters* **89**, 111110 (2006).
- [86] Hunger, D., Steinmetz, T., Colombe, Y., Deutsch, C., Hänsch, T. W., & Reichel, J. *New Journal of Physics* **12**, 065038 (2010).
- [87] Sagué, G., Vetsch, E., Alt, W., Meschede, D., & Rauschenbeutel, A. *Physical Review Letters* **99**, 163602 (2007).
- [88] Vetsch, E., Reitz, D., Sagué, G., Schmidt, R., Dawkins, S. T., & Rauschenbeutel, A. *Physical Review Letters* **104**, 203603 (2010).
- [89] O'Shea, D., Rettenmaier, A., & Rauschenbeutel, A. *Applied Physics B* **99**, 623 (2010).
- [90] Ryu, H., Hwang, J., & Lee, Y. *Quantum Electronics, IEEE Journal of* **39**, 314 (2003).
- [91] Armani, D. K., Kippenberg, T. J., Spillane, S. M., & Vahala, K. J. *Nature* **421**, 925 (2003).
- [92] Aoki, T., Dayan, B., Wilcut, E., Bowen, W. P., Parkins, A. S., Kippenberg, T. J., Vahala, K. J., & Kimble, H. J. *Nature* **443**, 671 (2006).
- [93] Loyer, Y., Meschede, D., & Rauschenbeutel, A. *Physical Review A* **72**, 031801 (2005).

-
- [94] Cai, M., Painter, O., & Vahala, K. J. *Physical Review Letters* **85**, 74 (2000).
- [95] Gaetan, A., Miroshnychenko, Y., Wilk, T., Chotia, A., Viteau, M., Comparat, D., Pillet, P., Browaeys, A., & Grangier, P. *Nat Phys* **5**, 115 (2009).
- [96] Wilk, T., Gaëtan, A., Evellin, C., Wolters, J., Miroshnychenko, Y., Grangier, P., & Browaeys, A. *Physical Review Letters* **104**, 010502 (2010).
- [97] Pupillo, G., Micheli, A., Boninsegni, M., Lesanovsky, I., & Zoller, P. *Physical Review Letters* **104**, 223002 (2010).
- [98] Weimer, H., Muller, M., Lesanovsky, I., Zoller, P., & Buchler, H. P. *Nat Phys* **6**, 382 (2010).
- [99] Müller, M., Liang, L., Lesanovsky, I., & Zoller, P. *New Journal of Physics* **10**, 093009 (2008).
- [100] Jaksch, D., Briegel, H.-J., Cirac, J. I., Gardiner, C. W., & Zoller, P. *Physical Review Letters* **82**, 1975 (1999).
- [101] *Copper*. <http://en.wikipedia.org/wiki/Copper> (2011).
- [102] Black, E. D. *Am. J. Phys.* **69**, 79 (2001).